Copyright

by

Wei Du

2016

The Dissertation Committee for Wei Du

certifies that this is the approved version of the following dissertation:

Mathematical Modeling of the Interaction between Two-phase Environmental Flow and Protective Hydraulic Structures

Committee:

Clint Dawson, Supervisor

Leszek Demkowicz

Irene Gamba

Omar Ghattas

Tan Bui-Thanh

Mathematical Modeling of the Interaction between Two-phase Environmental Flow and Protective Hydraulic Structures

by

Wei Du, B.S.; M.S.C.S.E.M

DISSERTATION

Presented to the Faculty of the Graduate School of

The University of Texas at Austin

in Partial Fulfillment

of the Requirements

for the Degree of

DOCTOR OF PHILOSOPHY

THE UNIVERSITY OF TEXAS AT AUSTIN

December 2016

Dedicated to my parents.

Acknowledgments

I wish to thank all the people who helped me during my graduate school study. First, I would like to thank my family, especially my parents. They are the first teachers who led me to enter the world of science and engineering. Their encouragement and support help me get through all the difficulties in life and study. I would like to thank my undergraduate advisors Xin Li and Zuchi Chen, who introduced me to the Institute for Computational Engineering and Sciences and encouraged me to attend the University of Texas at Austin.

I want to express my deep appreciation to the University of Texas at Austin, the Institute for Computational Engineering and Sciences, the Severe Storm Prediction, Education, and Evacuation from Disasters (SSPEED) Center of Rice University, and the Computational Hydraulics Group. The faculty, staff and postdocs have given me much help both on academics and life, physically and mentally. I want to thank all my committee: Irene Gamba, Omar Ghattas, Leszek Demkowicz, Tan Bui-Thanh, and my advisor Clint Dawson. Thank you Dr. Dawson for your unremitting guidance on my graduate study and research work. You lead me to get approach to the hurricane storm surge and protection system design topic. The huge influence of our work to the society always inspires and fulfills me. Thank you for all the professional trainings, including the weekly discussion and the presentation in group meeting,

from which I benefit much. I would also like to thank Dr. Steven Mattis. Thank you for your guidance all the way through my research. You share the valuable experience with Proteus and flow modeling, and shed light to me whenever I encounter difficulties from building proper models to choosing numerical methods.

I am also thankful to my friends from the Institute for Computational Engineering and Sciences, Mathematics Department and Aerospace Engineering and Engineering Mechanics Department of the University of Texas at Austin, in particular to Mr. Yimin Zhong, Dr. Prapti Neupane, Dr. Lindley Graham, Mr. Jiachuan He, Dr. Jessica Meixner, Dr. Jennifer Proft, Dr. Casey Dietrich, Mr. Ju Liu, Mr. Dongjie Jiang, Ms. Nora Deram, Ms. Yunan Yang. I cannot list all of my friends and people who have helped me in achieving what I have today. I am deeply grateful to have you all in my life.

Mathematical Modeling of the Interaction between Two-phase Environmental Flow and Protective Hydraulic Structures

Publication No. _____

Wei Du, Ph.D.
The University of Texas at Austin, 2016

Supervisor: Clint Dawson

In August 2005, Hurricane Katrina struck the Gulf Coast of the United States. Over a thousand people lost their lives and the total damage was about 108 billion USD. It was the costliest United States hurricane. Two-thirds of the deaths and majority of economical loss were related to the protection system failure. This drives the study of fluid structure interaction to properly design the levees and floodwalls in the future for flooding vulnerable areas.

Fluid-structure interaction is the interaction between a deformable structure and the surrounding flow. The fluid causes the deformation of the solid, and the solid reacts to the fluid. This thesis will focus on the interactions between two-phase environmental flow (air and water), and hydraulic structures (e.g. floodwalls, etc.) which are partially submerged in the water to disrupt the flow. Hydrodynamic and hydrostatic forces and impact loads from high water levels and velocities applied to

the interface must be carefully monitored, as well as their impact on the structural stability. The main purpose of this work is to give a deeper understanding to the interaction processes and the coupling effects, and to determine the possible deformation or critical values of overturning moments for more robust future designs of floodwalls and levees.

There are two main approaches to simulate fluid-solid interactions: the monolithic approach and the partitioned approach. In this work we use the partitioned approach by looking into the separate flow and structure models and simulating the interaction process. For the two-phase flow subproblem, the interface of air and water is treated as a material discontinuity in modeling, and is tracked by the level set method. The coupled system consists of Navier-Stokes Equation, level set method and the volume of fraction method, solved by the splitting method with residual-based variational multi-scale methods for stabilization. The structural mechanics is modeled by linear elasticity. Different types of floodwalls and two factors of safety against sliding and overturning are studied. In the Galveston area, the soil and floodwall properties determine the necessity to include soil as a part of the model. Hyperelastic and plastic models are discussed in simulating the soil behavior. The interaction process is modeled by imposing the matching conditions on the common fluid-structure boundary. Both one-way and two-way interaction models under synthetic waves are discussed and compared. One-way interaction is saving in computation and used widely in engineering design. Two-way interaction is formulated under the Arbitrary Lagrangian-Eulerian(ALE) framework. The operator splitting technique is developed for the coupled system to reduce computing cost while remain high accuracy.

Table of Contents

List of Tables

List of Figures

Chapter 1

Introduction

1.1 Background and Motivation

In August 2005, Hurricane Katrina struck the Gulf Coast of the United States. Over a thousand people lost their lives and a half million people were forced to evacuate. The total damage was about 108 billion USD. It was the costliest United States hurricane [37]. Katrina was catastrophic, especially the aftermath. Many parts of the surge protection system, made of levees and floodwalls, was breached during the hurricane. Impacted areas, such as New Orleans, were severly flooded. Two-thirds of the deaths and majority of economical loss were related to the protection system failure [38].

A federal order was issued to independent agencies and departments for investigations. All the studies showed the improper design and construction of the surge protection system was the main reason for flooding [39, 42, 43]. During the hurricane, over 50 levee and floodwall failures were reported. Inadequate design of canal floodwalls, overtopping, and sand effects caused the most failures. The oversight of the soil strength and not considering the water-filled gap were the primary reason

of flooding in the Lakeview neighborhood and the Gentilly neighborhood [40, 41]. In four cases, the floodwalls and levees even failed before the surge exceeded the designed elevations [42, 44]. This drives the study of fluid structure interaction in specific flooding vulnerable areas.

Fluid structure interaction(FSI) is the interaction between the deformable structure made up of one or more materials and the internal or surrounding flow. The fluid forces acting on the interface between the fluid and the structure cause the deformation or movement of the solid. The spatial change of the structure also influences the flow behavior. In other words, the movements of the two subparts are affected by each other. FSI is a commonly seen phenomenon in many natural or engineering systems, for example, air and turbines, blood and the heart valves, water and submerged vegetation, etc. As a result growing attention has been paid to this problem as well as the study and development of mathematical models and numerical simulation of these processes.

The main focus in this work is the interaction between two-phase environmental flow (mainly air and water), and hydraulic structures (e.g. floodwall, levees, etc.) which are partially submerged in the flow. Floodwalls and levees are usually built in coastal regions to prevent flooding from storm surge during hurricane season [20, 28]. Currently there are levees in all 50 states. In Greater Houston area, there is still significant risk [25, 26, 27, 32] of flooding even with the existence of levees. It is possible that the levees can be overtopped, overturned, slid or even breached by heavy floods [24, 28], like what happened in Hurricane Katrina.

In 2008, Hurricane Ike caused great damage to the Galveston Bay area, the

Bolivar Peninsula and Houston with approximately 3.4 billion dollars of total loss. Various protections are being studied by the Severe Storm Prediction, Eduction, and Evacuation from Disasters (SSPEED) center at Rice University. These projects could include enhancement of the existing Galveston Seawall, the USACE-constructed levees in Texas City and the Freeport Hurricane Protection Structure, among others [20, 28]. Therefore, it is of great importance and significance to conduct research on the interaction processes between the flow and the protective hydraulic structures in the region. The critical values of overturning moments or collapsing and the factor of safety should also be developed and evaluated, which provides significant information in the design or maintenance of the coastal structures for better protection of the residents and property [14, 24, 30].

To build the complete FSI model, a common method is to look into separate flow and structure models and simulate the coupling process between them afterwards [8, 9, 56]. The fluid subproblem is modeled as a two-phase flow, where incompressibility is assumed and the full 3D Navier-Stokes Equations are used [1, 2]. We treat the air-water interface as the material discontinuity. The level set method is applied to track the interface by an implicit scalar function. The volume fraction method and the eikonal equation are added for re-distancing. The structural mechanics is modeled by linear elasticity. In the Galveston area, the soil and floodwall properties determine the necessity to include soil as a part of the model [66]. Hyperelastic and plastic models are discussed in simulating the soil behavior. How the soil movement affects the floodwall is also studied from the coupled model. The interaction process is modeled by imposing the matching conditions on the common fluid-structure

boundary [9].

There are two basic computational approaches to solve the fully coupled system: the monolithic approach and the partitioned approach [8, 9, 22]. In the monolithic approach, the velocity of the flow and the displacement of the structure are solved simultaneously with a single solver [8, 9]. It is advantageous in parallel algorithms to formulate the different descriptions of fluid and structure into one framework. But it may result in a very large non-linear problem and may be expensive to solve numerically. For the partitioned approach, the fluid and the structure problems are solved separately and are connected through common boundary conditions [8, 22]. However, the use of an Eulerian description for the fluid and a Lagrangian description for the structure adds difficulties in modeling and makes it more difficult to parallelize [15, 17, 18, 19]. In this work, the conflict between different frameworks is solved by using the arbitrary Lagrangian Eulerian framework to reformulate the coupled system. For current study, we mainly focus on the partitioned approach.

In engineering analysis and design, a common and simple technique to deal with the interaction is often used - only one way interaction is considered. It means that the effect of structure deformation to the flow is neglected. The tractions at the common interface are computed and output from the separate flow model, then used as the boundary conditions to solve the separate structural subproblem. It works fine especially when the deformation is relatively small. The full two way interaction model takes account of the structure deformation, thus more complicated in theory and computation. We will discuss both interaction models. The partitioned method is used to solve the fully coupled system.

For verification we will compare the numerical results of one way and two way interaction models in the same system. In future work, monolithic solvers as well as 3D models will be developed. We will further study the application to a specific protection system in the Galveston Bay area. We will use the Advanced Circulation Model(ADCIRC) to obtain the external boundary forcing for the fluid model and look at various hurricane/levee scenarios. Our computations with existing levee/dam data and historical hurricane records will be compared. The final goal of this work is to evaluate the quantities of interest in the Galveston area more precisely, which has a significant effect in the design of coastal structures to better protect the local residents and properties.

1.2 Research Contributions

There have been many researches on the environmental flow and structure interaction problem. The introduce of multiple waves and two phase flow, which are closer to physical reality, differentiates our model from the others. We developed the open source python package for the fluid subproblem based on the framework Proteus from the US Army Corps of Engineers. One of the primary reasons for the levee and floodwall failures during Hurricane Katrina was the oversight of soil strength in design. In many soil-pile or soil-foundation interaction computation software, soil is modeled by layers of connected springs. In our model, we developed the C++ programs to simulate soil plasticity and describe the inelasticity more accurately. Our open source code consists of three parts: fluid subproblem, soil-floodwall subproblem

and interaction process. It provides the flexibility for users to choose the domain mesh shape and size, floodwall types, and one-way or two-way interaction models. Users can also combine or change specific submodels to implement their own models based on our current framework, which commercial software cannot provide. The completed research focus the three areas as Computational Science, Engineering and Mathematics program requires.

Area A: Applicable Mathematics. We investigate the partitioned approach for the coupling of the two-phase fluid and the solid[10]. The convergence rate is studied. Stability and a posterior error analysis are presented. We also study the one way interaction model in 2D for verification and comparison. A method is formulated for estimating the quantity of interest (QoI) including two factors of safety against sliding and overturning. We would also like to examine its dependence on Young's modulus, Poisson ratio and hydraulic pressure gradient, with different structural geometries considered.

Area B: Numerical Analysis and Scientific Computation. The two-phase Reynolds Averaged Navier-Stokes equations with spatially multiscale-stabilized Continuous Galerkin methods(RBVMS) are developed by operator splitting method under the Proteus framework[1, 3, 4, 5]. The formulation of the level set method and auxiliary equations are conservative with relatively accurate track of the air-water interface. The stabilized coupling scheme is used by adding a time penalty term on the pressure fluctuations of the fluid. By using the ALE formulation moving mesh is modeled to simulate the deformation of the two subdomains and track the fluid-structure interface. Sequential methods are developed for small and structured

meshes, and parallel computations will be performed with large unstructured meshes.

Area C: Mathematical Modeling and Application. Implementations are done in two dimensional spaces with various complexities of the meshes for both the one way and two way interaction models, by examples of generated waves and a flow interacting with a floodwall along the Galveston Bay coastline. Random multiple single peaked waves are included to simulate the natural gulf environmental condition. Effect of supporting soil is considered by adding the plasticity model to the structure subproblem. We will further study the application to a specific levee system in the Galveston Bay area and use the Advanced Circulation Model(ADCIRC) to obtain the external boundary forcing for model validation and future scenario predictions.

Chapter 2

The Fluid Model

For the incompressible fluid subproblem, we mainly focus on air-water two-phase flow [1]. One challenge is to precisely locate the positions of the interface over time. There have been many methods where the interface is treated as a material discontinuity, such as deforming mesh method, volume-of-fluid method, level set method, and particle method [1, 2]. In our work, the level set method is used, i.e. the interface between the two fluids is tracked by an implicit scalar function [2]. The positive and negative values of the level set function correspond to subdomains of water and air. In consideration of mass conservation, modified level set methods and the volume-of-fluid methods coupled with the signed distance function are used. Also a robust approach will be developed with high accuracy for precise phase material properties and complex geometric descriptions on the high performance computing platforms.

2.1 Two-phase Flow Model

2.1.1 Level Set Methods

In the level set method [1, 2], the interface Γ is represented by a scalar function $\phi(x)$. Γ is defined by:

$$\Gamma = \{\mathbf{x} | \phi(\mathbf{x}) = 0\}, \tag{2.1}$$

i.e., Γ is the zero level set for ϕ. For two fluids in the same domain Ω with the interface Γ, the water and air subdomains Γ_w and Γ_a, are defined as

$$\Gamma_w = \{\mathbf{x} | \phi(\mathbf{x}, t) > 0\} \tag{2.2}$$

and

$$\Gamma_a = \{\mathbf{x} | \phi(\mathbf{x}, t) < 0\}. \tag{2.3}$$

Then the interface evolution is represented as:

$$\frac{\partial \phi}{\partial t} + \mathbf{u} \cdot \nabla \phi = 0 \tag{2.4}$$

Here $\mathbf{u}$ is the flow velocity. The quantity $\int\limits_{\Omega} \phi \, d\Omega$ should remain unchanged if we use the conservative discrete formulation.

In the multiphase case, each phase of the fluid should be conserved. The key is to use the Heaviside function H which is defined as:

$$H(\phi) = \begin{cases} 0 & \phi < 0 \\ 1/2 & \phi = 0 \\ 1 & \phi > 0. \end{cases} \tag{2.5}$$

The density ρ and viscosity μ of the two-phase system are:

$$\rho = \rho_w H(\phi) + \rho_a[1 - H(\phi)] \tag{2.6}$$

$$\mu = \mu_w H(\phi) + \mu_a[1 - H(\phi)] \tag{2.7}$$

where ρ_a and μ_a are the density and dynamic viscosity for air, and ρ_w and μ_w are the density and dynamic viscosity for water. The mass of air can be neglected compared to that of water, thus the conservation of mass can be described as:

$$\frac{\partial[\rho_w H(\phi)]}{\partial t} + \nabla \cdot [\rho_w H(\phi)\,\mathbf{u}] = 0 \tag{2.8}$$

Under the assumption of incompressibility, (2.8) is simplified as:

$$\frac{\partial H(\phi)}{\partial t} + \nabla \cdot H(\phi)\,\mathbf{u} = 0 \tag{2.9}$$

However, the solution ϕ to the volume fraction equation (2.4) may not necessarily satisfy the conservation of mass. One approach to solve this issue is to impose a correction ϕ' to ϕ. from the conservation correction equation 2.10, with the assumption ρ_w is a constant [1, 2]:

$$\int_\Omega [H\left(\phi^{n+1} + \phi'\right) - \hat{H}^{n+1}] w d\Omega + \kappa \int_\Omega \nabla\phi' \cdot \nabla w d\Omega = 0,\ \forall w \in W(\Omega), \tag{2.10}$$

where at the $(n+1)th$ time step, ϕ^{n+1} is the numerical solution to (2.4), and $\hat{H}^{n+1}$ is the mass conservative solution to (2.9). $W(\Omega)$ is the weighting space. In this work, the continuous Galerkin finite element spaces is chosen as the weighting space. We solve for ϕ' and use $\phi^{n+1} + \phi'$ for substitution of to satisfy equation (2.10).

2.1.2 Governing Equations

Next we give a summary of the governing equations for the general system. First, we start with the Navier-Stokes equations for incompressible flow:

$$\rho\frac{\partial \mathbf{u}}{\partial t} + \rho\mathbf{u}\cdot\nabla\mathbf{u} + \nabla p - \nabla\cdot 2\mu\nabla^s\mathbf{u} = \rho\mathbf{f} \tag{2.11}$$

$$\nabla\cdot\mathbf{u} = 0 \tag{2.12}$$

where $\mathbf{u}$ is the fluid velocity, p is the pressure, ρ and μ are defined in (2.6) and (2.7), $\mathbf{f}$ is the body force per unit mass, and ∇^s is the symmetric spatial gradient defined as $\nabla^s = \frac{1}{2}\left(\nabla + \nabla^T\right)$. Then the level set function ϕ is solved to determine the fluid subdomains and the interface by

$$\frac{\partial \phi}{\partial t} + \mathbf{u}\cdot\nabla\phi = 0, \text{in } \Omega\times(0,T]. \tag{2.13}$$

The volume fraction is also included:

$$\frac{\partial \hat{H}}{\partial t} + \nabla\cdot\left(\hat{H}\mathbf{u}\right) = 0. \tag{2.14}$$

Two more auxiliary equations for correction are added to the system, since the solution ϕ from 2.13 may not satisfy the mass conservation. The first one is the eikonal equation. It keeps the signed distance properties of the level set function ϕ. :

$$||\nabla\phi_d|| = 1. \tag{2.15}$$

$$\phi_d = 0, \text{on } \Gamma. \tag{2.16}$$

The last equations link the signed distance function ϕ_d to the volume fraction $\hat{H}$ by:

$$\kappa\Delta\phi' = H\left(\phi_d + \phi'\right) - \hat{H} \tag{2.17}$$

$$\nabla\phi' \cdot \mathbf{n} = 0, \text{on } \partial\Omega. \tag{2.18}$$

Note that $\hat{H}$ is the numerical approximation to the volume fraction equations, while H is the exact Heaviside function. The solution for ϕ is updated by $\phi = \phi_d + \phi'$.

2.2 Numerical Methods

2.2.1 Equation Splitting

In section 2.1.1, we formulated a partial differential equation system (2.11) - (2.18). In general, it is expensive to directly solve the fully coupled system. One approach is operator splitting, which is relatively simple in computation without losing much accuracy. In this technique, the system is decomposed first. Then the subproblems are solved separately following a specified order. It allows different time steps in each of the subproblems [1, 2]. The detailed splitting process is described below.

First, assume that the results at the *nth* time step have been computed, and they will be used as initial conditions for the *(n+1)th* time step.

We start with the Navier–Stokes equations to solve for $\mathbf{u}^{n+1}$. The backward Euler method is used, with ϕ^n and $\mathbf{u}^n$ known:

$$\frac{\mathbf{u}^{n+1} - \mathbf{u}^n}{\Delta t} + \mathbf{u}^{n+1} \cdot \nabla\mathbf{u}^{n+1} + \frac{\nabla p^{n+1}}{\rho\left(\phi^n\right)} - \frac{1}{\rho\left(\phi^n\right)}\nabla \cdot 2\mu\left(\phi_n\right)\nabla^s\mathbf{u}^{n+1} = \mathbf{f}^{n+1} \tag{2.19}$$

$$\nabla \cdot \mathbf{u}^{n+1} = 0. \tag{2.20}$$

Next, we use $\mathbf{u}^{n+1}$ for the level set equation and the volume fraction to solve ϕ_0^{n+1} and $\hat{H}_0^{n+1}$ from (2.21) and (2.22) respectively:

$$\frac{\phi_0^{n+1} - \phi^n}{\Delta t} + \mathbf{u}^{n+1} \cdot \nabla \phi_0^{n+1} = 0 \tag{2.21}$$

$$\frac{\hat{H}_0^{n+1} - \hat{H}^n}{\Delta t} + \nabla \cdot \left(\hat{H}_0^{n+1} \mathbf{u}^{n+1} \right) = 0. \tag{2.22}$$

Notice that in this step, $H\left(\phi_0^{n+1}\right) = \hat{H}_0^{n+1}$ may not hold, which means the loss of mass conservation. The error can accumulate over the simulation, and lead to smearing for both ϕ_0 and H_0. To overcome this drawback we re-initialize and assign the signed distance property to ϕ_0^{n+1} by solving the eikonal Equation 2.23 and 2.24 for ϕ_d^{n+1}:

$$||\nabla \phi_d^{n+1}|| = 1 \tag{2.23}$$

$$\phi_d^{n+1} = 0, \text{ on } \Gamma_0 = \{\mathbf{x} | \phi_0^{n+1}(\mathbf{x}) = 0\}. \tag{2.24}$$

Then a correction ϕ' to ϕ_d^{n+1} is made through:

$$\kappa \Delta \phi' = H_\epsilon\left(\phi_d^{n+1} + \phi'\right) - \hat{H}_0^{n+1} \tag{2.25}$$

$$\nabla \phi' \cdot \mathbf{n} = 0, \text{ on } \partial\Omega. \tag{2.26}$$

Here H_ϵ the smoothed approximation to the Heaviside function to avoid discontinuity or singularity, and is defined as:

$$H_\epsilon(\phi) = \begin{cases} 0 & \text{if } \phi \leqslant -\epsilon \\ \frac{1}{2}\left(1 + \frac{\phi}{\epsilon} + \frac{1}{\pi}\sin\left(\frac{\phi\pi}{\epsilon}\right)\right) & \text{if } |\phi| < \epsilon \\ 1 & \text{if } \phi \geqslant \epsilon \end{cases} \tag{2.27}$$

where ϵ is the regularization parameter usually chosen to be the maximum diameter of the element. Lastly, the level set and volume fraction functions at the *(n+1)th* time step are updated by

$$\phi^{n+1} = \phi_d^{n+1} + \phi' \tag{2.28}$$

$$\hat{H}^{n+1} = H_\epsilon \left(\phi_d^{n+1} + \phi' \right). \tag{2.29}$$

Note that in this approach there is no explicit interface reconstruction. It is advantageous compared with traditional level set method which may require complicated topology reconstruction. The reinitialization step generates the signed distance function to determine the interface. The mass conservation is also ensured by the corrections [1, 2]. However, for general meshes, to solve the signed distance function with high order approximations is still an open topic[1, 2].

2.2.2 Discrete Form

Next we discuss the spatial discretization of the system. Take the Navier-Stokes equation as an example. We define the trial function spaces S_u and S_p for the velocity and pressure respectively as [3, 4, 5, 7]:

$$S_u = \{\mathbf{u} | \mathbf{u}(\cdot, t) \in \left(H^1(\Omega_t) \right)^3, \mathbf{u} = \mathbf{g} \; on \; \Gamma_g\} \tag{2.30}$$

and

$$S_p = \{p | p(\cdot) \in L^2(\Omega), p = r \; on \; \Gamma_r\} \tag{2.31}$$

The spaces of test functions are V_u and V_p as

$$V_u = \{\mathbf{w} | \mathbf{w}(\cdot) \in \left(H^1(\Omega) \right)^3, \mathbf{w} = \mathbf{0} \; on \; \Gamma_g\} \tag{2.32}$$

and

$$V_p = \{p | p(\cdot) \in L^2(\Omega), p = 0 \; on \; \Gamma_r\} \tag{2.33}$$

The variational form of (2.11) is to find $\mathbf{u} \in S_u$ and $p \in S_p$ such that $\forall \mathbf{w} \in S_u$ and $q \in V_p$ the following holds:

$$\int_\Omega \mathbf{w} \cdot \rho \left(\frac{\partial \mathbf{u}}{\partial t} + \mathbf{u} \cdot \nabla \mathbf{u} - \mathbf{f} \right) d\Omega + \int_\Omega \nabla^s(\mathbf{w}) : \sigma(\mathbf{u}, p) \, d\Omega - \int_{\Gamma_h} \mathbf{w} \cdot \mathbf{h} \, d\Gamma + \int_\Omega q \nabla \cdot \mathbf{u} \, d\Omega = 0 \tag{2.34}$$

where $\sigma(\mathbf{u}, p) = -p\mathbf{I} + 2\mu\nabla^s(\mathbf{u})$, and $\sigma(\mathbf{u}, p) \cdot \mathbf{n} = \mathbf{h}$ on Γ_h. We use the residual-based variational multiscale stabilized (RBVMS) formulation. The trial and test spaces are decomposed into resolved and unresolved scales using direct sum decompositions [7]:

$$S_u = S_u^h \oplus S_u', \; S_p = S_p^h \oplus S_p' \tag{2.35}$$

$$V_u = V_u^h \oplus V_u', \; V_p = V_p^h \oplus V_p' \tag{2.36}$$

S_u^h, S_p^h, V_u^h and V_p^h are coarse-scale subspaces with finite dimensions. while e are fine-scale subspaces.

The corresponding solutions $\mathbf{u}$ and p, and the test functions $\mathbf{w}$ and q can be rewritten as

$$\mathbf{u} = \mathbf{u}^h + \mathbf{u}', \; p = p^h + p' \tag{2.37}$$

$$\mathbf{w} = \mathbf{w}^h + \mathbf{w}', \; q = q^h + q' \tag{2.38}$$

Multiscale velocity and pressure are modeled as [7]:

$$\mathbf{u}' = \frac{\tau_{SUPG}}{\rho} \mathbf{r}_M \left(\mathbf{u}^h, p^h \right), \tag{2.39}$$

$$p' = -\rho\nu_{LSIC} r_C\left(\mathbf{u}^h\right). \tag{2.40}$$

Here $\mathbf{r}_M\left(\mathbf{u}^h, p^h\right) = \rho\left(\dfrac{\partial \mathbf{u}^h}{\partial t} + \mathbf{u}^h \cdot \nabla \mathbf{u}^h - \mathbf{f}^h\right) - \nabla \cdot \sigma\left(\mathbf{u}^h, p^h\right)$ and $r_C\left(\mathbf{u}^h\right) = \nabla \cdot \mathbf{u}^h$. The stabilization parameters are defined by [5]:

$$\tau_{SUPG} = \left(\frac{4}{\Delta t^2} + \mathbf{u}^h \cdot \mathbf{G}\mathbf{u}^h + C_I \nu^2 \mathbf{G} : \mathbf{G}\right)^{-1/2} \tag{2.41}$$

and

$$\nu_{LSIC} = \left(tr\mathbf{G}\tau_{SUPG}\right)^{-1} \tag{2.42}$$

where $\mathbf{G} = \dfrac{\partial \xi^T}{\partial \mathbf{x}} \dfrac{\partial \xi}{\partial \mathbf{x}}$, $\xi \in R^3$ are the coordinates of the parametric element $\hat{\Omega}^e$.

The RBVMS formulation is to find $\mathbf{u} \in S_u$ and $p \in S_p$ such that $\forall \mathbf{w} \in S_u$ and $q \in V_p$ the following holds:

$$\begin{aligned}
&\int_\Omega \mathbf{w}^h \cdot \rho\left(\frac{\partial \mathbf{u}^h}{\partial t} + \mathbf{u}^h \cdot \nabla \mathbf{u}^h - \mathbf{f}^h\right) d\Omega + \int_\Omega \nabla^s\left(\mathbf{w}^h\right) : \sigma\left(\mathbf{u}^h, p^h\right) d\Omega \\
&- \int_{\Gamma_h} \mathbf{w}^h \cdot \mathbf{h}^h d\Gamma + \int_\Omega q^h \nabla \cdot \mathbf{u}^h d\Omega + \sum_{e=1}^{N} \int_{\Omega_e} \tau_{SUPG}\left(\mathbf{u}^h \cdot \nabla \mathbf{w}^h\right) \cdot \mathbf{r}_M\left(\mathbf{u}^h, p^h\right) d\Omega \\
&+ \sum_{e=1}^{N} \int_{\Omega_e} \tau_{SUPG}\left(\frac{\nabla q^h}{\rho}\right) \cdot \mathbf{r}_M\left(\mathbf{u}^h, p^h\right) d\Omega + \sum_{e=1}^{N} \int_{\Omega_e} \rho\nu_{LSIC} \nabla \cdot \mathbf{w}^h r_C\left(\mathbf{u}^h\right) d\Omega = 0
\end{aligned} \tag{2.43}$$

A discontinuity capturing technique is also used to provide further dissipation and improve the accuracy. We use the YZβ method [6] by adding one term $\sum_{e=1}^{N} \int_{\Omega_e} \nabla w^h \kappa_{dc} \nabla \mathbf{u}^h$ to the left side of the RBVMS semi-discrete form. The parameter is defined as:

$$\kappa_{dc} = \left|Y^{-1}Z\right| \left(\sum_{i=1}^{3} |Y^{-1} \frac{\partial u_i^h}{\partial x_i}|^2\right)^{\beta/2-1} \left(\frac{h_{dc}}{2}\right)^{\beta} \tag{2.44}$$

where $Y = |u^h_{ref}|$ is the reference value and $h_{dc} = 2\left(\sum_{a=1}^{n_e} |\mathbf{j} \cdot \nabla N_a|\right)^{-1}$, $\mathbf{j} = \nabla \mathbf{u}^h / ||\nabla \mathbf{u}^h||$, N_a is the element basis function, n_e is the total number of basis functions, β is 1 for smooth layers or 2 for sharp layers. Z is chosen to be the residual of (2.34):

$$\begin{aligned} Z = \int_\Omega \mathbf{w}^h \cdot \rho \left(\frac{\partial \mathbf{u}^h}{\partial t} + \mathbf{u}^h \cdot \nabla \mathbf{u}^h - \mathbf{f}^h \right) d\Omega + \int_\Omega \nabla^s \left(\mathbf{w}^h \right) : \sigma \left(\mathbf{u}^h, p^h \right) d\Omega \\ - \int_{\Gamma_h} \mathbf{w}^h \cdot \mathbf{h}^h d\Gamma + \int_\Omega q^h \nabla \cdot \mathbf{u}^h d\Omega. \end{aligned} \tag{2.45}$$

For the level set equations, volume fraction equation and redistancing equation, we employ the same RBVMS and YZβ methods. The Continuous Galerkin method is used for the conservation correction equations. The classical Newton's method is utilized for each of the discrete subproblems. For simplified 2D case, the continuous linear or quadratic spaces are used on triangular meshes. In 3D we use continuous piecewise trilinear spaces on a tetrahedral mesh.

2.3 Numerical Experiments for Two-Phase Flow

The numerical experiments for two-phase flow are based on Proteus framework. Proteus is a Python package used for solving numerical models of mechanical processes [57, 58]. It contains various Python modules as solvers to partial differential equations from engineering. It is advantageous in developing and solving coupled systems consisting of Navier-Stokes Equations, advection-diffusion-reaction equations, etc. We assess the model with the wave tank problem in a quasi 2D case, which means the domain is chosen to be one element wide as shown in Figure 2.1. The co-

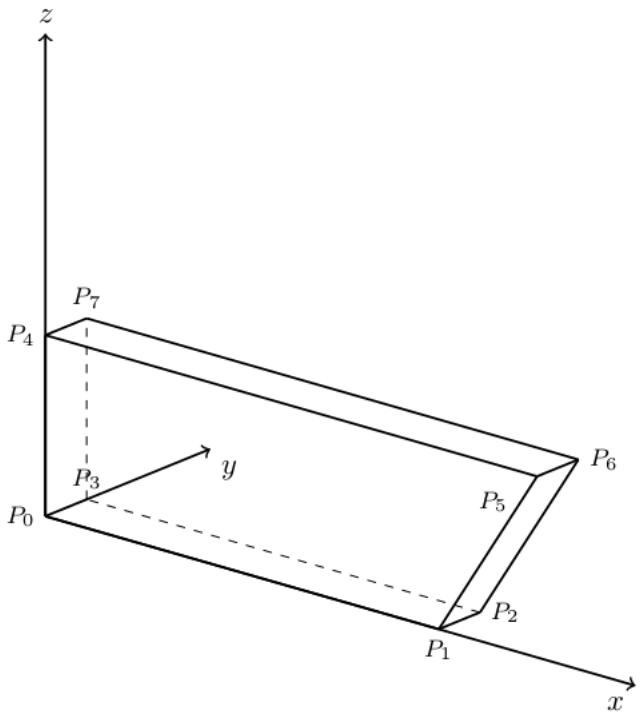

Figure 2.1: Wave Tank Domain

ordinates are set as: $P_0 = (0, 0, 0)$, $P_1 = (2, 0, 0)$, $P_3 = (0, 0.025, 0)$, $P_4 = (0, 0, 0.75)$, $P_5 = (2.5, 0, 0.75)$, $P_6 = (2.5, 0.025, 0.75)$ and $P_7 = (0, 0.025, 0.75)$. The wave is generated at the left boundary $P_0P_4P_7P_3$. We suppose the Plane $P_1P_2P_6P_5$ is the shared interface between the flow and the structure. The width of the domain in y direction is set to be one element wide, i.e. $|P_5P_6| = h_e$ and h_e is the maximum diameter of the elements.

In our first test cases, we set the amplitude (amp) of the wave to be $0.05m$, the wavelength(wl) to be $1.0m$, $h_e = 0.025m$, the time step $\Delta t = T/20s$, T is the wave period, and the total time is 3 periods.

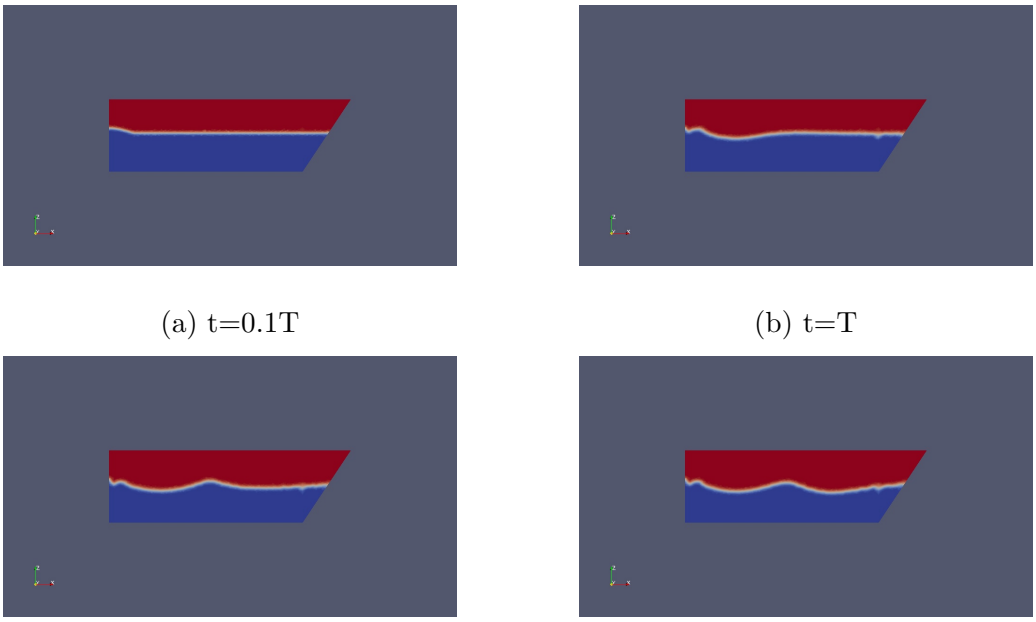

(a) t=0.1T (b) t=T

(c) t=2T (d) t=3T

Figure 2.2: Air-water Volume Fraction at 0.1T, T, 2T, 3T

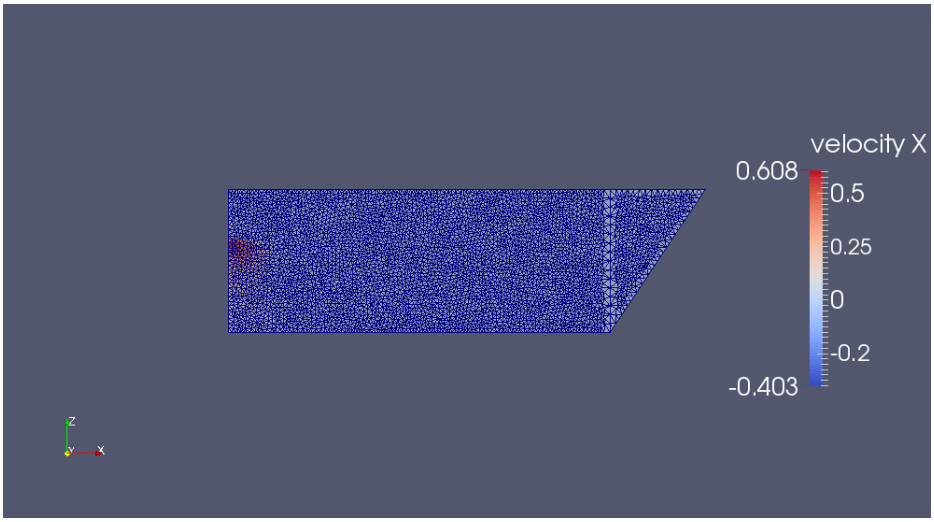

Figure 2.3: Velocities of Air and Water at t=0.1T: m/s

Figure 2.2 demonstrates the change of the volume fraction for the air-water system on the xz plane at t=0.1T, T, 2T and 3T. The top red part represents the air while the bottom blue part represents the water. The flow driven by the wave goes from the left to the right. Next we plot the corresponding water and air velocities in x direction for each of the scenarios in Figure 2.3-2.6.

The stress tensor for incompressible flow is

$$\sigma = -p\mathbf{I} + \mu\left(\nabla\mathbf{u} + \left(\nabla\mathbf{u}^T\right)\right) \tag{2.46}$$

We define $\mathbf{f_p}$ the force due to pressure as

$$\mathbf{f_p} = \int_\Gamma -p\mathbf{I}\cdot\mathbf{n} \tag{2.47}$$

and $\mathbf{f_v}$ the force due to viscosity as

$$\mathbf{f_v} = \int_\Gamma \mu\left(\nabla\mathbf{u} + \left(\nabla\mathbf{u}^T\right)\right)\cdot\mathbf{n} \tag{2.48}$$

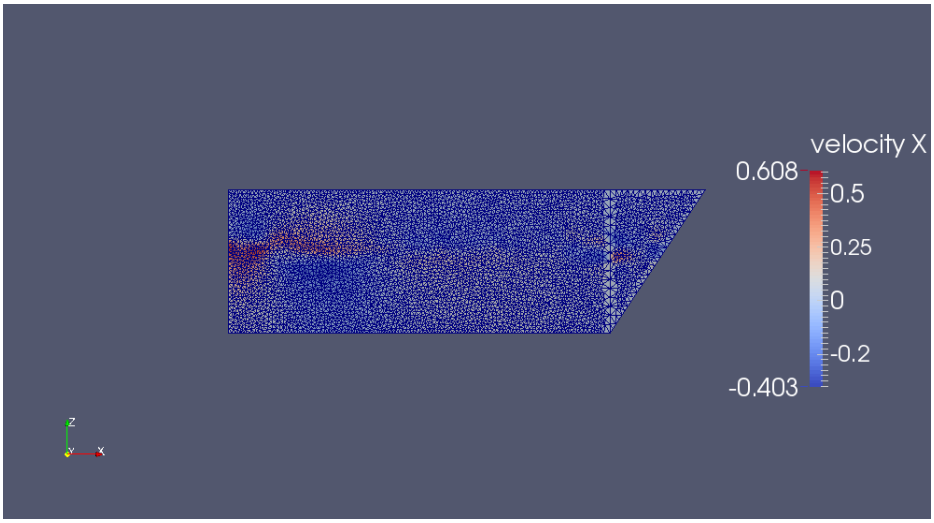

Figure 2.4: Velocities of Air and Water at t=T: m/s

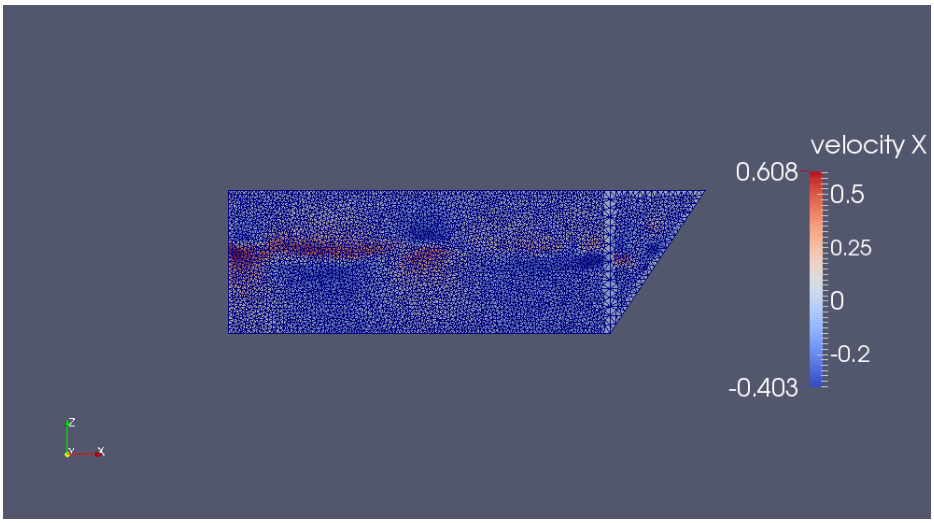

Figure 2.5: Velocities of Air and Water at t=2T: m/s

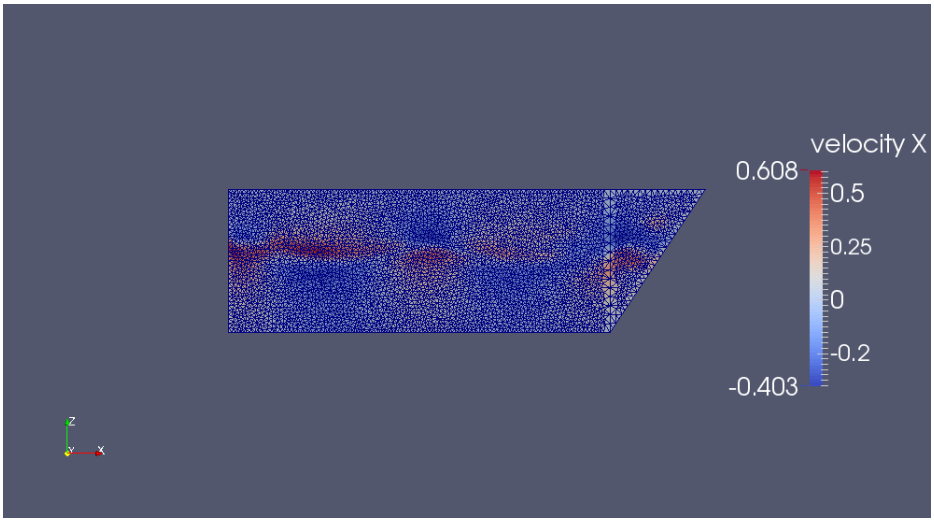

Figure 2.6: Velocities of Air and Water at t=3T: m/s

where Γ represents the interface $P_1P_2P_6P_5$. When the amplitude of the wave is set to be $0.1m$, the wavelength to be $2m$ and the simulation time as 3 periods, Figure 2.7 (a) and (b) show the magnitude change of $\mathbf{f_p}$ and $\mathbf{f_v}$ over time on the interface Γ. From Figure 2.7 we observe that $\mathbf{f_p}$ is of much larger value compared to $\mathbf{f_v}$ in magnitude. In the following analysis we will mainly focus on $\mathbf{f_p}$.

When amplitude is $0.05m$, wavelength is $2.0m$, $\Delta t = T/20$, he =$0.025m$, the time-averaged $\mathbf{f_p}$ are given in Table 1. As the simulation time increases, the components of $\mathbf{f_p}$ tend to converge to $(\mathbf{f_p})_x = 17.2N$ and $(\mathbf{f_p})_z = -11.5N$.

When we reduce the element diameter h_e and keep the same simulation time (10T), we obtain the time-averaged $\mathbf{f_p}$ as in Table 2. From Table 2, we observe that as h_e decreases, $(\mathbf{f_p})_x$ is approaching $17.12N$, and $(\mathbf{f_p})_z$ is approximate to -$11.47N$.

Next let's focus on the forces in the normal direction to the interface. When

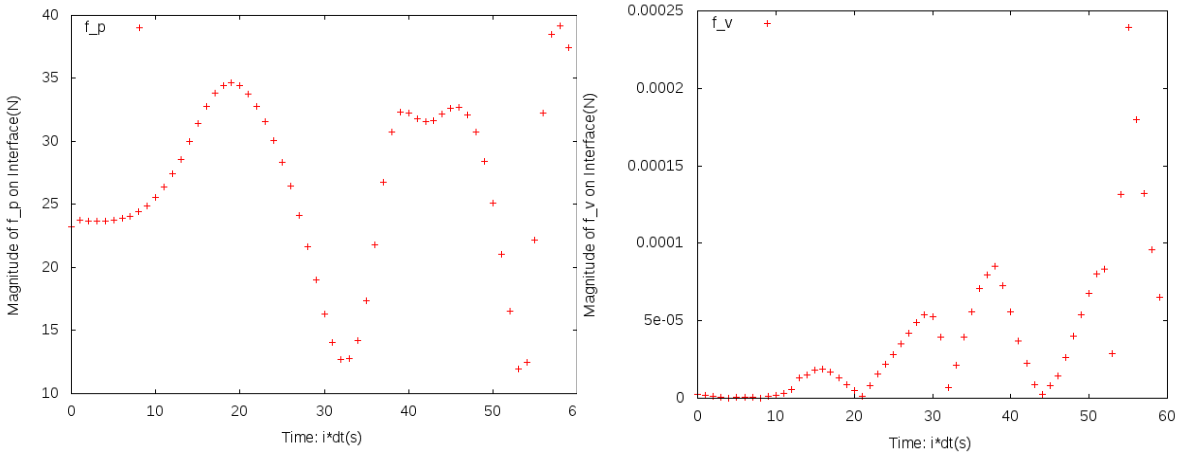

(a) f_p over time

(b) f_v over time

Figure 2.7: Forces from Pressure and Viscosity Over Time

Time	$(\mathbf{f_p})_x$	$(\mathbf{f_p})_y$	$(\mathbf{f_p})_z$
3T	19.0834502871	0.0	-12.5556335247
5T	18.7598711326	0.0	-12.5065807546
10T	17.4873163574	0.0	-11.6582109049
20T	17.2348593020	0.0	-11.5893048272

Table 2.1: Time averaged $\mathbf{f_p}(N)$ for t=3T, 5T, 10T, 20T with amp=0.05m, wl=2m, he=0.025m

he	$(\mathbf{f_p})_x$	$(\mathbf{f_p})_y$	$(\mathbf{f_p})_z$
0.025	17.4873163574	0.0	-11.6582109049
0.020	17.2523857190	0.0	-11.5023461644
0.015	17.1245146086	0.0	-11.4809263945
0.0125	17.1241405343	0.0	-11.4792356689

Table 2.2: Time averaged $\mathbf{f_p}(N)$ over different h_e with amp=$0.05m$, wl=$2m$, t=10T

the amplitude is set to be $0.05m$, h_e=$0.025m$, $t = 3T$, $\Delta t = T/20$, Figure 8 demonstrates how the normal force of $\mathbf{f_p}$ changes over time with different wavelengths. $\mathbf{n} = (\frac{3}{\sqrt{13}}, 0, -\frac{2}{\sqrt{13}})$ is the normal to the interface Γ. Figure 2.8 shows that when the amplitude of the wave remains unchanged, the oscillation of normal force of $\mathbf{f_p}$ becomes more frequent as the wavelength increases. Larger wavelength also leads to larger magnitude of the normal force. These observations match well with experience, i.e. the force is greater with stronger wave.

When the wavelength is fixed to be $4.00m$, $h_e = 0.025m$, $t = 3T$, $\Delta t = T/20$, the figure below demonstrates how the normal force of $\mathbf{f_p}$ changes over time with different amplitudes. The Figure 2.9 shows that when the wavelength of the wave remains unchanged, the amplitude change will not affect the oscillation of $\mathbf{f_p}$ in the normal direction. Larger wave amplitude leads to larger magnitude of the normal force. These observations match with experience.

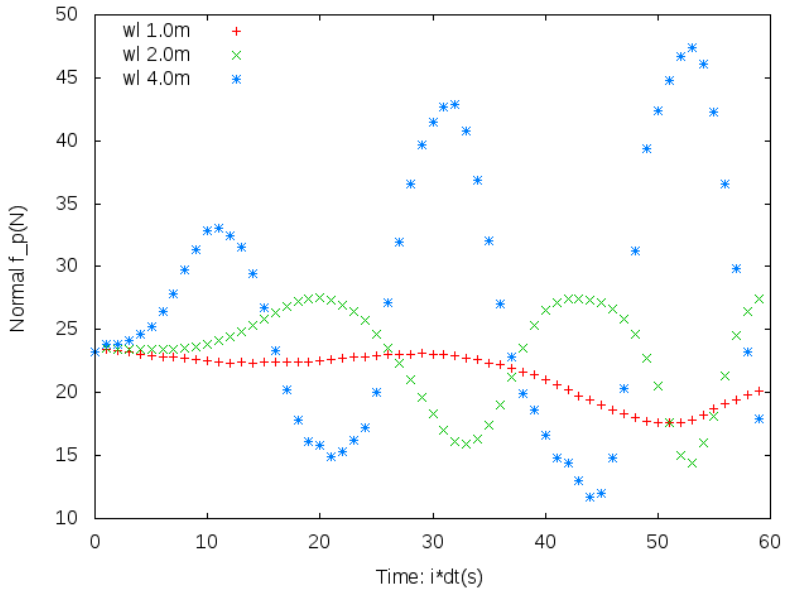

Figure 2.8: Comparison of Normal of $\mathbf{f_p}$ in Different Wavelengths

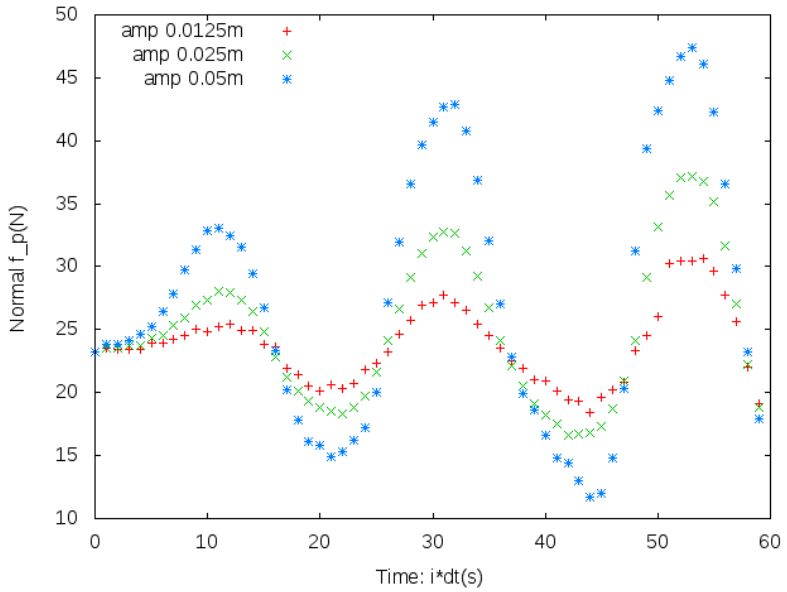

Figure 2.9: Comparison of Normal $\mathbf{f_p}$ in Different Amplitudes

Chapter 3

The Structure Model

Floods are the top one natural disaster in the United States. Levees and floodwalls are common protective structures built in coastal regions. They provide barriers against flooding from storm surge to protect buildings and residents. Most of the protective structures are built by government or public agencies along the coast, extending to hundred of miles in length. Currently there have been levees in all 50 states providing protection to millions of people [34]. In Texas, the levee system mainly consists of the Galveston Seawall, the Freeport Hurricane Protection Structure and the USACE-constructed levees [35].

The differences between floodwalls and levees include materials, designs and applications. Floodwalls are usually built by manmade materials [36]. On the contrary, levees are mostly made of compacted soil to prevent flooding. The designs of the protective structures highly rely on the properties of the protected area, including the flooding type, soil characteristics, etc [36]. The external forces from the water and internal forces from the structure may cause safety concern if the structures are not carefully designed and built. Typically, on the cross section, the floodwalls look like the inverted t-shape (or with enhancement on one side), while the levees have

the trapezoid shape [36]. Overtopping is another main reason to cause failure, but it does not mean the floodwalls should be built high enough. With limited budget, a proper design is preferred to reduce the unnecessary high cost from construction to maintenance. Due to the higher cost and larger land required for construction, levees are used less common than floodwalls as the residential flooding protective measure[36]. In this work, we will focus more on the floodwall model and simulate the floodwall behavior under waves and surge.

In this section, we will first start with the simplest elastic models for the floodwall. Both linear elastic and hyperelastic models will be discussed. As mentioned in the introduction section, the lack of proper soil model was the primary reason for levee failure in the Lakeview neighborhood and the Gentilly neighborhood [40, 41]. So it is necessary to include the supporting soil under and around the floodwall as part of the structural model. Plasticity is used to best described the soil deformation when external forces are applied. In the soil-floodwall model, we assume there is no separation on the interface between the soil and the floodwall.

3.1 Elastic Models

3.1.1 Background

Solid objects will deform when forces are applied on them. A natural quantity of interest in structural mechanics is the displacement. The simplest model to this problem is elasticity. If the material is elastic, the object will return to its original shape when the forces are removed. For simplicity, we usually assume linear elastic-

ity when the deformations are small. In the linear elastic model, the relationships between the components of stress and strain are linear. Linear elasticity assumption is reasonable for many engineering materials and engineering design scenarios, thus used extensively in structural analysis. For more general cases, we will consider hyperelastic models where the stress-strain relationship is derived from the strain energy density function. Hyperelasticity also allows us to consider potentially large deformation of the material.

3.1.2 Elasticity

Under the Lagrangian framework, a fixed material point $\mathbf{x_0}$ has be chosen at $t = 0$. The position of the point at time t is determined by a bijection:

$$\mathbf{x(t)} = \mathbf{\Phi}(\mathbf{x_0}, t). \tag{3.1}$$

The displacement is defined by

$$\mathbf{u}(\mathbf{x_0}, t) = \mathbf{\Phi}(\mathbf{x_0}, t) - \mathbf{x_0}. \tag{3.2}$$

The general governing equations for elastic materials are derived from the Newton's second law:

$$\nabla \cdot \sigma + \mathbf{F} = \rho \ddot{\mathbf{u}} \tag{3.3}$$

In linear elastic models, the stress tensor $\sigma(\mathbf{u})$ is derived as:

$$\sigma(\mathbf{u}) = 2\mu \nabla^s \mathbf{u} + \lambda tr(\nabla^s \mathbf{u}) \mathbf{I_n}, \tag{3.4}$$

where

$$\nabla^s \mathbf{u} = \frac{1}{2}(\nabla \mathbf{u} + (\nabla \mathbf{u})^T), \tag{3.5}$$

$$\lambda = \frac{E\nu}{(1+\nu)(1-2\nu)}, \tag{3.6}$$

$$\mu = \frac{E}{2(1+\nu)}. \tag{3.7}$$

E is the Young's modulus and μ is the Poisson's ratio. We choose E=10GPa, and ν=0.3 in the elastic models.

For large deformations, hyperelastic models are often used. We define

$$\mathbf{f} = grad\, \mathbf{\Phi}. \tag{3.8}$$

The Green Lagrange tensor is denoted as

$$\mathbf{e} = \frac{1}{2}(\mathbf{f}^T\mathbf{f} - \mathbf{I}). \tag{3.9}$$

The St. Venant-Kirchhoff model is employed for the energy functional ψ:

$$\psi(\mathbf{e}) = \mu tr(\mathbf{e}^2) + \frac{\lambda}{2}(tr(\mathbf{e}))^2, \tag{3.10}$$

where μ and ψ are positive Lamé constants. Therefore, the first Piola-Kirchhoff tensor σ is

$$\sigma = \mathbf{f} \cdot \frac{\partial \psi(\mathbf{e})}{\partial \mathbf{e}} = \mathbf{f} \cdot (2\mu\mathbf{e} + \lambda tr(\mathbf{e})\mathbf{I}). \tag{3.11}$$

3.2 Numerical Experiments for Elasticity

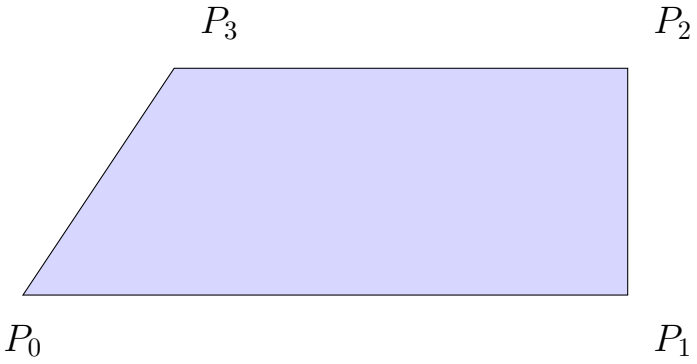

We use the traditional continuous Galerkin finite element method in discretization of the 2D case, we set the domain as above with P_0=(2.0, 0.0), P_1=(4.0, 0.0), P_2=(4.0, 0.75), P_3=(2.5, 0.75). All of the coordinates are in meters. We assume P_0P_3 is the common interface between the flow and the structure. Forces from the flow will be passed to the structure and cause deformation through P_0P_3. The bottom P_0P_1 keeps unmoved. For the 2D test, we set the boundary conditions as:

$$\begin{aligned} \sigma \cdot \mathbf{n} &= (100000.0, 0.0)^T, \text{ on } P_0P_3 \\ \sigma \cdot \mathbf{n} &= (0.0, 0.0)^T, \text{ on } P_1P_2 \text{ and } P_2P_3 \\ \mathbf{u} &= (0.0, 0.0)^T, \text{ on } P_0P_1 \end{aligned}$$

We start with the simplest linear elastic case in steady state, i.e. $\ddot{\mathbf{u}} = 0$. The deformation $\mathbf{u}$ in 2D is shown in Figure 3.1.

From Figure 3.1, it is easy to tell the largest deformation happens at the upper left corner. In the bottom right region, there is barely deformation. The deformation is larger on the left than on the right. These observations match well

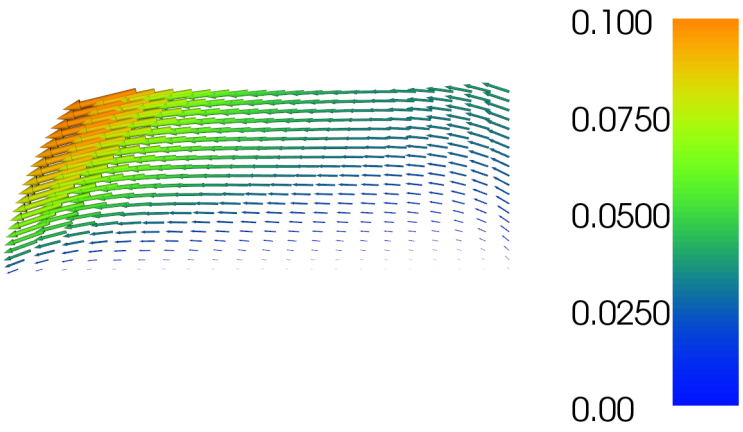

Figure 3.1: Linear Elastic Deformation in 2D: meters

with our expectation and experience. Next, we proceed to learn about the time-dependent case. The domain and boundary conditions are set as the same as for the steady state case. Therefore we set a changing external force on P_0P_3 as $F_x = 0.9 \times 10^4 sin(2t)N, F_y = 1.2 \times 10^4 sin(2t)N$. The time step is $\Delta t = 0.01s$ and total simulation time $t \in [0, 1]s$. Figure 3.2 to Figure 3.5 show the displacement at $t = 0s$, $t = 0.3s$, $t = 0.6s$ and $t = 1s$.

From Figure 3.3, we observe that deformation first happens along the common interface and the nearby regions. After another 0.3s, due to the elastic property of the material, large deformation is captured on the right part, as seen in Figure 3.4. When $t = 1$s, the deformation on the right becomes smaller, while the displacement near the interface are getting larger, compared to the solution at $t = 0.6$s. The whole process demonstrates how the stress is transferred from the interface to the interior and causes the displacement on each section of the material with time.

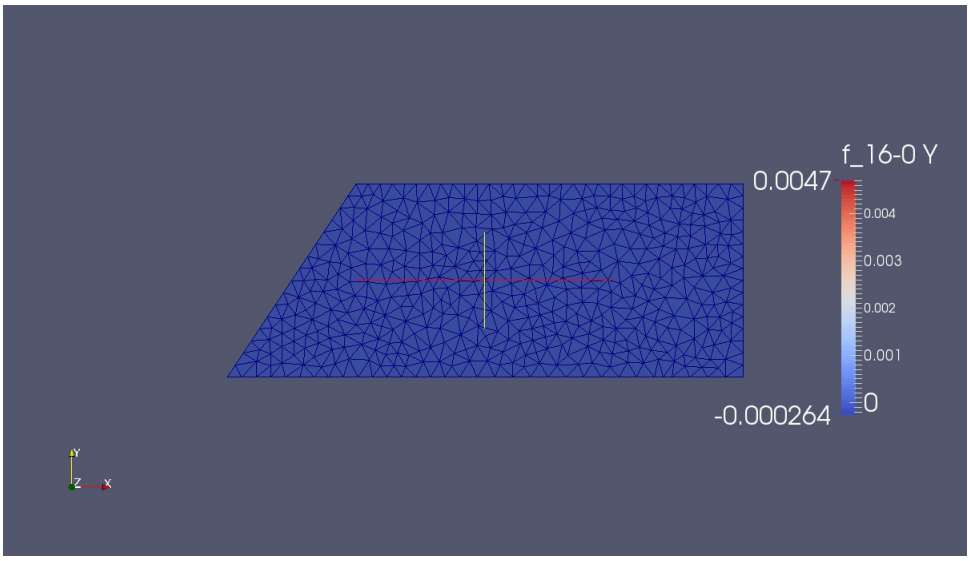

Figure 3.2: Displacement of Linear Elasticity at t=0s: m

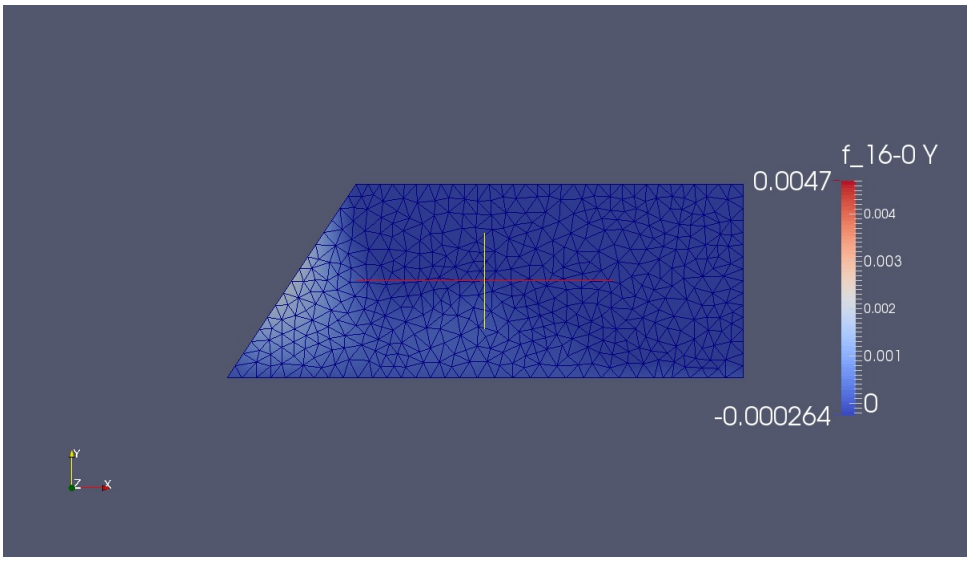

Figure 3.3: Displacement of Linear Elasticity at t=0.3s: m

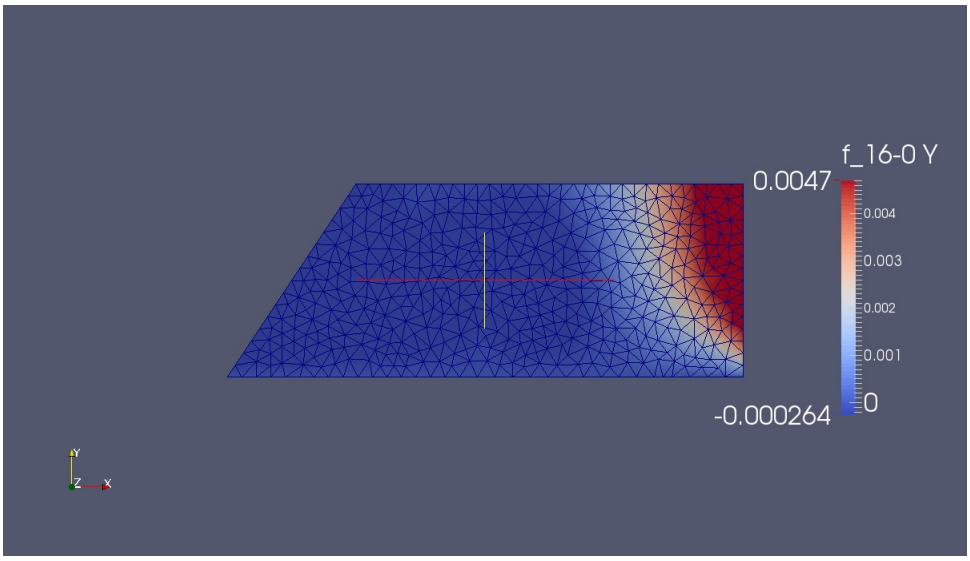

Figure 3.4: Displacement of Linear Elasticity at t=0.6s: m

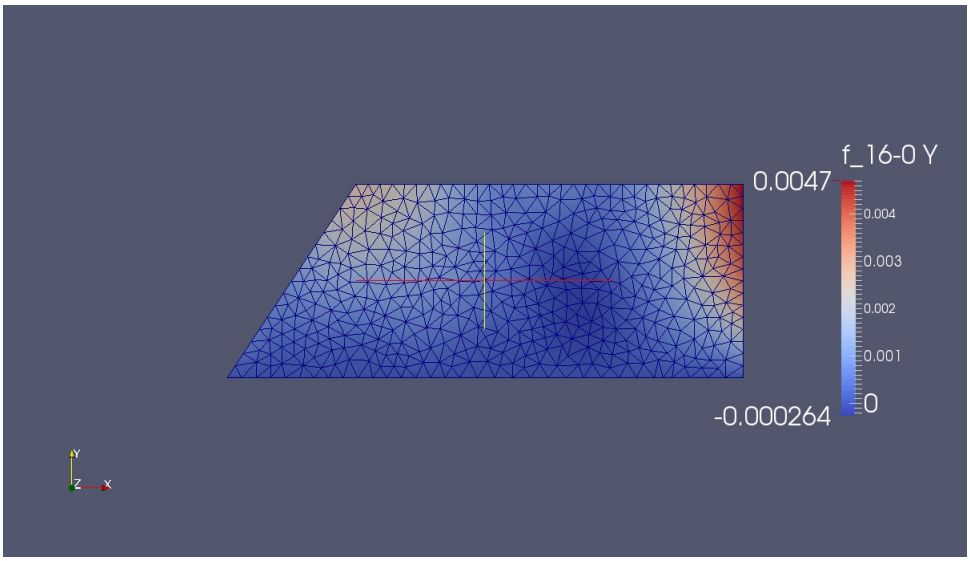

Figure 3.5: Displacement of Linear Elasticity at t=1s: m

3.3 Floodwall

3.3.1 Introduction

In the elastic models, the structure is assumed with single material, i.e. concrete. We did not consider the impact of the supporting soil. This is reasonable to neglect the soil when the structure is light and the soil is stiff [45]. In realistic engineering design, floodwalls are mostly made of manmade materials with relatively large density. The improper estimation of soil strength may lead to floodwall design defects and result in failure, as seen in Hurricane Katrina [40, 41]. Our interest mainly focus on the Galveston Bay Area, so the soil property in this area should be paid special attention to. As referred in the soil survey of Galveston County from the United States Department of Agriculture and Soil Conservation Service [66], Galveston Island is known as sandy, made up mostly of sand-sized particles, with some amounts of finer mud and gravel-sized sediments. The equivalent soil type is SM, which stands for silty sand. The physical properties of both the floodwall and the soil in this specified area determine the necessity of including soil as part of the structural model.

3.3.2 Floodwall Types

Currently, there are four common floodwall types: gravity wall, cantilever wall, buttress and counterfort [14, 36]. The gravity floodwall relies on the weight of the structure. It resists overturning by its heavy weight, as the name suggests. This type of floodwall is rather easy to construct. The construction cost increases as the

wall height goes up. It is commonly used for low height walls. For higher heights a cantilever wall is more often used. The cantilever wall is designed to keep the center of mass to the back side of the wall. Other floodproofing methods and backfilling may also help to stabilize the floodwall [14, 36]. It is a traditional and relatively safe design to prevent flooding. The other two types buttress and counterfort are the enhanced versions of the cantilever wall. The buttress wall is nearly the same as the counterfort wall, except the opposite locations of the extra supporting walls. The counterfort wall is more often used than the buttress wall, since the supporting portion is placed along the water-structure interface thus saving usable space behind the wall [36]. A counterfort wall is built in areas with severe flooding in historic record to counteract the very high pressures more effectively. It is commonly used for wall height larger than 20 feet [36].

From the FEMA construction guidelines, the floodwall height should be determined by the Base Flood Elevation (BFE) of the protected area. BFE is the expected flooding elevation within 1% probability in any year of a 100-year flood [14, 36]. Referring to the FEMA risk map database, BFEs are varied along the coastline in the Galveston Bay area, ranging from 12 to 17 feet. To achieve the best protection effect we choose BFE as 17 feet in the following discussion, which also suggests that a cantilever wall will be used in the modeling.

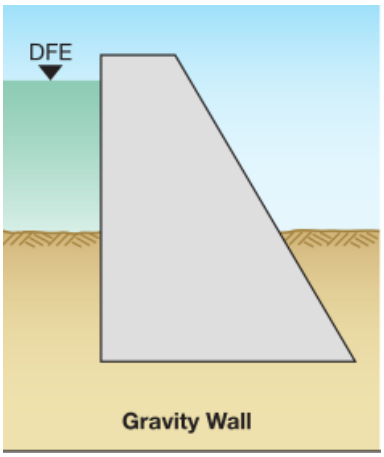

(a) Gravity Wall

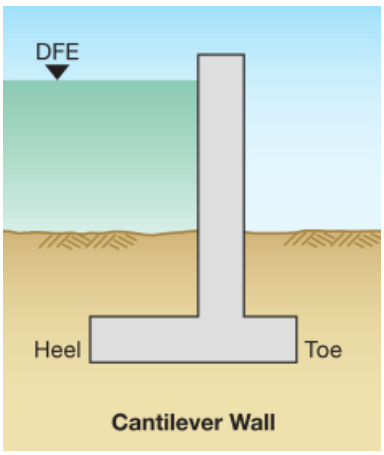

(b) Cantilever Wall

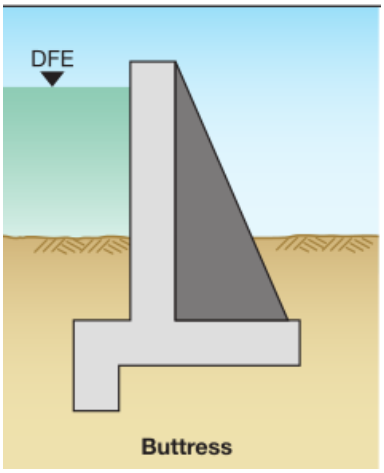

(c) Buttress Wall

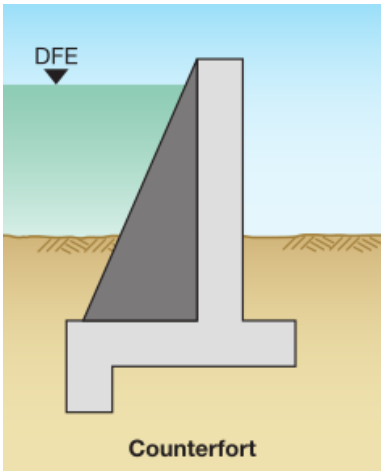

(d) Counterfort Wall

Figure 3.6: Four Types of Floodwall: Gravity, Cantilever, Buttress, Counterfort (FEMA Report [14] 2013)

3.3.3 Failure Analysis

Based on the Federal Emergency Management Agency (FEMA) report 232, there are two main factors to evaluate if the design of current existing floodwall meets safety standards. The stability of the floodwall is assessed for mainly two different reasons of failure. The first one is sliding. When the sum of lateral forces is greater than the total resisting forces, sliding may happen. The other factor is overturning around the foundation toe. This happens when the sum of overturning moments is greater than the sum of resisting moments. In this section, we will investigate the two factors of safety arising from the two concerns. The equations for factors of safety are formulated first, followed by test cases with different wave and floodwall size parameters.

The most common used flood wall is the cantilever floodwall. The geometric parameters of the floodwall needed in the computation are marked in Figure 3.7. Here BFE is the base flood elevation and DFE is the designed flood elevation. DFE is usually set to be 1 foot larger than BFE.

We start with the sliding forces. Let f_{sta} be the lateral hydrostatic force from the water, f_{diff} the differential soil and water force due to the free-standing water and saturated soil, f_d the hydrodynamic force acting on the structure from the flow, and f_S the total sliding forces. S is the soil density and γ_ω is the water density. The forces are modeled as [36]:

$$f_{sta} = \frac{1}{2}\gamma_\omega H^2, \tag{3.12}$$

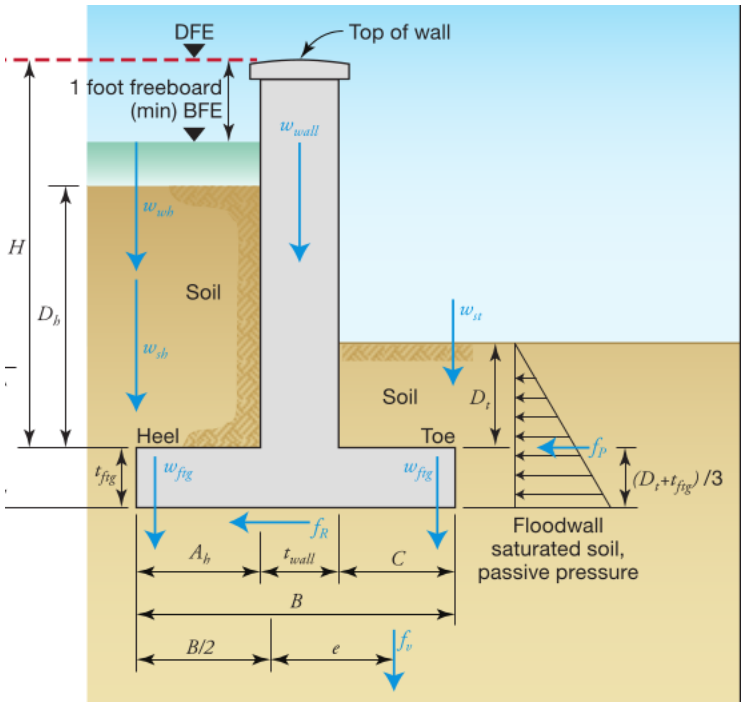

Figure 3.7: Parameters in Floodwall Design (FEMA Report [14] 2013)

$$f_{diff} = \frac{1}{2}\left(S - \gamma_\omega\right) D_h^2. \tag{3.13}$$

H is the distance from the top of wall to the top of floodwall heel. D_h is the depth of soil above the heel. f_d is the hydrodynamic force on the interface obtained from the flow subproblem. So in summary, the total sliding force is represented as:

$$f_S = f_{sta} + f_{diff} + f_d. \tag{3.14}$$

Next let's take a look at the resisting forces. Let f_{buoy} be the total force due to buoyancy, f_{buoy1} be the buoyancy force due to hydrostatic pressure at the floodwall heel, and f_{buoy2} be the buoyancy force due to hydrostatic pressure at the toe. γ_w is the density of water. H is the depth from floodwall top to toe. D_t is the depth of soil above the floodwall toe. A_h is the floodwall heel width. C is the floodwall toe width. According to [36],

$$f_{buoy1} = \gamma_1 \left[(H) \left(\frac{1}{2} t_{wall} \right) + \left(A_h + \frac{1}{2} t_{wall} \right) (t_{ftg}) \right] \tag{3.15}$$

$$f_{buoy2} = \gamma_1 \left[(D_t) \left(\frac{1}{2} t_{wall} \right) + \left(C + \frac{1}{2} t_{wall} \right) (t_{ftg}) \right] \tag{3.16}$$

and

$$f_{buoy} = f_{buoy1} + f_{buoy2}. \tag{3.17}$$

The gravity forces are decomposed due to different sources. Let w_{wall} be the weight of floodwall(lb/lf), w_{ftg} the weight of the footing(lb/lf), w_{st} the weight of soil over the toe(lb/lf), w_{sh} the weight of the soil over the heel(lb/lf), w_{wh} the weight

of water above the heel, and w_G the total gravity forces. t_{wall} is the floodwall width. t_{ftg} is the height of floodwall heel. B is the total width of floodwall footing. Each of the components of w_G is formulated as [36]:

$$w_{wall} = Ht_{wall}S_g \tag{3.18}$$

$$w_{ftg} = Bt_{ftg}S_g \tag{3.19}$$

$$w_{st} = C(D_t)\gamma_{soil} \tag{3.20}$$

$$w_{sh} = A_h(D_h)(\gamma_{soil} - \gamma_\omega) \tag{3.21}$$

$$w_{wh} = A_h(H)(\gamma_\omega) \tag{3.22}$$

and

$$w_G = w_{wall} + w_{ftg} + w_{st} + w_{sh} + w_{wh}. \tag{3.23}$$

Now the friction force f_{fr} is computed as:

$$f_{fr} = C_f(w_G - f_{buoy}). \tag{3.24}$$

The saturated soil force over the toe is formed as:

$$f_p = \frac{1}{2}\left[\kappa_p\left(\gamma_{soil} - \gamma_\omega\right) + \gamma_\omega\right]\left(D_t + t_{ftg}\right)^2. \tag{3.25}$$

The resisting force f_R is then computed by:

$$f_R = f_{fr} + f_p. \tag{3.26}$$

The factor of safety against sliding is defined as:

$$FS_{sl} = \frac{f_R}{f_S}. \tag{3.27}$$

When $FS_{sl} \geqslant 1.5$, it means the structure is safe against sliding.

The overturning moments rise from f_{sta}, f_{diff}, f_{buoy1}, f_{buoy2} and f_d. The sum of the overturning moments is [36]:

$$\begin{aligned} M_O = \quad & f_{sta}\left(\frac{H + t_{ftg}}{3}\right) + f_{diff}\left(\frac{D_h + t_{ftg}}{3}\right) + f_{buoy1}\left(\frac{2B}{3}\right) \\ & + f_{buoy2}\left(\frac{B}{3}\right) + f_d\left(\frac{H - D_h}{2} + D_h + t_{ftg}\right) \end{aligned} \tag{3.28}$$

The resisting moments are from the gravity forces and f_p. The total resisting moments M_R is formed as [36]:

$$M_R = w_{wall}\left(C + \frac{t_{wall}}{2}\right) + w_{ftg}\left(\frac{B}{2}\right) + w_{st}\left(\frac{C}{2}\right) + w_{sh}\left(B - \frac{A_h}{2}\right) + f_p\left(\frac{D_t + t_{ftg}}{3}\right) \tag{3.29}$$

Factor of safety against overturning is then computed as [36]:

$$FS_{ov} = \frac{M_R}{M_O}. \tag{3.30}$$

When$FS_{ov} \geqslant 1.5$, it means the structure is safe against overturning.

To be closer to realistic waves, we improve the two-phase flow model by introducing multiple random waves instead of single wave. Only the peak value of

wavelength and period are set to be fixed. In the following two tests, we choose the total runtime to be 20s. The peak wavelength is 0.1m and the peak period is 2.0s. The initial water depth is 0.5 m. The flow region is set the same as in Section 2.3. In Test 1, $h_e = 0.1m$ and $\Delta t = 0.05s$. In Test 2, $h_e = 0.05m$ and $Deltat = 0.025s$.

The floodwall design parameters are chosen as: $t_{ftg} = 1ft$, $A_h = 5ft$, $t_{wall} = 1ft$, $C = 2ft$, $D_h = 3ft$, $D_t = 3ft$, $H = 6ft$. The soil type in Galveston area is of silty fine sands so that the fraction coefficient $C_f = 0.55$ and the passive soil pressure gradient is $k_p = 3.7$ [66].

Now let us take a look at the force due to pressure in the two tests first, as seen in Figure 3.8 and Figure 3.9:

Notice that the force f_d in the two tests are not the same due to the random wave generator. The waves in Test 1 and Test 2 may vary though the peak wavelength and period are fixed. The factors of safety about sliding and overturning for both of the test cases are also analyzed in Figure 3.10 and Figure 3.11.

The factors of safety are dependent on the values of the geometric parameters. From Figure 3.10 and Figure 3.11, we tell the floodwall is safe both against sliding and overturning. The choice of the floodwall design parameters is safe under this wave. If we reduce the footing of the floodwall by decrease the length of t_{ftg}, A_h or C, failure may happen at any time. To be more specific, if we use the same wave settings thus the same hydrodynamic force profiles as in Test 2, but change $A_h = 4ft$ and $C = 1ft$, the risk of overturning is encountered at the first time step where $FS_{ov} = 1.39474$. If we change $A_h = 4ft$ and $t_{wall} = 0.5ft$, $C = 2ft$ while

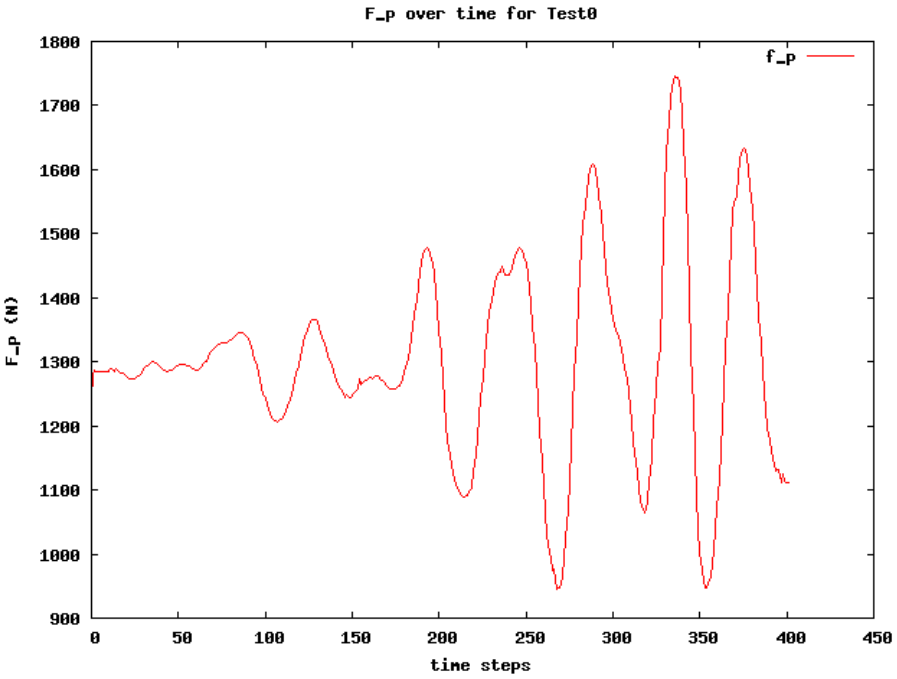

Figure 3.8: f_p Over Time for Test 1

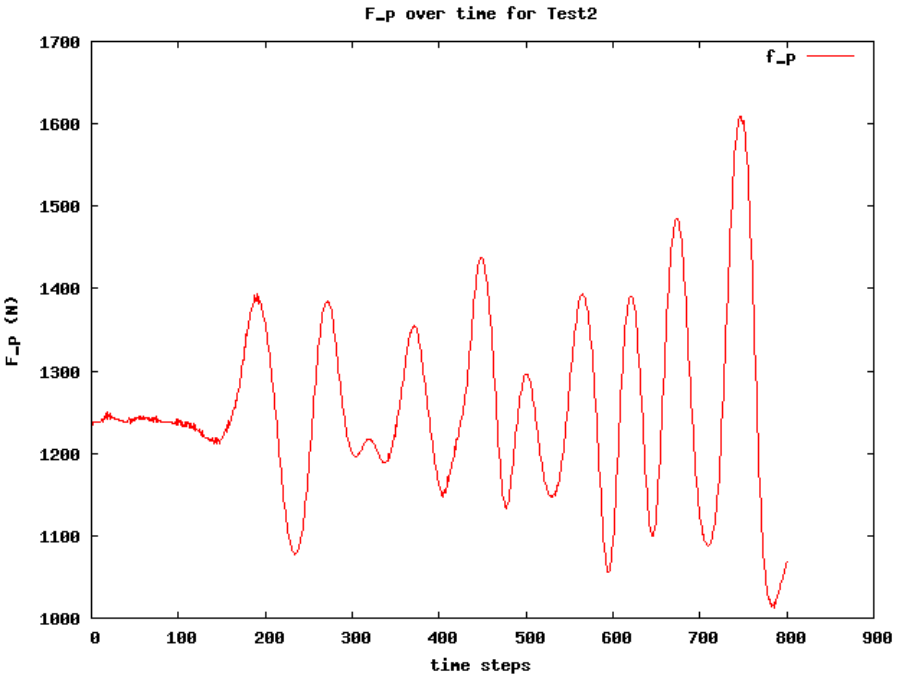

Figure 3.9: f_p Over Time for Test 2

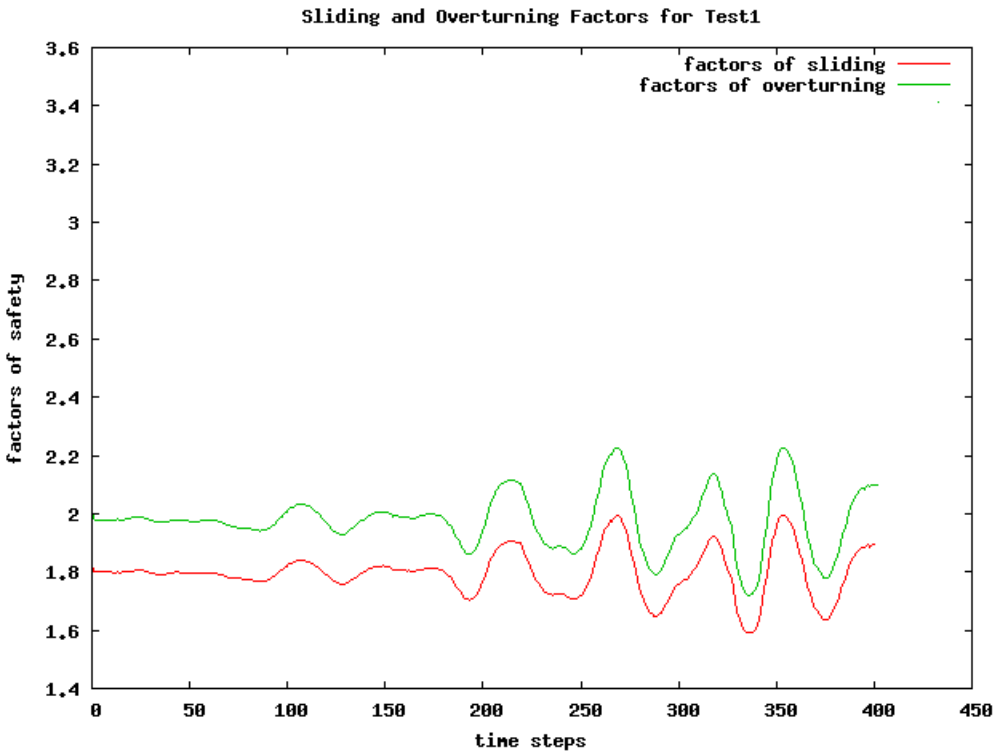

Figure 3.10: Factors of Safety Over Time for Test 1

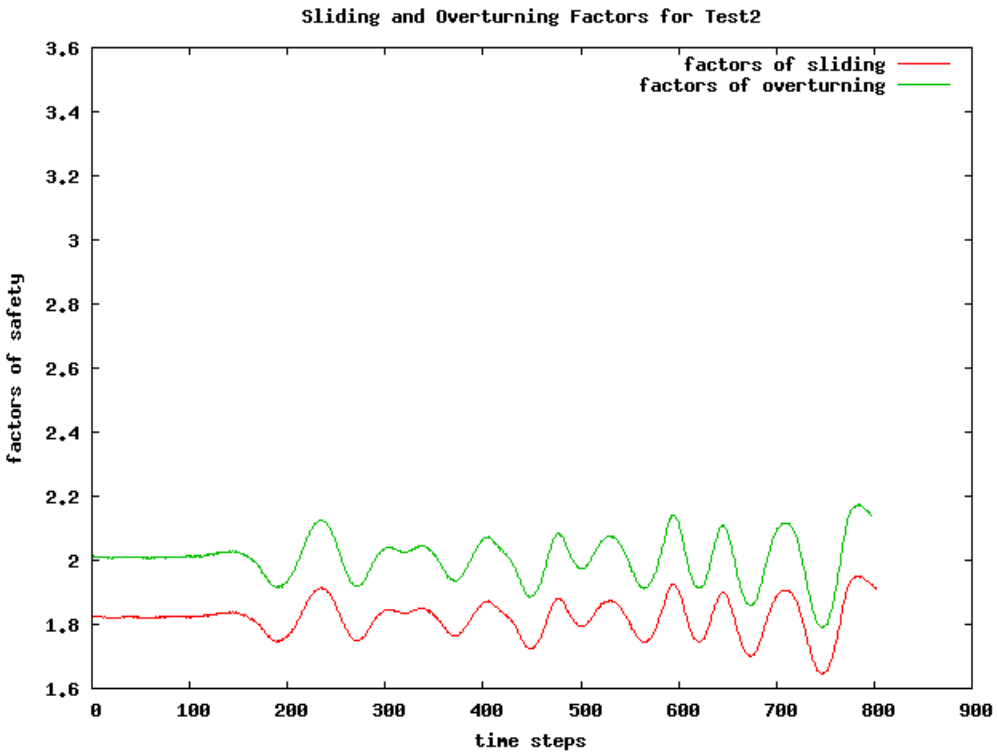

Figure 3.11: Factors of Safety Over Time for Test 2

the other variables keep unchanged, at the $742th$ time step, the factor of overturning reaches 1.49726, less than the safety limit 1.5. Moreover, when the floodwall material density or fraction coefficients are chosen to different values, the risk of sliding may be met in the middle of runtime.

In summary, the factors of safety rely on the hydrodynamic forces from the flow, the values of the floodwall parameters and soil properties. The two factors provides safety check when choosing geometries for the floodwall and soil region under designed wave and flooding level.

3.4 Soil As Part of the Model

3.4.1 Elastic Model for the Soil

As discussed in Section 3.3.1, we will include the soil in our structural model. To simplify the model complexity, we assume no gap or separation between the soil and floodwall will happen. The soil and floodwall system will be computed simultaneously in one bigger domain. The soil and floodwall subdomains are separated as the material discontinuity. Smaller Young's modulus is observed in the soil than in the floodwall. That is why we will use a much finer mesh in soil subdomain than in floodwall subdomain. The max element area of floodwall subdomain is $10^{-2}m^2$, while that of the soil subdomain is $6.25 \times 10^{-4}m^2$. The choice of floodwall and soil region size is the same as in Test 1 and Test 2 from Section 3.3.3.

We set $\rho_s = 1600kg/m^3$ as the soil density [66], $E_s = 0.016GPa$ as the

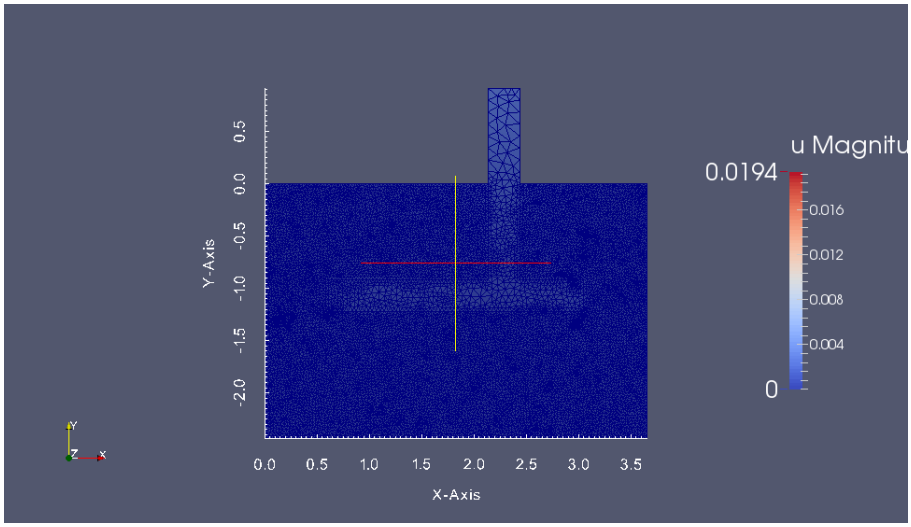

Figure 3.12: Deformation at t=0s: m

Young's modulus for soil, $\rho_f = 2000kg/m^3$ as the floodwall density, and $E_f = 17GPa$ the Young's modulus for floodwall. Considering the huge difference between the two Young's moduli, hyperelasticity is used for soil subdomain and linear elasticity is used for the floodwall. The total simulation time is $20s$, and time step $\Delta t = 0.1s$. Figure 3.12 to Figure 3.17 show the deformation of the soil-floodwall over time. A constant traction (-100000.0, 0.0)N is applied on the top left side of the floodwall above the soil surface. The boundary conditions are:

$$\mathbf{u} = \mathbf{0}, \text{on the bottom,} \tag{3.31}$$

$$\sigma \cdot \mathbf{n} = (-100000.0, 0.0)^T, \text{on interface,} \tag{3.32}$$

$$\sigma \cdot \mathbf{n} = (0.0, 0.0)^T, \text{elsewhere.} \tag{3.33}$$

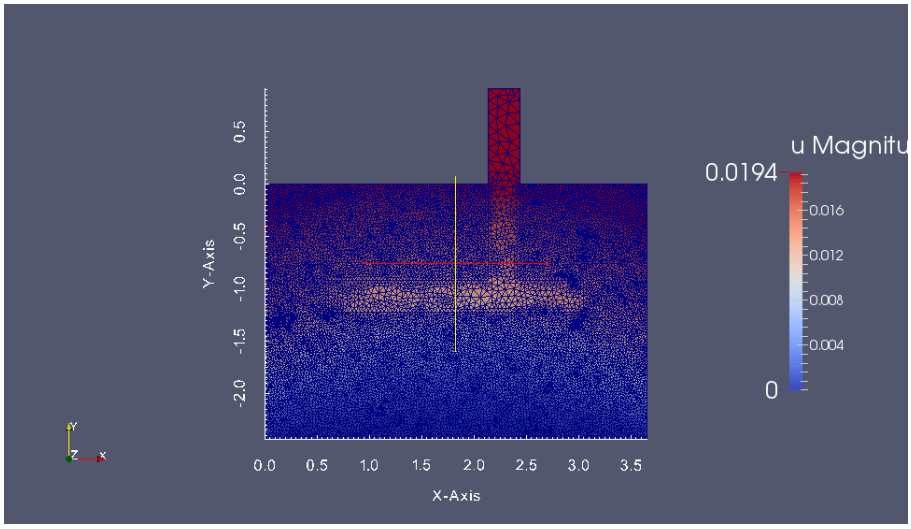

Figure 3.13: Deformation at t=2.5s: m

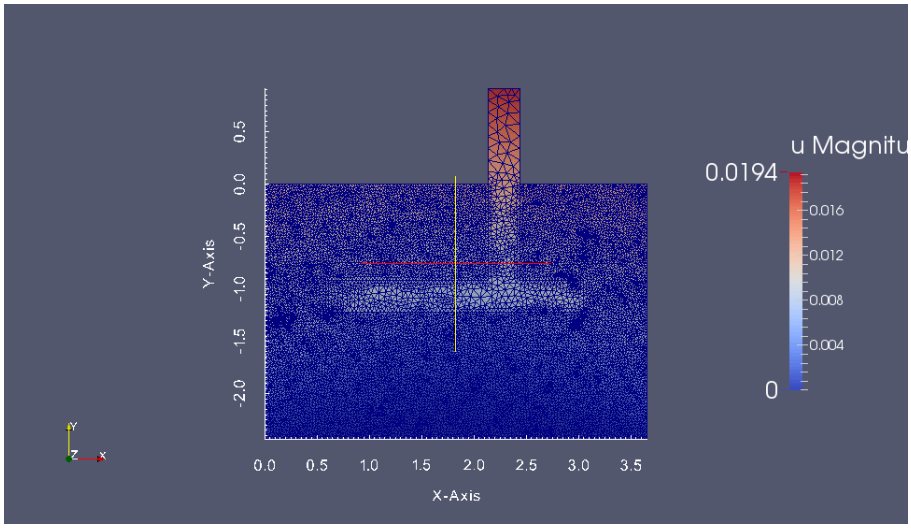

Figure 3.14: Deformation at t=5.0s: m

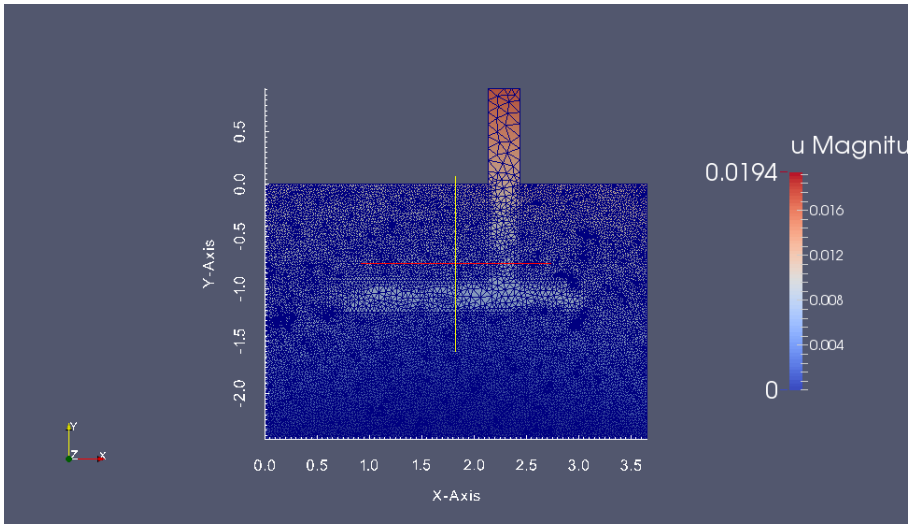

Figure 3.15: Deformation at t=7.5s: m

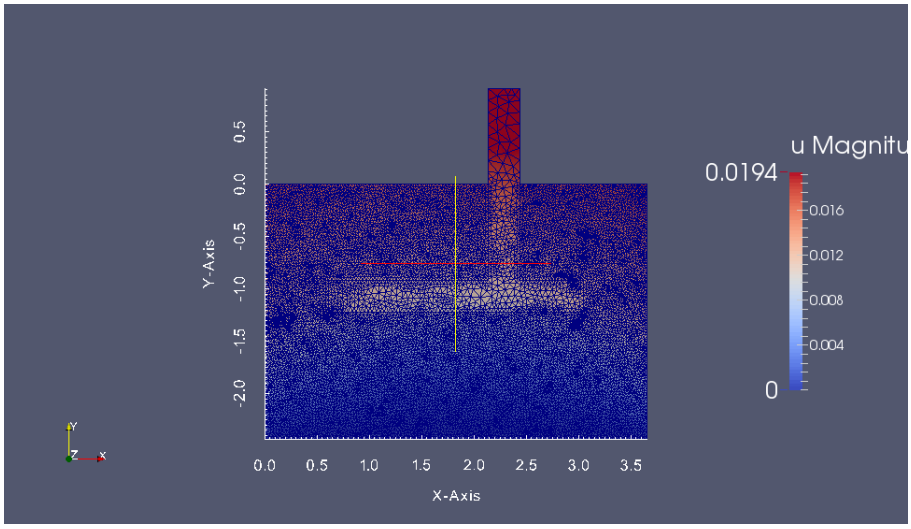

Figure 3.16: Deformation at t=10.0s: m

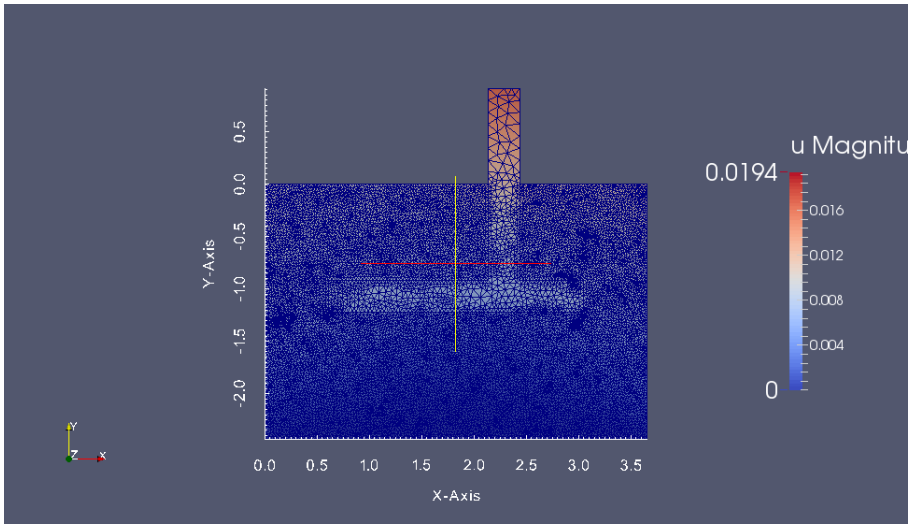

Figure 3.17: Deformation at t=12.5s: m

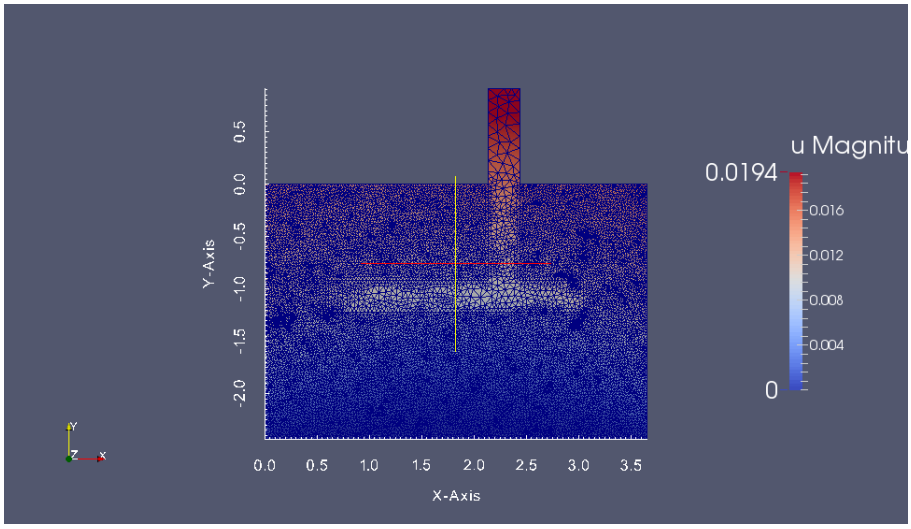

Figure 3.18: Deformation at t=15.0s: m

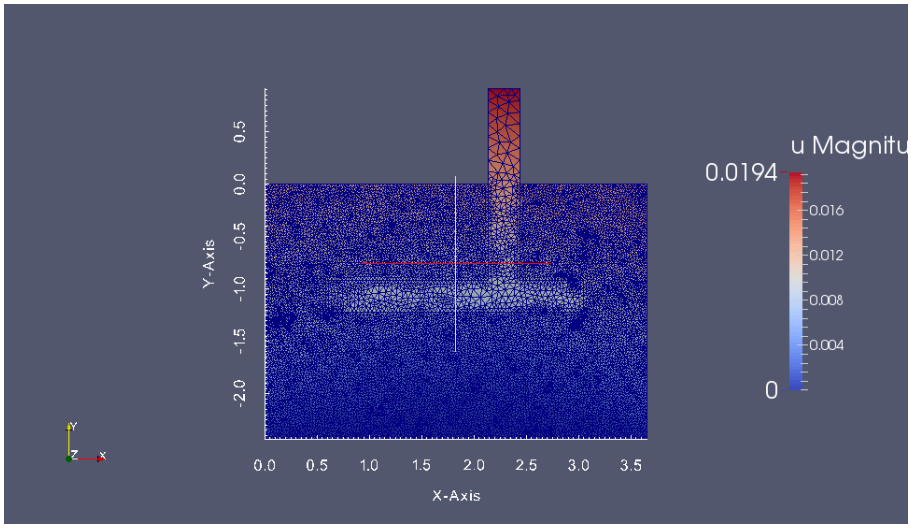

Figure 3.19: Deformation at t=17.5s: m

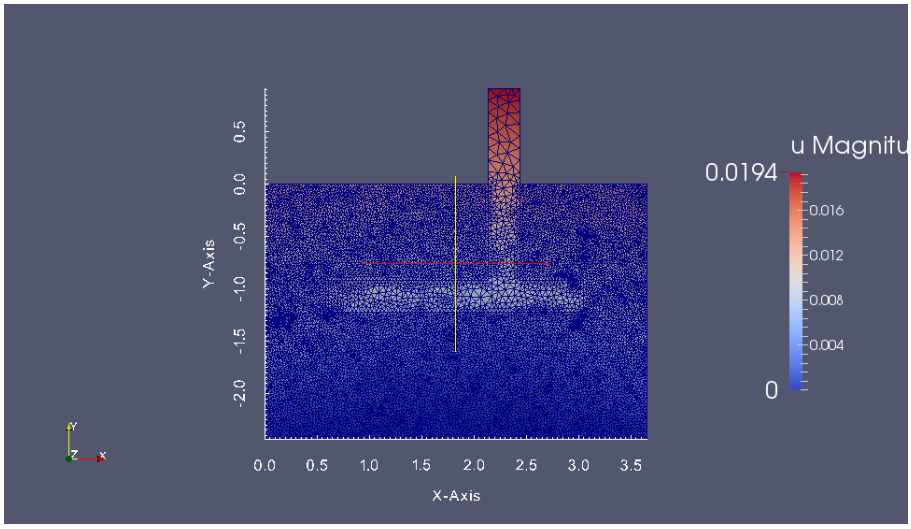

Figure 3.20: Deformation at t=20.0s: m

From the output, we observe the deformation first appears on the top part of the floodwall. When $t = 2.5s$, 3.13 shows deformation on the floodwall heel and toe, though the largest deformation still happens on the floodwall top. We can also find the soil displacement around the floodwall area, since in the model we assume there is no gap or separation between the soil the floodwall. The movement of the floodwall leads to the position change of soil due to the continuity assumption. As time goes by, larger soil deformation is captured, as is the deformation of floodwall. After peak values are reached, displacement for both regions starts to decrease, as seen at $t = 5.0s$ in Figure 3.14. When $t = 7.5s$ in Figure 3.15, it is observed that deformation is becoming larger, until it nearly reaches the max values at $t = 10.0s$ in Figure 3.16. This process repeats over time while external forces from flow continue.

3.4.2 Plastic Model for the Soil

As described in Section 3.1.1, the soil type in Galveston area is mostly silty sand. From lab experiments, we observe the plastic property for most soil types. Significant inelasticity under load is captured for soils, especially clays. The causes of plasticity are various, depending on the composition and the microstructure of the soil. For most soil types, the main cause is the motion and reorganization of neighboring clusters [45, 48]. In the following section, we will first introduce the plasticity theory and models, followed by numerical experiments with simulated external traction forces.

3.4.3 Theory of Plasticity

Assume the plastic body domain is $\Omega \in R^d$. The boundary of Ω is $\partial\Omega$. Considered the Dirichlet and Neumann boundary conditions, the boundary $\partial\Omega$ can be decomposed as:

$$\partial\Omega = \Gamma_u \cup \Gamma_t, \tag{3.34}$$

$$\Gamma_u \cap \Gamma_t = \Phi. \tag{3.35}$$

On Γ_u the displacement $u = \bar{u}(x)$, and on Γ_t the traction $\bar{t}(x)$ is given.

In plasticity theory, an important concept is the yield surface. It is a five-dimensional space inside the six-dimensional stress space [50, 64]. The state of stress inside the surface is the elastic state. When a stress state falls on the surface, it means that the material reaches the yield point and thus becomes plastic [64]. Deformation caused by plasticity makes the stress state to remain on the yield surface [50, 64]. The yield function is defined to describe the yield surface mathematically. The yield function Y is usually expressed as [49]:

$$Y : \mathbf{L} \times R \to R, \tag{3.36}$$

where $\mathbf{L}$ is the tensor space and R is the scalar function space. The parameters are $(\sigma, \nu) \in \mathbf{L} \times R$, where σ is the Cauchy stress tensor and ν is a hardening parameter. The permissible stress space for elastic state is defined as [49, 50, 64]:

$$E^e := \{(\sigma, \nu) \in \mathbf{L} \times R | Y(\sigma, \nu) < 0\}. \tag{3.37}$$

The yield surface, as well as the stress space for the plastic state is defined as:

$$E^p := \{(\sigma, \nu) \in \mathbf{L} \times R | Y(\sigma, \nu) = 0\}. \tag{3.38}$$

The admissible stress space for elastic and plastic states is the union of the two spaces:

$$E := \{(\sigma, \nu) \in \mathbf{L} \times R | Y(\sigma, \nu) \leqslant 0\} = E^e \cup E^p. \tag{3.39}$$

Next we will introduce the flow plasticity theory, in which a flow rule is assumed to exist and determine the material deformation [64]. In flow plasticity theory, the total strain is decomposed as the sum of elastic stain and plastic strain [50, 64]. Elastic strain can be determined from the elastic constitutive model. The plastic strain is dependent on the flow rule and the hardening model.

In flow plasticity theory [64], within the elastic limit deformation is caused only by linear elasticity. When the stress reaches $\sigma = \sigma_0$, plastic deformation first occurs. σ_0 is the stress at initial yield. For strain hardening materials, the deformation continues to increase as the yield stress increases, but not linearly. The increment of stress is defined as $d\sigma$. If $d\sigma > 0$, we call it the loading state. If $d\sigma < 0$, it is called unloading. In loading and $\sigma > \sigma_0$, the increment of plastic strain will always be positive. In unloading, the material is elastic, and the increment of plastic strain will be zero.

In the flow rule [50, 64], it is assumed that the increment of plastic strain and the normal to the yield surface are colinear:

$$d\varepsilon_p = d\lambda \frac{\partial F}{\partial \sigma} \tag{3.40}$$

where $d\lambda$ is called the hardening coefficient, and F is the flow function, also known as the plastic potential. The hardening parameter is a nonnegative scalar. In Drucker's stability postulate [46, 64], the increment of stress and plastic strain must satisfy:

$$d\sigma : d\varepsilon_p \geq 0. \tag{3.41}$$

When $d\sigma : d\varepsilon_p = 0$, it means the pure elastic state.

To build up the system, let us start from the very basic equation of motion from Newton's second law:

$$\nabla \cdot \sigma + f = 0. \tag{3.42}$$

The kinematic relation is

$$\varepsilon = \frac{1}{2}(\nabla u + (\nabla u)^T). \tag{3.43}$$

From the flow theory, the total strain is decomposed as:

$$\varepsilon(u) = \varepsilon^e(u) + \varepsilon^p(u). \tag{3.44}$$

The elastic constitutive rule yields:

$$\sigma(u) = D\varepsilon^e(u) = D(\varepsilon(u) - \varepsilon^p(u)) \tag{3.45}$$

where D is the fourth order elasticity tensor. D satisfies the following properties [49]:

$$D_{ijkl} = D_{jikl} = D_{ijlk} = D_{klij}, \tag{3.46}$$

$$D\varepsilon > 0, \forall |\varepsilon| \neq 0, \tag{3.47}$$

$$D\varepsilon > \alpha|\varepsilon|^2, \text{for some } \alpha > 0. \tag{3.48}$$

ε is the strain tensor. Equation(3.40) gives the evolutionary plastic strain model by [49]

$$\dot{\varepsilon^p}(u) = \dot{\gamma}(\sigma(u), \nu(\varepsilon^p(u)))\frac{\partial F(\sigma(u), \nu(\varepsilon^p(u))}{\partial \sigma(u)}, \forall(\sigma, \nu) \in E^p \tag{3.49}$$

where F is the flow function and ν is the hardening coefficient. $\dot{\gamma}$ is a scalar function and $\dot{\gamma} \geq 0$. To be more precise [64],

$$\dot{\gamma} = 0, \forall(\sigma, \nu) \in E^e \tag{3.50}$$

$$\dot{\gamma} > 0, \forall(\sigma, \nu) \in E^p \tag{3.51}$$

Recall that the yield function Y determines the elastic and plastic states by:

$$Y(\sigma(u), \nu(\varepsilon^p(u))) < 0, \forall(\sigma, \nu) \in E^e \tag{3.52}$$

$$Y(\sigma(u), \nu(\varepsilon^p(u))) = 0, \forall(\sigma, \nu) \in E^p \tag{3.53}$$

In plastic state, it is trivial that

$$\dot{Y}(\sigma, \nu) = 0, \forall(\sigma, \nu) \in E^p. \tag{3.54}$$

which is also called the consistency condition.

So far the unknowns are the displacement u, strain tensor ε, plastic strain tensor ε^p and the stress tensor σ. The boundary conditions are:

$$u = u_0, \text{on}\Gamma_u, \tag{3.55}$$

$$\sigma \cdot n = t, \text{on}\Gamma_t. \tag{3.56}$$

The uniqueness and stability for plasticity solution was discussed in [65].

3.4.4 Plastic Models

In reality, many materials show hardening effect with plastic strain, which means the yield stress increase results in the increase in displacement after the elastic limit is reached. There are two types of hardening: isotropic hardening and kinematic hardening [48, 49, 64]. As indicated from the name, in isotropic hardening the yield surface expands homogeneously. In kinematic hardening the expansion is more complicated. The hardening parameter ν is included in the yield function $Y(\sigma, \nu)$ to describe the hardening effect.

Recall the definitions of yield function Y and the hardening coefficient $\dot{\gamma}$ and it is natural to conclude:

$$\dot{\gamma}Y(\sigma,\nu)=0,\forall(\sigma,\nu)\in E. \tag{3.57}$$

This is known as the Karush-Kuhn-Tucker condition. It is a first order necessary condition for solving nonlinear optimal problems. Furthermore, the following consistency condition can be simply derived from Equation(3.54):

$$\dot{\gamma}\dot{Y}(\sigma,\nu)=0,\forall(\sigma,\nu)\in E. \tag{3.58}$$

In summary, the signs of yield function Y and the hardening coefficient increment indicate the state of a specific material point as [49]:

$$Y<0,\dot{\gamma} = 0, \text{ elastic state} \tag{3.59}$$

$$Y=0,\dot{Y}<0,\dot{\gamma} = 0, \text{ plastic state, elastic unloading} \tag{3.60}$$

$$Y=0,\dot{Y}=0,\dot{\gamma} = 0, \text{ plastic state, neutral loading} \tag{3.61}$$

$$Y=0,\dot{Y}=0,\dot{\gamma} > 0, \text{ plastic state, plastic loading} \tag{3.62}$$

There are multiple choices for the flow function F. When $F=Y$, we call it the associated plasticity model. If $F\neq Y$, it is the non-associated plasticity model. It is more complicated in computation to solve the non-associated plasticity model than the associated plasticity model. No matter what model is used, there is one rule that must not be violated [49]. This rule requires that the yield and flow functions do not change under rotation of coordinate systems. It indicates that the yield and flow functions are in the forms of invariants of stress and strain [49, 64].

The invariants of σ is defined as

$$I_1 = tr(\sigma), \tag{3.63}$$

$$I_2 = \sigma : \sigma, \tag{3.64}$$

$$I_3 = det(\sigma). \tag{3.65}$$

The stress tensor σ can be decomposed into two parts. The first part is the isotropic component which is the mean stress. This part devotes to the deformation mechanism. The remaining part is the deviatoric stress which causes the body distortion [50]. The deviatoric stress S is expressed as:

$$S = \sigma - \frac{1}{3} I_1 I. \tag{3.66}$$

For the deviatoric stress S, the invariants are:

$$J_1 = 0, \tag{3.67}$$

$$J_2 = \frac{1}{2} S : S, \tag{3.68}$$

$$J_3 = det(S). \tag{3.69}$$

There are multiple models of the yield function. In Tresca model [64], the yield function is in the form of

$$Y = max(\frac{1}{2}|\sigma_1 - \sigma_2|, \frac{1}{2}|\sigma_1 - \sigma_3|, \frac{1}{2}|\sigma_2 - \sigma_3|) - \sigma_0. \tag{3.70}$$

σ_0 can be either a constant or a function of I_1. In this model, when the maximum value is reached, yielding starts to occur. Based on the Tresca model, von Mises [64] proposed an advanced model in which the yield function is smooth:

$$Y = \sqrt{J_2} - \sigma_0. \tag{3.71}$$

Tresca and von Mises models indicate that the yielding of materials is independent of hydrostatic pressure [49]. This is true for metal plasticity, but may not be applicable to soil or rocks. The Drucker-Prager model [63] was proposed to overcome this issue. In Drucker-Prager model, an extra mean stress term is added to von Mises's model:

$$Y = \sqrt{J_2} - \alpha_Y I_1 - \sigma_Y. \tag{3.72}$$

The associated flow function is

$$F = \sqrt{J_2} - \alpha_F I_1 - \sigma_F \tag{3.73}$$

where

$$\alpha_Y = -\frac{2sin\phi_1}{\sqrt{3}(3 - sin\phi_1)} \tag{3.74}$$

$$\sigma_Y = \frac{6c \cdot cos\phi_1}{\sqrt{3}(3 - sin\phi_1)} \tag{3.75}$$

$$\alpha_F = -\frac{2sin\phi_2}{\sqrt{3}(3 - sin\phi_2)} \tag{3.76}$$

$$\sigma_F = \frac{6c \cdot cos\phi_2}{\sqrt{3}(3 - sin\phi_2)}. \tag{3.77}$$

ϕ_1 and ϕ_2 are friction angles determined by the material. c is cohension.

3.4.5 Solve for the System

Next, we discuss how to simplify the system before numerical discretization [49]. From(3.53), we obtain

$$\dot{Y} = \frac{\partial Y}{\partial \sigma} : d\sigma + \frac{\partial Y}{\partial \nu}\frac{\partial \nu}{\partial \varepsilon^p} : d\varepsilon^p = 0, \forall(\sigma, \nu) \in E^p. \tag{3.78}$$

Here the colon operator is the inner product between two tensors. By plugging (3.49) into (3.78), the following equation holds:

$$\frac{\partial Y}{\partial \sigma} : d\sigma = -\dot{\gamma}\frac{\partial Y}{\partial \nu}\frac{\partial \nu}{\partial \varepsilon^p} : \frac{\partial F}{\partial \sigma}. \tag{3.79}$$

We take the time differentiated form of (3.44) to get

$$\dot{\varepsilon}(u) = \dot{\varepsilon^e}(u) + \dot{\varepsilon^p}(u) \tag{3.80}$$

By introducing (3.45) and (3.49) to the evolutionary (3.80) we obtain:

$$\dot{\varepsilon} = \dot{\varepsilon}^e + \dot{\varepsilon}^p = D^{-1}d\sigma + \dot{\gamma}\frac{\partial F}{\partial \sigma}. \tag{3.81}$$

We multiply the elasticity tensor D to (3.81) and take the inner product to get

$$\frac{\partial Y}{\partial \sigma} : D\dot{\varepsilon} = \frac{\partial Y}{\partial \sigma} : d\sigma + \dot{\gamma}\frac{\partial Y}{\partial \sigma} : D\frac{\partial F}{\partial \sigma} \tag{3.82}$$

By introducing (3.79) to (3.82), the consistency parameter $\dot{\gamma}$ is derived as

$$\dot{\gamma} = \frac{\dfrac{\partial Y}{\partial \sigma} : D\dot{\varepsilon}}{\dfrac{\partial Y}{\partial \sigma} : D\dfrac{\partial F}{\partial \sigma} - \dfrac{\partial Y}{\partial \nu}\dfrac{\partial \nu}{\partial \varepsilon^p} : \dfrac{\partial F}{\partial \sigma}} \tag{3.83}$$

From (3.81) we can get

$$D\dot{\varepsilon} = \dot{\sigma} + \dot{\gamma}D\frac{\partial F}{\partial \sigma} \tag{3.84}$$

Therefore, the relation between $\dot{\sigma}$ and $\dot{\varepsilon}$ is simplified as

$$\dot{\sigma} = D^{ep}\dot{\varepsilon}, \forall(\sigma, \nu) \in E. \tag{3.85}$$

D^{ep} is the equivalent tensor defined as

$$D^{ep} = \begin{cases} D\,, & \forall(\sigma,\nu) \in E^e \\ D - \dfrac{D\dfrac{\partial F}{\partial \sigma} \otimes D\dfrac{\partial Y}{\partial \sigma}}{\dfrac{\partial Y}{\partial \sigma} : D\dfrac{\partial F}{\partial \sigma} - \dfrac{\partial Y}{\partial \nu}\dfrac{\partial \nu}{\partial \varepsilon^p} : \dfrac{\partial F}{\partial \sigma}}\,, & \forall(\sigma,\nu) \in E^p \end{cases} \tag{3.86}$$

Here $\otimes$ is the tensor product operator. When we choose the associated model where $F = Y$, for plastic state D^{ep} will be a symmetric operator, while in the nonassociated model D^{ep} will be nonsymmetric. The coupled system from Equation(3.42) to (3.49) is simplified as

$$\nabla \cdot \sigma + f = 0 \tag{3.87}$$

$$\varepsilon = \frac{1}{2}(\nabla u + (\nabla u)^T) \tag{3.88}$$

$$\dot{\sigma} = D^{ep}\dot{\varepsilon} \tag{3.89}$$

When solving the system, we typically solve for the time derivative displacement $\dot{u}$, $\dot{\varepsilon}$ and $\dot{\sigma}$ from the evolutionary equations:

$$\nabla \cdot \dot{\sigma} + \dot{f} = 0 \tag{3.90}$$

$$\dot{\varepsilon} = \frac{1}{2}(\nabla \dot{u} + (\nabla \dot{u})^T) \tag{3.91}$$

$$\dot{\sigma} = D^{ep}\dot{\varepsilon} \tag{3.92}$$

3.4.6 Numerical Methods

We start from the momentum equation in the time derivative form

$$\nabla \cdot \dot{\sigma} + \dot{f} = 0. \tag{3.93}$$

By multiplying the test function $\dot{v} \in V$ and integrating by parts, we get the form

$$\int_{\Omega} \dot{\sigma} : \nabla \dot{v} dV - \int_{\partial\Omega} (\dot{\sigma}(u)n) \cdot \dot{v} dS = \int_{\Omega} \dot{f} \cdot \dot{v} dV \tag{3.94}$$

Now we have

$$a(\dot{u}, \dot{v}) = \int_{\Omega} D^{ep}(\sigma) B\dot{u} : \nabla(\dot{v}) dV \tag{3.95}$$

and

$$L(\dot{v}) = \int_{\Omega} \dot{f} \cdot \dot{v} dV + \int_{\Gamma t} \dot{\bar{t}} \cdot \dot{v} dS \tag{3.96}$$

where $\sigma \cdot n = t$, on Γ_t. The variational form is to find $\dot{u} \in V$ such that

$$a(\dot{u}, \dot{v}) = L(\dot{v}), \forall \dot{v} \in V. \tag{3.97}$$

In discretization, $\dot{\sigma}$, $\dot{\varepsilon}$, $\dot{u}$ and $\dot{v}$ are replaced with the incremental quantities $\delta\sigma$, $\delta\varepsilon$, δu and δv in the variational form:

$$a(\delta u, \delta v) = \int_{\Omega} D^{ep}(\sigma) B\delta u : \nabla(\delta v) dV \tag{3.98}$$

and

$$L(\delta v) = \int_{E} \delta f \cdot \delta v dV + \int_{\Gamma t} \delta \ \hat{t} \cdot \delta v dS \tag{3.99}$$

Equation (3.85) is rewritten as

$$\delta\sigma = D^{ep}\delta\varepsilon \tag{3.100}$$

In the following analysis, we will use Voigt notation to represent the symmetric tensors [51]. The benefit of Voigt notation is to decrease the computation complexity by reducing the tensor order. For example, in 2D case, the full strain

tensor ε, plastic strain ε^p, total stress σ, symmetric gradient $\nabla^s u$ are

$$\varepsilon = \begin{pmatrix} \varepsilon_{11} & \varepsilon_{12} \\ \varepsilon_{21} & \varepsilon_{22} \end{pmatrix}, \qquad \varepsilon^p = \begin{pmatrix} \varepsilon^p_{11} & \varepsilon^p_{12} \\ \varepsilon^p_{21} & \varepsilon^p_{22}. \end{pmatrix}$$

$$\sigma = \begin{pmatrix} \sigma_{11} & \sigma_{12} \\ \sigma_{21} & \sigma_{22}. \end{pmatrix}, \qquad \nabla^s u = \begin{pmatrix} u_{1,1} & \dfrac{u_{1,2}+u_{2,1}}{2} \\ \dfrac{u_{1,2}+u_{2,1}}{2} & u_{2,2}. \end{pmatrix}$$

In Voigt notation, ε, ε^p, σ, $\nabla^s u$ are rewritten as

$$\varepsilon = \begin{pmatrix} \varepsilon_{11} \\ \varepsilon_{21} \\ 2\varepsilon_{12} \end{pmatrix}, \qquad \varepsilon^p = \begin{pmatrix} \varepsilon^p_{11} \\ \varepsilon^p_{22} \\ 2\varepsilon^p_{21} \end{pmatrix},$$

$$\sigma = \begin{pmatrix} \sigma_{11} \\ \sigma_{22} \\ \sigma_{12} \end{pmatrix}, \qquad \nabla^s u = \begin{pmatrix} u_{1,1} \\ u_{2,2} \\ u_{1,2}+u_{2,1} \end{pmatrix}.$$

The symmetric fourth order D is represented as

$$D = \begin{pmatrix} D_{1111} & D_{1122} & D_{1112} \\ D_{1122} & D_{2222} & D_{2212} \\ D_{1112} & D_{2212} & D_{1212} \end{pmatrix}$$

In linear elasticity, D is represented as [60]

$$D = \lambda \mathbf{1} \otimes \mathbf{1} + 2\mu \mathbf{I}, \tag{3.101}$$

where $\mathbf{1}$ is the second-order symmetric unit tensor, $\mathbf{I}$ is the fourth-order symmetric unit tensor, λ and μ are Lamé parameters. Originally D has 16 components. Under Voigt notation D is reduced to

$$D = \begin{pmatrix} \lambda + 2\mu & \lambda & 0 \\ \lambda & \lambda + 2\mu & 0 \\ 0 & 0 & \mu \end{pmatrix}$$

The relation between total strain ε and deformation u can be reformulated as

$$\varepsilon = Bu \tag{3.102}$$

Under the Voigt nonation, B is represented as:

$$B = \begin{pmatrix} \partial/\partial x & 0 \\ 0 & \partial/\partial y \\ \partial/\partial x & \partial/\partial y \end{pmatrix}$$

The relation between σ and u is

$$\sigma = D\varepsilon = DBu \tag{3.103}$$

Again, $\dot{\sigma}$, $\dot{\varepsilon}$, $\dot{u}$ and $\dot{v}$ in (3.102) and (3.103) are replaced with $\delta\sigma$, $\delta\varepsilon$, δu and δv to obtain the general form:

$$\delta\varepsilon = B\delta u \tag{3.104}$$

$$\delta\sigma = D^{ep}B\delta u. \tag{3.105}$$

From the variational form (3.98) and (3.99), δu can be solved. $\delta\varepsilon$ and $\delta\sigma$ are updated based on Equation (3.105) and Equation (3.105).

Now let us go back to the variational form (3.98) and look into the system again. We would like to discuss the existence and the uniqueness of the solutions to the plastic model. The key component in the variation form is the complicated tensor D^{ep}. If D^{ep} is bounded by some positive constant C, we will have

$$a(\delta u, \delta v) = \int_\Omega D^{ep}(\sigma) B\delta u : \nabla(\delta v) dV \leqslant CA \parallel \delta u \parallel_{H^1} \parallel \delta v \parallel_{H^1} \tag{3.106}$$

given B is the differentiating operator and naturally bounded by some positive constants A. If the above inequality holds, there exists solution δu to the variation form (3.98). Now let us examine if D^{ep} is bounded by any positive constant. From (3.86), D^{ep} consists of two parts. D is a constant tensor only determined by Lame's constants λ and μ. So we only need to consider the remainder. In the yield function Y chosen in the Drager Prager's model, Y does not depend on ν or ε^p, so D^{ep} is simplified as

$$D^{ep} = D - \frac{D\dfrac{\partial F}{\partial \sigma} \otimes D\dfrac{\partial Y}{\partial \sigma}}{\dfrac{\partial Y}{\partial \sigma} : D\dfrac{\partial F}{\partial \sigma}} \tag{3.107}$$

We know for any second order tensor X and ϕ, the following equation holds:

$$(X \otimes X)\phi = (X \cdot \phi)X. \tag{3.108}$$

Assume the maximum and minimum eigenvalues of D are λ_{max} and λ_{min} respectively. Therefore,

$$\lambda_{min} \parallel \frac{\partial F}{\partial \sigma} \parallel \leqslant \parallel D\frac{\partial F}{\partial \sigma} \parallel \leqslant \lambda_{max} \parallel \frac{\partial F}{\partial \sigma} \parallel \tag{3.109}$$

,

$$\lambda_{min} \parallel \frac{\partial Y}{\partial \sigma} \parallel \leqslant \parallel D\frac{\partial Y}{\partial \sigma} \parallel \leqslant \lambda_{max} \parallel \frac{\partial Y}{\partial \sigma} \parallel \tag{3.110}$$

and

$$\parallel D\frac{\partial F}{\partial \sigma} \otimes D\frac{\partial Y}{\partial \sigma} \parallel \leqslant \lambda_{max}^2 \parallel \frac{\partial F}{\partial \sigma} \parallel \parallel \frac{\partial Y}{\partial \sigma} \parallel . \tag{3.111}$$

In the associate model, $Y = F$, so that $\forall \phi$,

$$\parallel \frac{D\frac{\partial F}{\partial \sigma} \otimes D\frac{\partial Y}{\partial \sigma}\phi}{\frac{\partial Y}{\partial \sigma} : D\frac{\partial F}{\partial \sigma}} \parallel \leqslant \frac{\lambda_{max}^2 \parallel \frac{\partial F}{\partial \sigma} \parallel^2 \parallel \phi \parallel}{\lambda_{min} \parallel \frac{\partial F}{\partial \sigma} \parallel^2} = \frac{\lambda_{max}^2}{\lambda_{min}} \parallel \phi \parallel . \tag{3.112}$$

This means

$$\parallel \frac{D\frac{\partial F}{\partial \sigma} \otimes D\frac{\partial Y}{\partial \sigma}}{\frac{\partial Y}{\partial \sigma} : D\frac{\partial F}{\partial \sigma}} \parallel \leqslant \frac{\lambda_{max}^2}{\lambda_{min}} \tag{3.113}$$

Therefore, D is a bounded operator, and the existence of solution δu is proved.

$$a(\delta u, \delta u) = \int_\Omega DB(\delta u) : \nabla(\delta u) - \int_\Omega \frac{D\frac{\partial F}{\partial \sigma} \otimes D\frac{\partial Y}{\partial \sigma}}{\frac{\partial Y}{\partial \sigma} : D\frac{\partial F}{\partial \sigma}} B(\delta u) : \nabla(\delta u) = H_h(\delta u) - \Sigma_h \delta u. \tag{3.114}$$

If $H_h(\delta u) - \Sigma_h \delta u > 0$, $a(\delta u, \delta u) > 0$. The stiffness matrix assembled will be positive definite. This is the sufficient condition for the variational form to have the unique solution, as discussed in [65]. If $H_h(\delta u) - \Sigma_h \delta u \leqslant 0$, the uniqueness of the solution is not guaranteed. This matches with the theoretical stress strain curve. For strictly elastic status, $D^{ep} = D$, only one solution exists, until it reaches the elastic limit. Beyond the elastic limit, the solid will not go back to its original shape or size when the forces are removed. Permanent deformation starts to happen. When unloading

after the elastic limit, the deformation change will not follow the original curve in previous loading period. At yield point, there could be two solutions of displacement corresponding to the same stress. In our model, $\frac{\partial Y}{\partial \nu}\frac{\partial \nu}{\partial \varepsilon^p} = h = 0$. In general, h may not be 0 and h helps to control $\Sigma_h(\delta u)$ such that $H_h(\delta u) - \Sigma_h \delta u > 0$ may hold. More discussions on how h affect the uniqueness of the solutions can be found in [65].

3.4.7 Stress Correction

The stress at current time step is updated by

$$\sigma_{n+1} = \sigma_n + \delta\sigma \tag{3.115}$$

A problem may occur that the updated $(\sigma_{n+1}, \nu_{n+1})$ could be out of the admissible space E, i.e. $Y(\sigma_{n+1}, \nu_{n+1}) > 0$. This problem still exists even when the time steps are decreased since the errors will be accumulated. In order to solve the problem, stress correction algorithms [59] - [62] are mostly used. In this work, Euler forward radial return algorithm is used for correction [59] and [47].

In Euler forward return algorithm, one important assumption is both δu and $\delta\varepsilon$ stay unchanged during the stress correction. From Equation (3.81), we obtain

$$\dot{\sigma} = D\dot{\varepsilon} - \dot{\gamma} D \frac{\partial F}{\partial \sigma} \tag{3.116}$$

From Equation (3.116) $\delta\sigma$ is derived as

$$\delta\sigma = D\sigma\varepsilon - \int_{\gamma_0}^{\gamma_0+\dot{\gamma}} D\frac{\partial F}{\partial \sigma} d\gamma. \tag{3.117}$$

Since

$$\dot{\sigma} = D(\dot{\varepsilon} - \dot{\varepsilon^p}), \tag{3.118}$$

we can decompose $\delta\sigma$ as the sum of elastic part $\delta\sigma^e$ and plastic part $\delta\sigma^p$

$$\delta\sigma = \delta\sigma^e + \delta\sigma^p \tag{3.119}$$

where

$$\delta\sigma^e = D\delta\varepsilon \tag{3.120}$$

and

$$\delta\sigma^p = \dot{\gamma} D \frac{\partial F}{\partial \sigma}. \tag{3.121}$$

The integration can be viewed as integrating along a flow path PQ. From the initial point P, $\delta\sigma^e$ may project the current status outside the yield surface. The plastic devotion can be approximated as

$$\delta\sigma^p = \dot{\gamma} D (\frac{\partial F}{\partial \sigma})_Q. \tag{3.122}$$

Q may fall out of the admissible space, so a correction is necessary. Point Q is corrected to Point T on the yield surface by

$$\sigma_T = \sigma_Q - \dot{\gamma} D (\frac{\partial F}{\partial \sigma})_Q. \tag{3.123}$$

Point T satisfies

$$Y(\sigma_T) = Y(\sigma_Q - \dot{\gamma} D (\frac{\partial F}{\partial \sigma})_Q) = 0. \tag{3.124}$$

From Taylor expansion of (3.124) we have

$$Y(\sigma_Q) - \dot{\gamma} (\frac{\partial Y}{\partial \sigma})_Q : D (\frac{\partial F}{\partial \sigma})_Q = 0 \tag{3.125}$$

So $\dot{\gamma}$ is approximated as

$$\dot{\gamma} = \frac{Y(\sigma_Q)}{(\frac{\partial Y}{\partial \sigma})_Q : D (\frac{\partial F}{\partial \sigma})_Q}. \tag{3.126}$$

The stress σ_{n+1} is updated after correction as

$$\sigma_{n+1} = \sigma_T = D\delta\varepsilon - \dot{\gamma}D(\frac{\partial F}{\partial \sigma})_Q = D\delta\varepsilon - \frac{Y(\sigma_Q)D(\frac{\partial F}{\partial \sigma})_Q}{(\frac{\partial Y}{\partial \sigma})_Q : D(\frac{\partial F}{\partial \sigma})_Q} \tag{3.127}$$

The approximation of σ_T may not ensure T strictly on the yield surface. Approximation in integration and Taylor's expansion both contribute to the error. Therefore, multiple iterations should be involved until the error is below the tolerance. The algorithm is summarized as [49]:

Initialize: σ_0 at a material point P;

for *Iterations:* $j = 1, 2, ..., n$ **do**

Compute $\dot{\gamma} = \dfrac{Y(\sigma_Q^j)}{(\frac{\partial Y}{\partial \sigma})_Q^j : D(\frac{\partial F}{\partial \sigma})_Q^j}$;

$\delta\sigma^p = \dot{\gamma}D(\frac{\partial F}{\partial \sigma})_Q^j$;

$(\sigma^{j+1})_T = (\sigma^j)_Q - \delta\sigma^p$;

Let T replace Q ;

Until $Y(\sigma^{j+1}) < tol$;

end

3.4.8 Global Algorithm

On the global level, Newton's method is used to solve the variational form [49, 62, 64]. The total external load vector F can be decomposed into n small sub-

steps as

$$F_1^E, F_2^E, F_3^E, ...F_n^E \tag{3.128}$$

and the incremental forces are

$$\Delta F_1^E, \Delta F_2^E, \Delta F_3^E, ...\Delta F_n^E. \tag{3.129}$$

ΔQ is denoted as the increment of internal stress by

$$\Delta Q = \int_E B^T \delta\sigma dV - \int_{\partial E} n\delta\sigma dS. \tag{3.130}$$

In theory,

$$\Delta R = \Delta Q - \Delta F^E = 0. \tag{3.131}$$

For each load step, we first initialize the external force ΔF^E and Δu. The inner loop is where we solve for the incremental displacement from the variational form. At the beginning, by checking the sign of yield function $Y(\sigma, \nu)$, we can determine whether the current status is plastic or elastic. D^{eq} will be assigned based on material point status. The stiffness matrix K from the variational form (3.98) and (3.99) is then assembled with residual ΔR computed. In actual computation, the incremental displacement Δu at given time step j is given as the summation of δu at each sub-step:

$$\Delta u_j = \delta u_j^1 + \delta u_j^2 + ... + \delta u_j^m \tag{3.132}$$

Newton's method is applied to solve for each δu_j^k. The increment of displacement Δu, total strain $\Delta\varepsilon$ and stress $\Delta\sigma$ are updated next. Then we check if the current solution (σ, ν) is in the admissible space. Otherwise, the stress correction will be

applied until the error is within tolerance. This process repeats until the last load step. The detailed algorithm to solve the full coupled plastic model is summarized as

[49]:

Initialize: U_0, F_0^E ;

for *time steps:* $j = 1, 2, ..., n$ **do**

Set external force increment ΔF_j^E ;

Initialize ΔU_j^0 ;

if $(Y < 0)$ **then**

$D^{ep} = D$;

end

while $(||\delta R_j^k|| < tol \cdot ||F||_2)$ **do**

Compute stiffness matrix K_j^k ;

Form $\delta R_j^k = \Delta Q_j^k - \Delta F_j^E$;

Solve $K_j^k \delta U_j^k = -\delta R_j^k$;

Update: $\Delta U_j = \Delta U_j + \delta U_j^k$, $\Delta \varepsilon_j = \Delta \varepsilon_j + B \delta U_j^k$;

if $(\sigma_j, \nu_j) \notin E$ **then**

Correction to σ_j until $Y(\sigma_j, \nu_j) < tol$;

end

end

Update $U_j = U_{j-1} + \Delta U_j$, $\varepsilon_j = \varepsilon_{j-1} + \Delta \varepsilon_j$;

end

3.5 Numerical Experiments for Soil-Structure Model

We will test on the same domain as in Section 3.4.1. The plastic model is used to simulate the soil behavior, while for the floodwall part linear elastic model stays unchanged. The total simulation time is $5s$, and time step $\delta t = 0.01s$. In plastic model, we use a smaller time step compared to $\delta t = 0.1s$ in elastic model. This is to reduce the possible accumulated error. Figure 3.21 to Figure 3.31 below show the deformation of the soil-floodwall over time. The synthetic external force applied on the top left side of the floodwall is

$$f_x = 20,000 * sin(20t)N \tag{3.133}$$

$$f_y = 0N. \tag{3.134}$$

The boundary conditions are:

$$\mathbf{u} = \mathbf{0}, \text{on the bottom} \tag{3.135}$$

$$\sigma \cdot \mathbf{n} = \mathbf{f}, \text{on top of floodwall} \tag{3.136}$$

$$\sigma \cdot \mathbf{n} = (0.0, 0.0)^T \text{elsewhere} \tag{3.137}$$

From the output, we observe the deformation first appears on the top part of the floodwall. In Figure 3.22 when $t = 0.5s$, deformation is seen on the floodwall heel and toe. The largest deformation occurs on the floodwall top as expected. We can also see the soil displacement, especially above the floodwall toe. As time goes by, larger soil deformation is captured, so is the deformation of floodwall. After peak values are reached, displacement for both regions starts to decrease, as seen at $t = 1.5s$ in Figure 3.24. When$t = 2.5s$ in Figure 3.26, it is observed that deformation

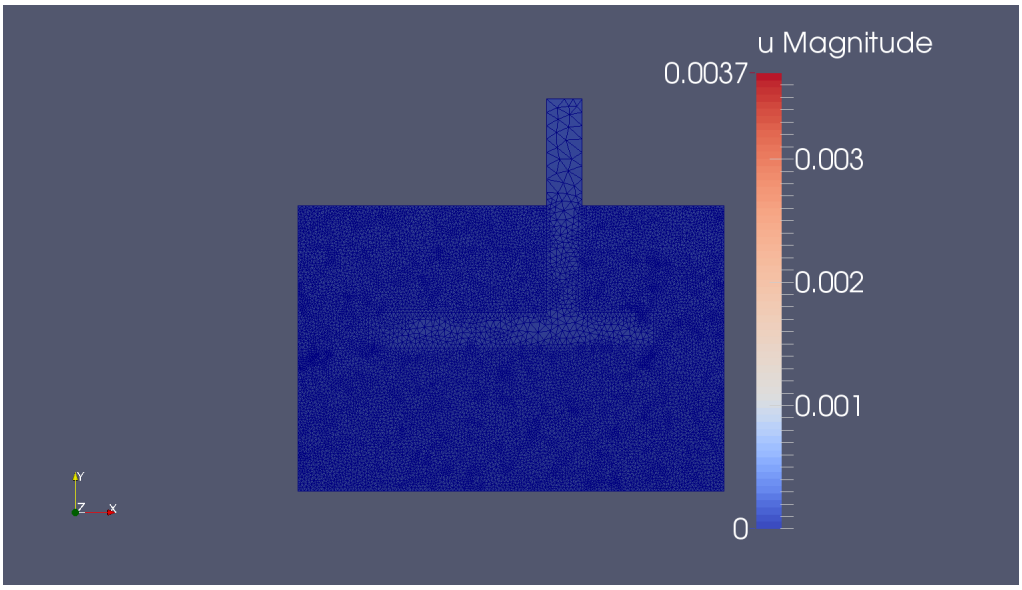

Figure 3.21: Deformation at t=0s: m

is becoming larger again, until it nearly reaches the max values. At $t = 3.0s$ in Figure 3.27, the deformation decreases again. This process repeats over time before the external synthetic force is removed.

In this experiment, the maximum magnitude of the external force is $20,000N$. We vary the maximum values of the external force, and rerun the program. The plot in Figure 3.32 shows the relationship between the maximum force and maximum displacement occurring in the whole simulation. When the external force is relatively small, the relation is almost linear. When the force increases and exceeds $35,000N$, nonlinearity starts to dominate.

Figure 3.33 is the stress strain curve for plasticity. It shows the theoretical relationship between stress and strain. By comparing Figure 3.33 to Figure 3.32, we

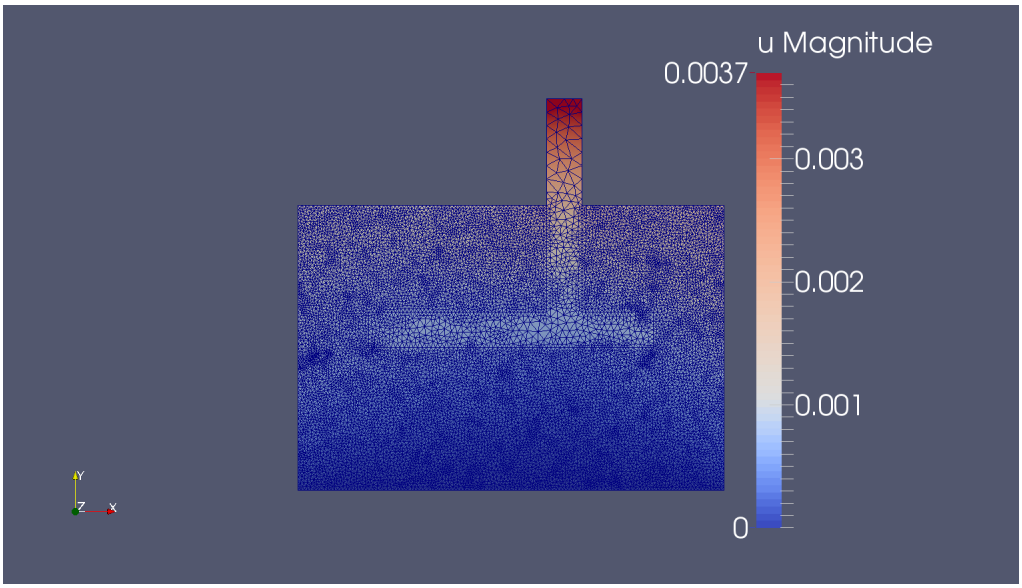

Figure 3.22: Deformation at t=0.5s: m

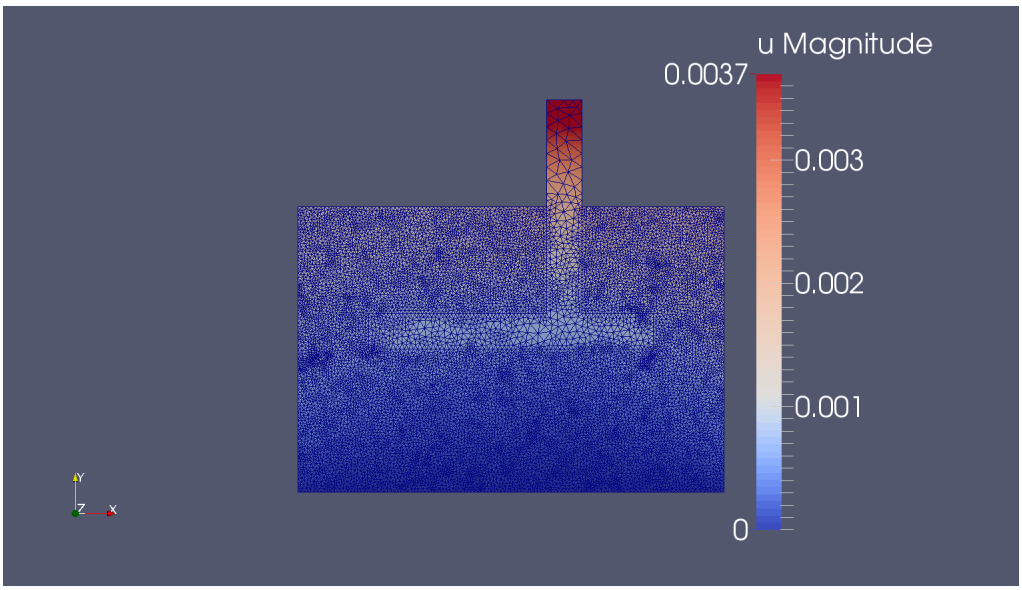

Figure 3.23: Deformation at t=1.0s: m

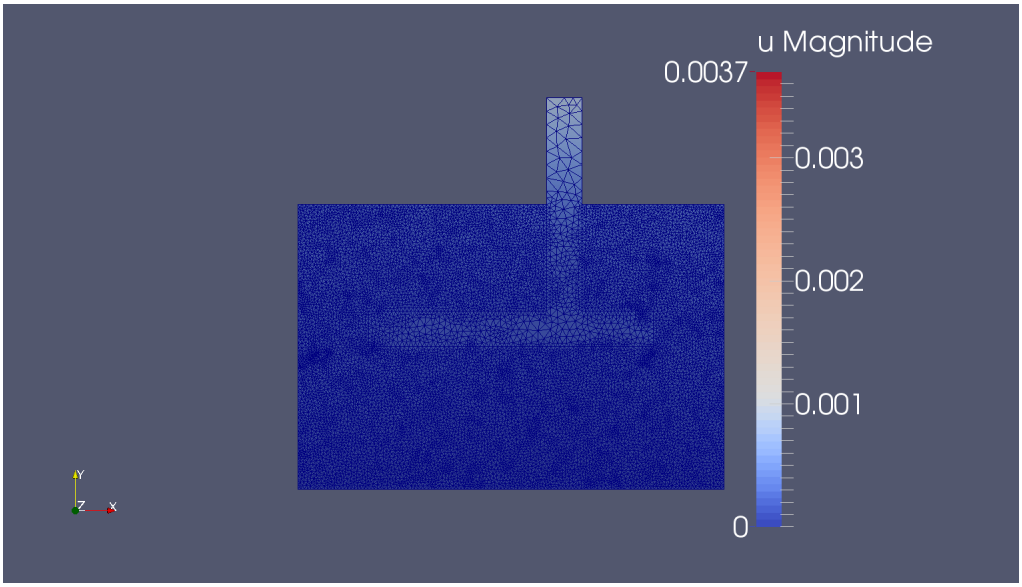

Figure 3.24: Deformation at t=1.5s: m

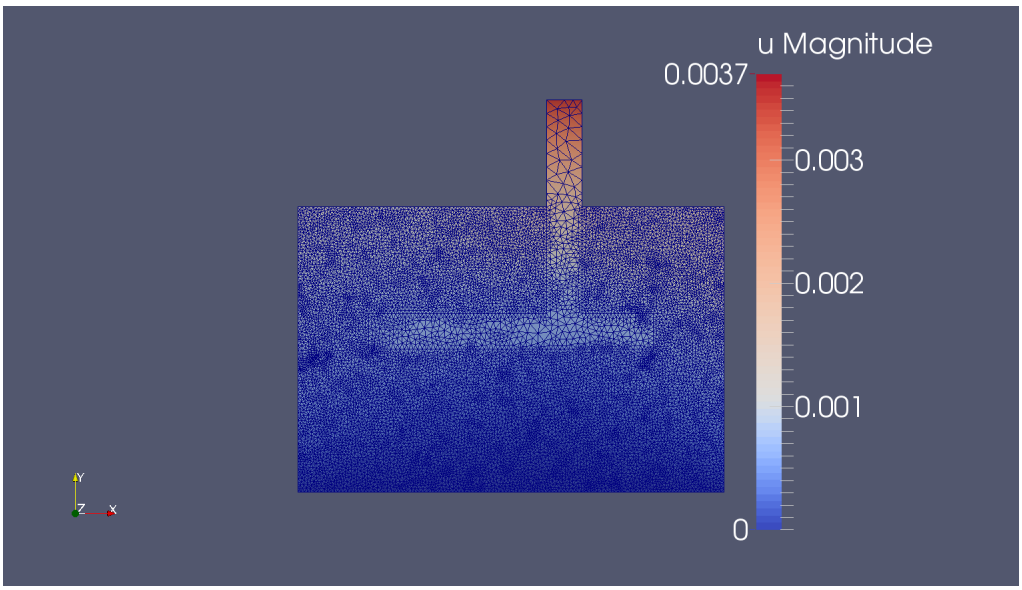

Figure 3.25: Deformation at t=2.0s: m

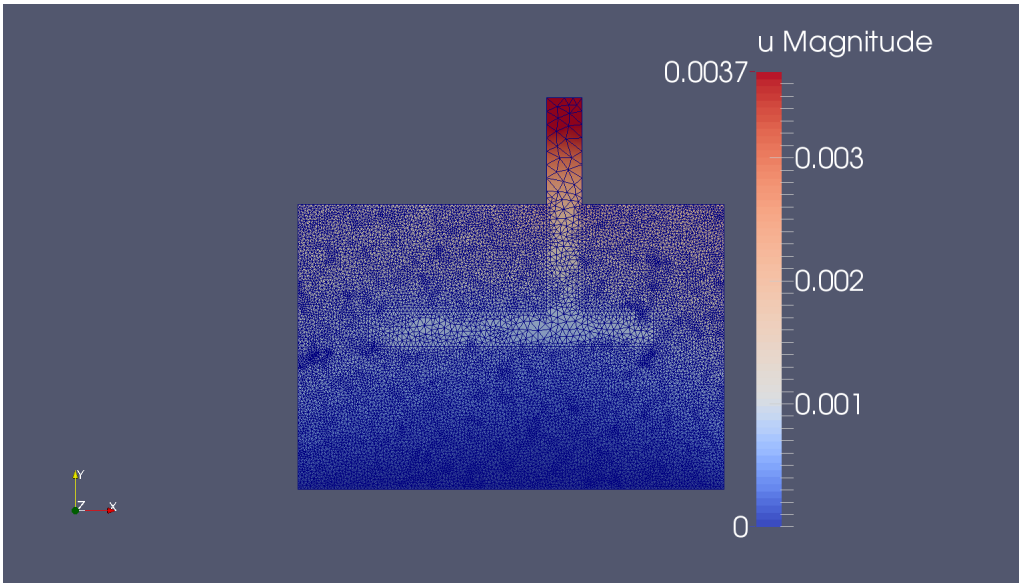

Figure 3.26: Deformation at t=2.5s: m

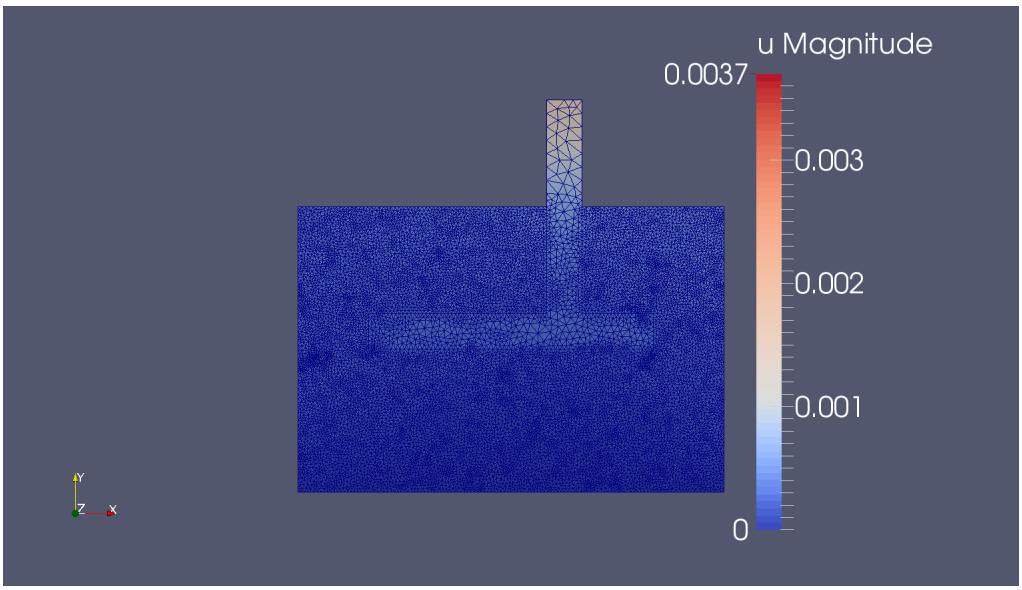

Figure 3.27: Deformation at t=3.0s: m

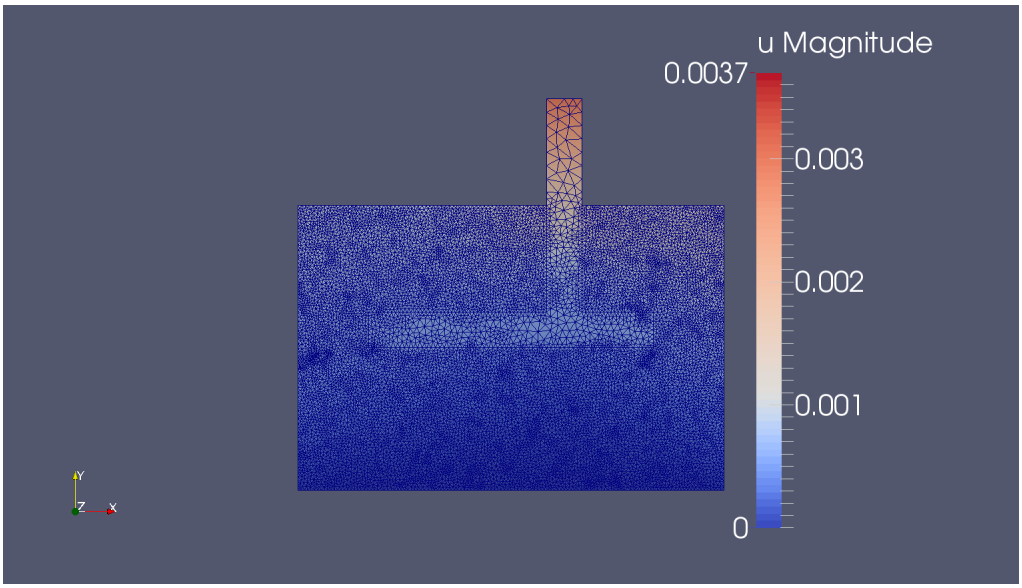

Figure 3.28: Deformation at t=3.5s: m

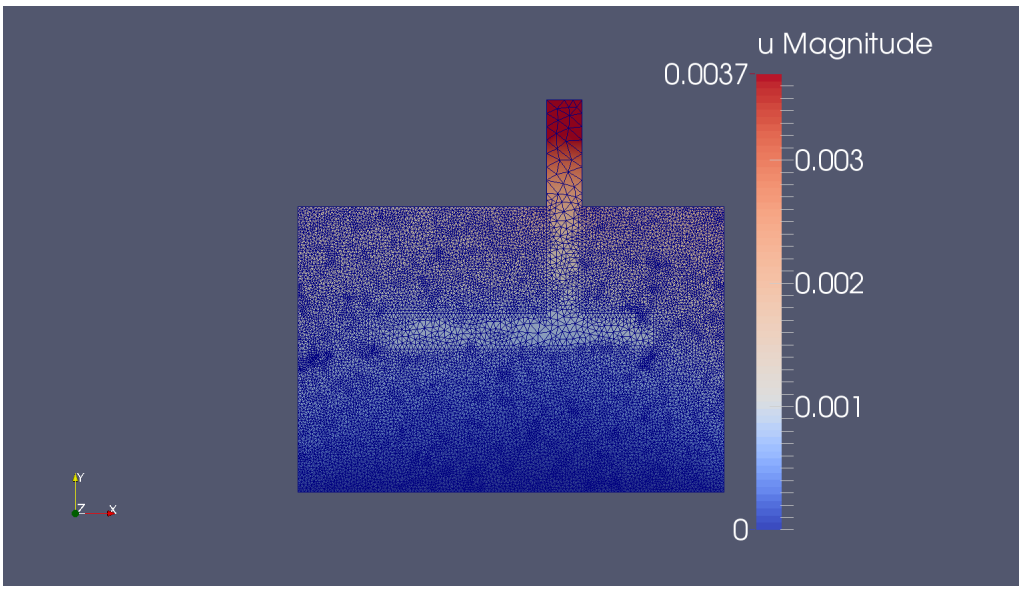

Figure 3.29: Deformation at t=4.0s: m

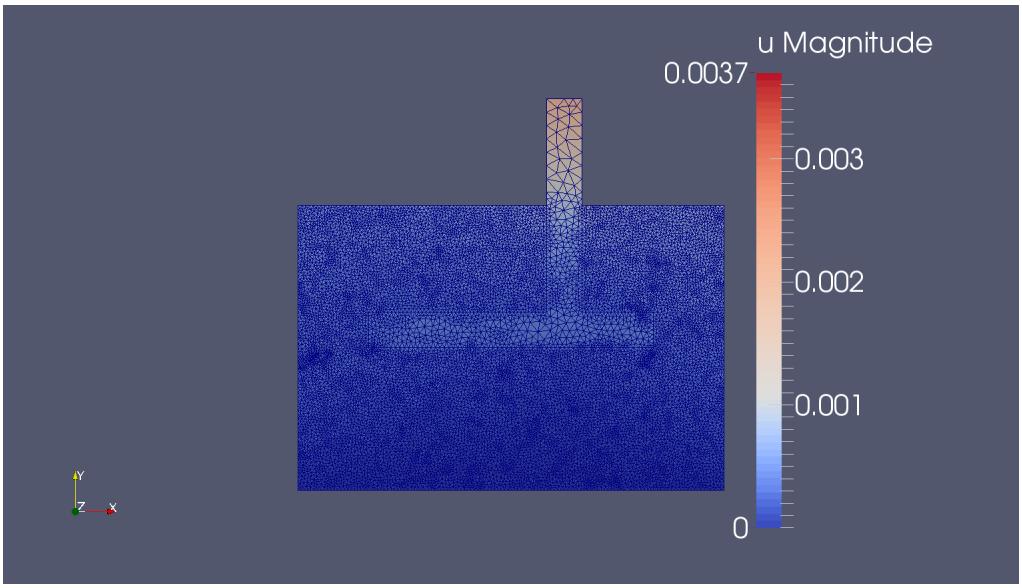

Figure 3.30: Deformation at t=4.5s: m

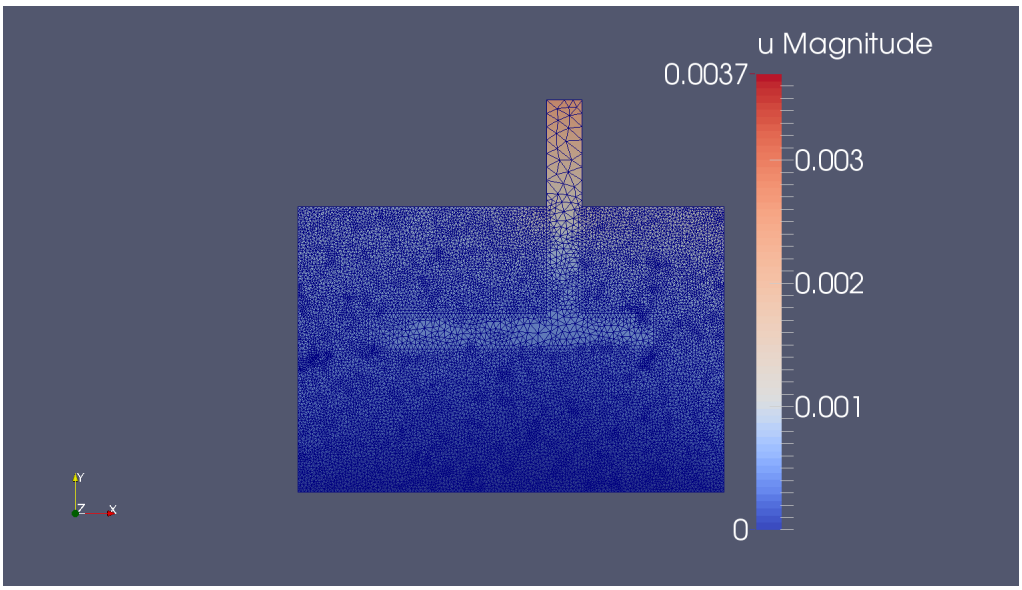

Figure 3.31: Deformation at t=5.0s: m

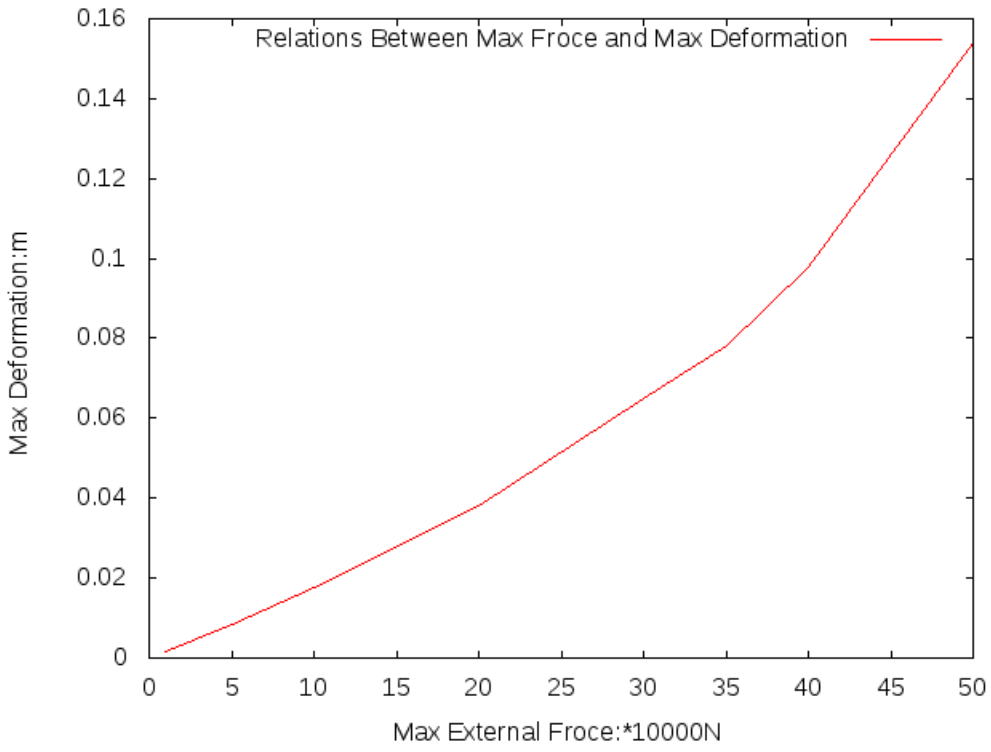

Figure 3.32: Relationship between Max Force and Max Deformation

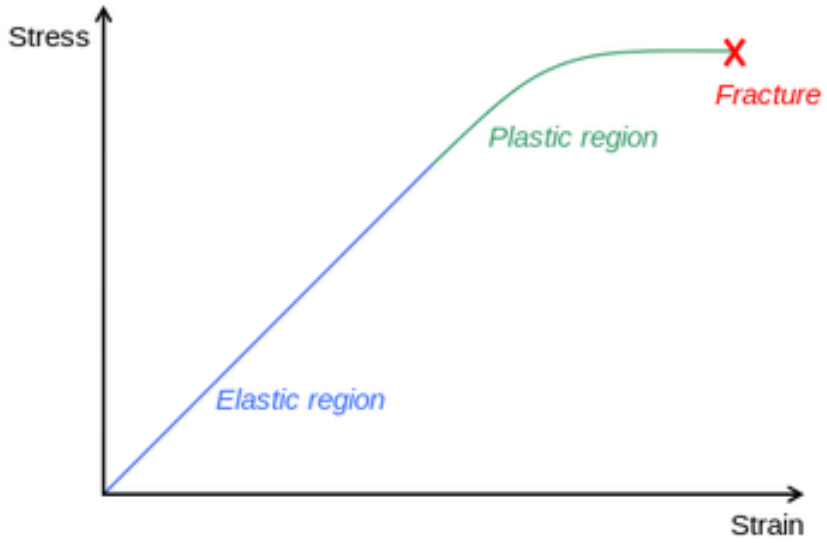

Figure 3.33: Theoretical Stress Strain Curve for Plasticity (Moondoggy [52] 2008)

conclude our numerical experiments indicate the correct trend. For relatively small external forces, yield surface has not been reached. The system is in linear elastic status. When the forces increase to larger values, plasticity starts to occur. That is why the nonlinearity is captured in the latter portion.

We also apply the convergence analysis to the coupled system by decreasing the mesh size. Remember the maximum element diameter in the soil is $h_{es} = 0.1m$, and the maximum element diameter for floodwall is $h_{ef} = 0.025m$. The soil sub mesh is 16 times finer than the floodwall sub mesh. Let the soil sub mesh size decrease from $0.4m$ to $0.025m$. The floodwall sub mesh is refined simultaneously, while the ratio of h_{es} and h_{ef}stays unchanged at 4. It is rather difficult to solve the system for the analytic solutions. Instead, we use the solutions from the finest mesh where $h_{es} = 0.025m$ to be the substitution of the exact solutions. The relative error is

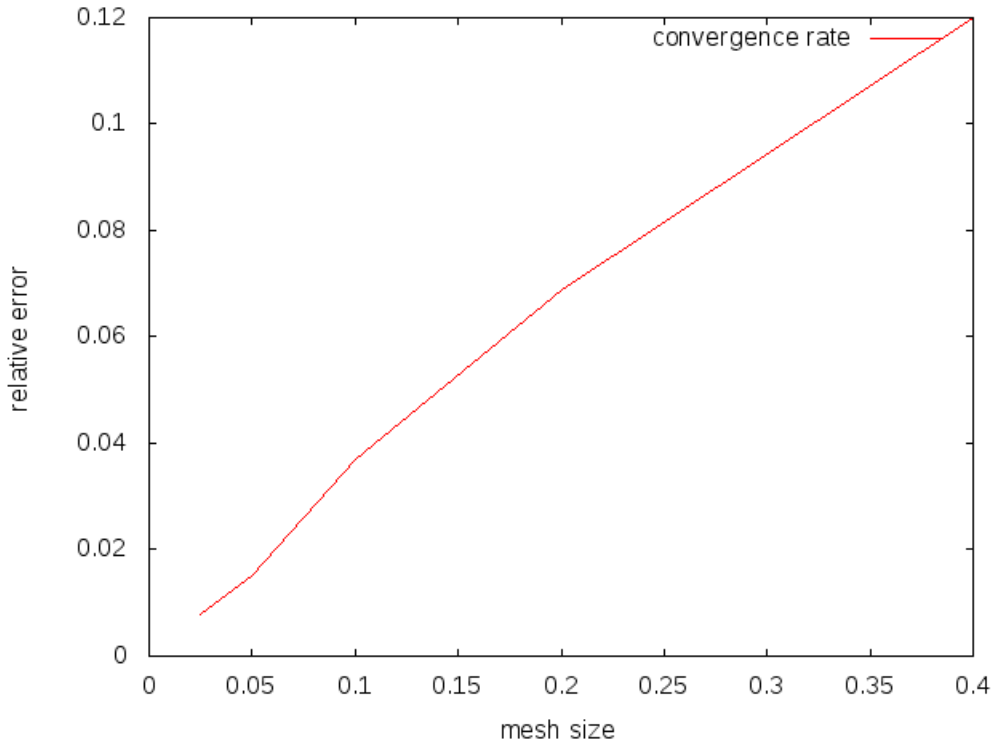

Figure 3.34: Convergence Rate of Soil-Floodwall Plastic-Elastic Model

plotted in Figure 3.34. The convergence rate is almost first order.

Chapter 4

Interaction Process - One Way

4.1 Introduction

In Section 2 and Section 3, we have discussed the individual fluid and structure models. Now let's focus on the interaction simulation which links the two separate processes through the common fluid-structure interface. In many engineering designs, for simplicity one way interaction model is often used. The traction along the interface is extracted from the wave driven air-water system. The traction will then be used as the boundary condition to the structure model. In this model, the influence of structure deformation to the flow is ignored. It is relative simpler in computation. For small structure deformation, the solution is quite reasonable. However, in reality when hurricane occurs with high tides, the structure deformation can be sufficiently large. The lack of accurate estimation of the water-filled gap may lead to levee failure as seen in Hurricane Katrina [28]. The impact of the structure to the flow is important and cannot be neglected.

Two-way interaction model is more complicated both in theory and computation. In most fluid-structure interaction models one of the difficulties is inter-

face movement. Generally there are two types of techniques in moving boundaries and interfaces problems: the interface-tracking methods and the interface-capturing methods. The interface-capturing technique(non-moving-mesh) is preferred when the geometric complexity of the interface requires a fluid mesh that is not affordable in mesh moving [11, 12].

One popular method to capture the interface is the Volume of Fraction method [1], which is defined as:

$$V_e = \frac{1}{vol(\Omega_e)} \int_{\Omega_e} H(\phi) d\Omega \tag{4.1}$$

Ω_e is the mesh element, H is the Heaviside function. By definition of H, it is easy to know the fraction of two materials in each of the elements, which enables us to reconstruct the interface in each cell at current time step.

In the interface-tracking methods, the fluid will occupy the spatial domain where part of the solid used to be, and the shapes of subdomains keep changing over time [18, 19]. The mesh is required to move to adapt to the shape change. This technique enables us to control the mesh resolution near the interface and obtain accurate solutions. In this work, we will use interface-tracking methods to track the fluid structure interface. The arbitrary Lagrangian-Eulerian (ALE) framework [18, 19, 23] will be used for flows on the moving domain. The two-way interaction is simulated by passing and applying the boundary conditions on fluid-structure interface in both directions. In the following discussion, we will start with the one-way simulation. The theory of ALE and the fully coupled two-way interaction model will be introduced in the next section. The numerical experiments and analysis will also be shown.

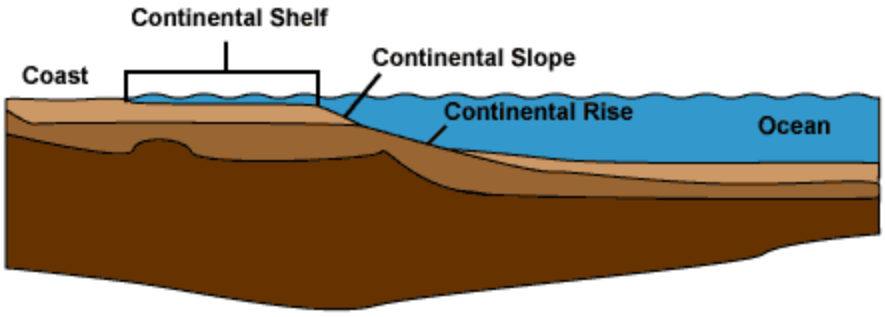

Figure 4.1: Continental Slope (From the Office of Naval Research [54], 2006)

4.2 One-Way Interaction Simulation

In the one way interaction model, the tractions computed from the flow subproblem are saved and used as the boundary conditions in the structure subproblem. It costs less in computation and is used extensively in engineering scenario study and design. To be closer to the actual environment in Galveston Bay, we will make a slight change to the computation domain. Compared with the domain in the test cases from Section 2 and 3, the new domain size is larger with continental slope added.

Continental shelf is the land under the surface of water [53]. It is the extension of continent with shallow water. The endpoint of the continental shelf is called the shelf break. There is usually a slope below the break. The continental slope connects the continental shelf and the continental rise. The end of continental rise is the deep ocean floor. Figure 4.1 demonstrates the underwater continental parts.

Figure 4.2 shows the updated computational domain. B is the coordinate system origin. The region $CBID$ is the air-water subdomain. CD is $12m$ and CB is

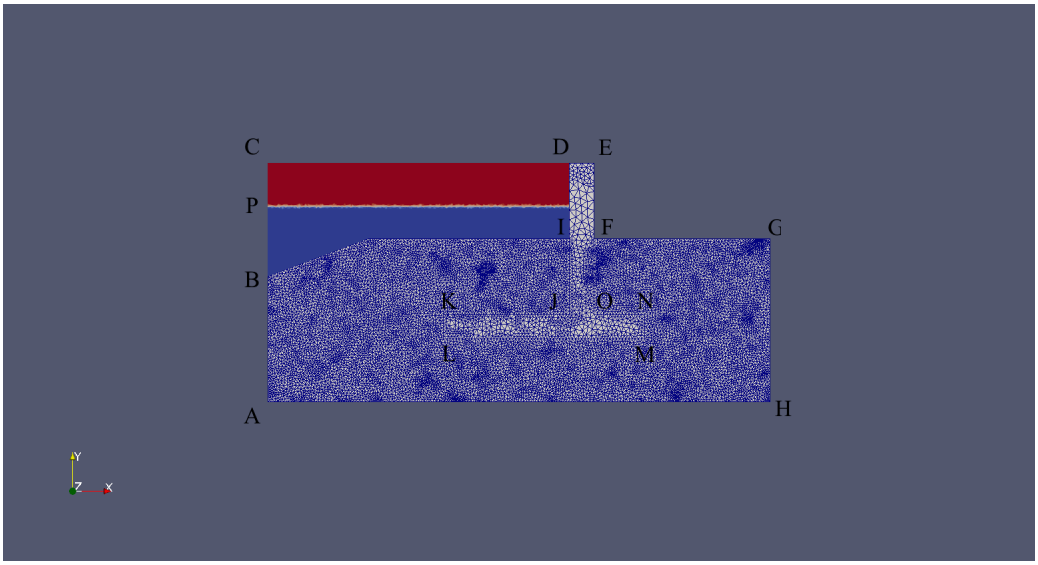

Figure 4.2: Computational Domain for Interaction Models

$4.5m$. PI is the air water interface. The water depth at P is $1.5m$. The slope angle $\alpha = arctan(0.375)$, which is about 20 degrees. A flat continental shelf is assumed. The height of the floodwall above the ground DI is $3m$. The width DE is $1m$. The portion embedded in soil $IJ = 3m$. The floodwall toe $KJ = 5m$ and $ON = 2m$. Soil domain depth GH is $6.5m$ and length AH is $20m$. The choice for floodwall sizes has passed the two factors of safety tests. The maximum element diameter h_e for flow subdomain and floodwall is $0.1m$. For soil subdomain h_{es} is $0.025m$. We will use this test domain for all interaction models and simulations.

We first generate the simulation of flow driven by waves. Again, same as in Section 3.3.3, multiple random single-peaked waves are used. We look into the myfoxhurricane database for current wave information. Figure 4.3 shows the current wave height in Galveston area is 2ft (0.61m) at 10:00pm EST on October 26, 2016.

There are no tropical cyclones now in the Gulf of Mexico area.

Figure 4.3: Wave Heights in the Gulf of Mexico at 10pm EST, 10/26/2016 (From myFoxHurricane, 2016)

Let the peak period be 2s and wave height be 0.8m which is within normal wave height range for Galveston Bay. The peak wave length is 3.9m. The total simulation lasts for 10s. Time step Δt is 0.1s. The volume of fractions for air and water over time is displayed in Figure 4.4 .

The tractions along the flow structure interface are extracted and used in the computation for the structure subproblem. The deformation at given time is displayed in Figure 4.5. From the output, again, we observe the deformation first appears on the top part of the floodwall. When $t = 2.5s$ in Figure 4.5(b), obvious deformation is found on the floodwall heel and toe. The largest deformation occurs on the floodwall top, again, as expected. When $t = 6.5s$ in Figure 4.5(d), larger

(a) t=1s

(b) t=2s

(c) t=3s

(d) t=4s

(e) t=5s

(f) t=6s

(g) t=7s

(h) t=8s

(i) t=9s

(j) t=10s

Figure 4.4: Air-Water Volume Fraction at 1s, 2s, ..., 10s

deformation is observed in both floodwall and soil regions. At $t = 7.5s$ in Figure 4.5(e), displacement for both regions starts to decrease. When $t = 8.5s$ in Figure 4.5(g), largest deformation is reached at the floodwall top. At $t = 9.5s$ in Figure 4.5(h), the deformation decreases again. Deformation changes happen more often in the latter time steps than in the earlier time steps. It meets expectation, since it takes time for the first wave front to reach the wall. Recall the peak wave length is $3.9m$ but the air water domain is $12m$ long. After a few seconds, wave effect starts to accumulate and results in more deformation changes.

Figure 4.6 to Figure 4.11 show the actual displacement of the structure subdomain more intuitively. In our experiment, the wave height is 0.8m. It is the normal wave amplitude when no tropical cyclone happens. The largest displacement is 1.4mm, which is 0.1% of the floodwall width. It meets with common sense - a manmade floodwall should not move much when there is no cyclone. To make it easier to see the movement with time, we rescale by a factor of 100, as seen in Figure 4.6 to Figure 4.11.

We also plot the magnitude of the stress over the whole domain for each of the time step. From Figure 4.13to Figure 4.16, we can see the largest stress concentrate along the floodwall boundary. This gives design engineers direct impression of the wave effect on structures.

When hurricane actually happens, wave height will increase from several feet to tens of feet. From myFoxHurricane record, Figure 4.12 shows the wave heights in Atlantic Ocean during Hurricane Matthew on October 2nd, 2016. Near the eye area wave height was above 18ft (5.49m). Along the coastline average wave height

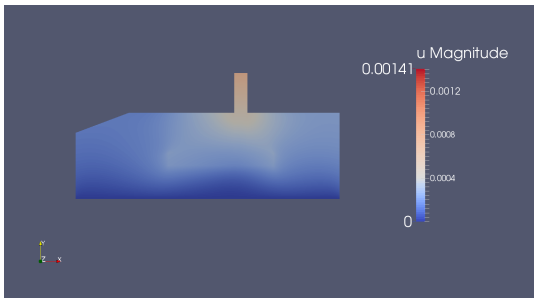

(a) t=0.1s

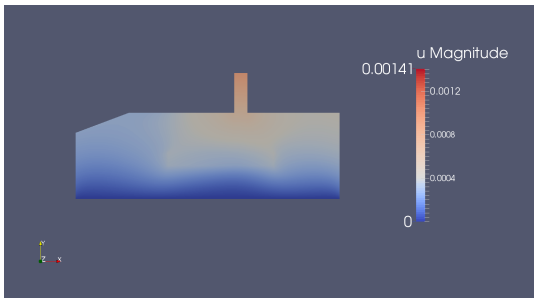

(b) t=2.5s

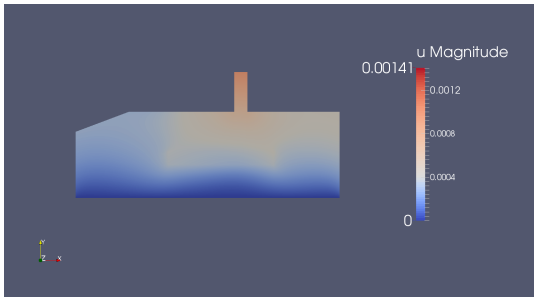

(c) t=4s

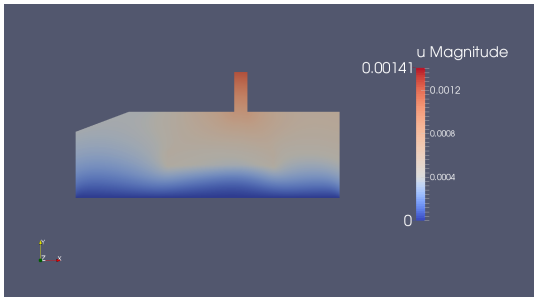

(d) t=6.5s

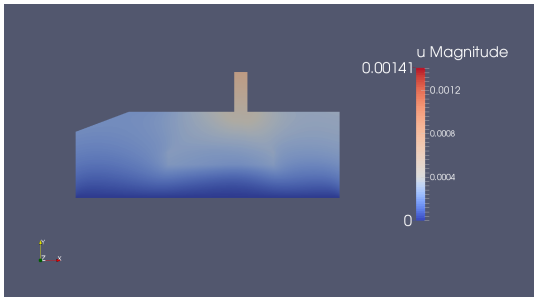

(e) t=7.5s

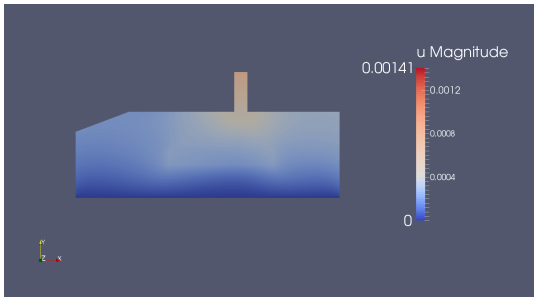

(f) t=8s

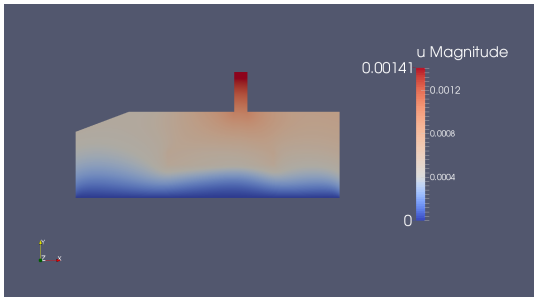

(g) t=8.5s

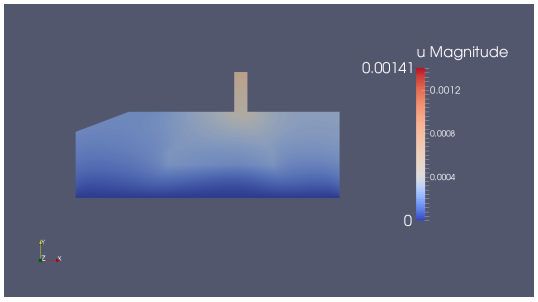

(h) t=9.5s

Figure 4.5: Structure Deformation of One-way Interaction at t=0.1s, 2.5s, 4s, 6.5s, 7.5s, 8s, 8.5s and 9.5s: m

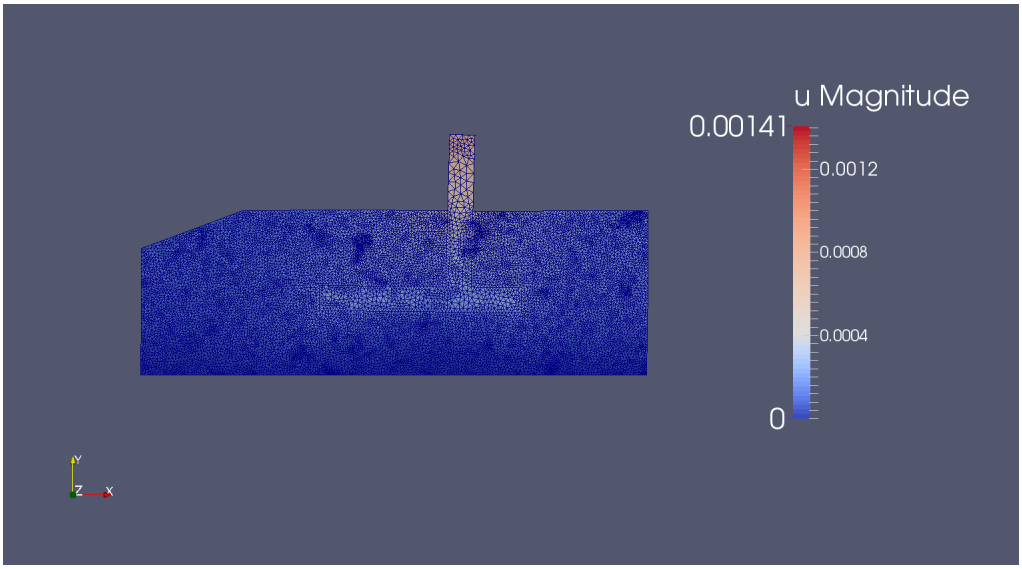

Figure 4.6: Deformation at t=0.1s: m

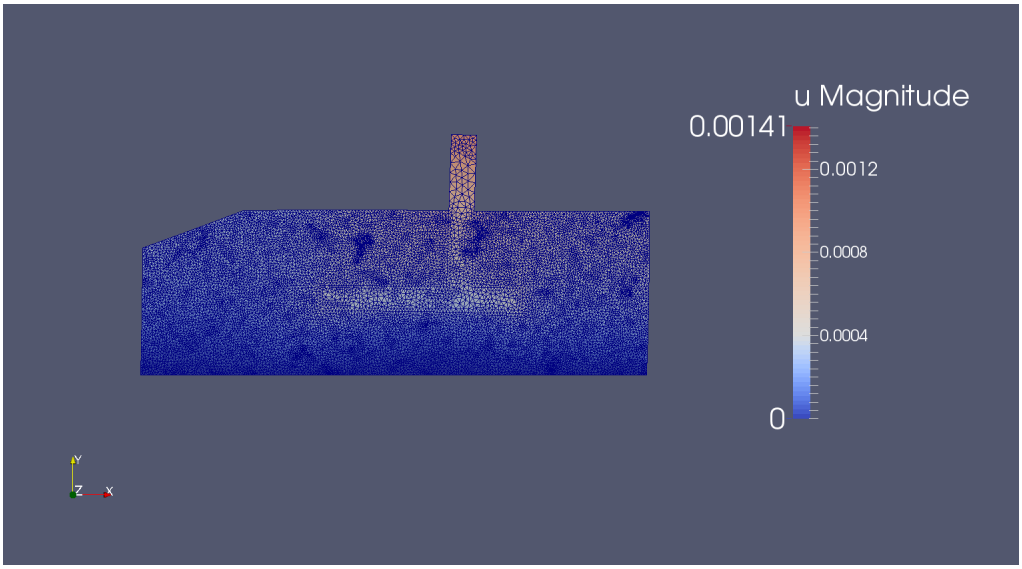

Figure 4.7: Deformation at t=4s: m

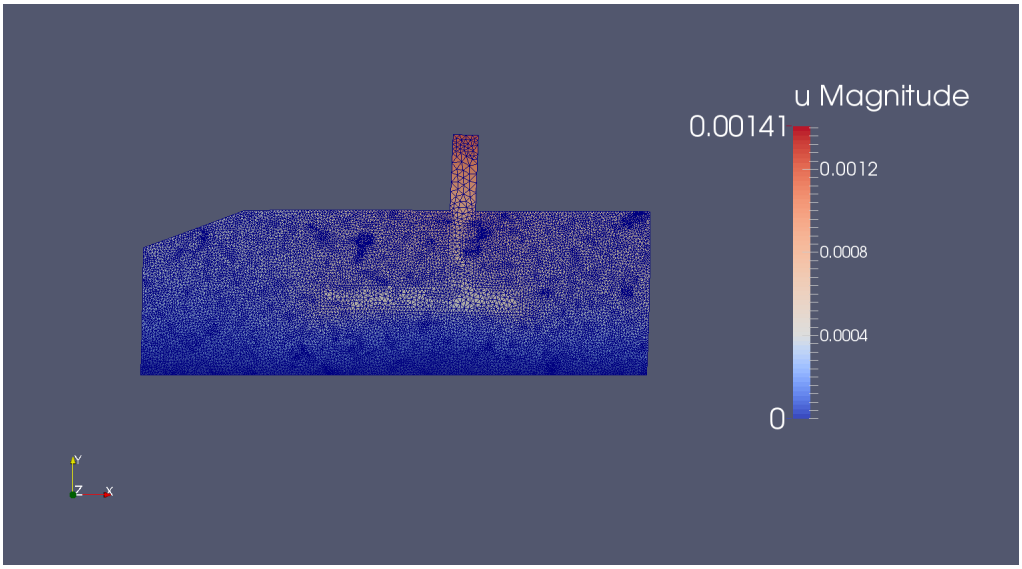

Figure 4.8: Deformation at t=6.5s: m

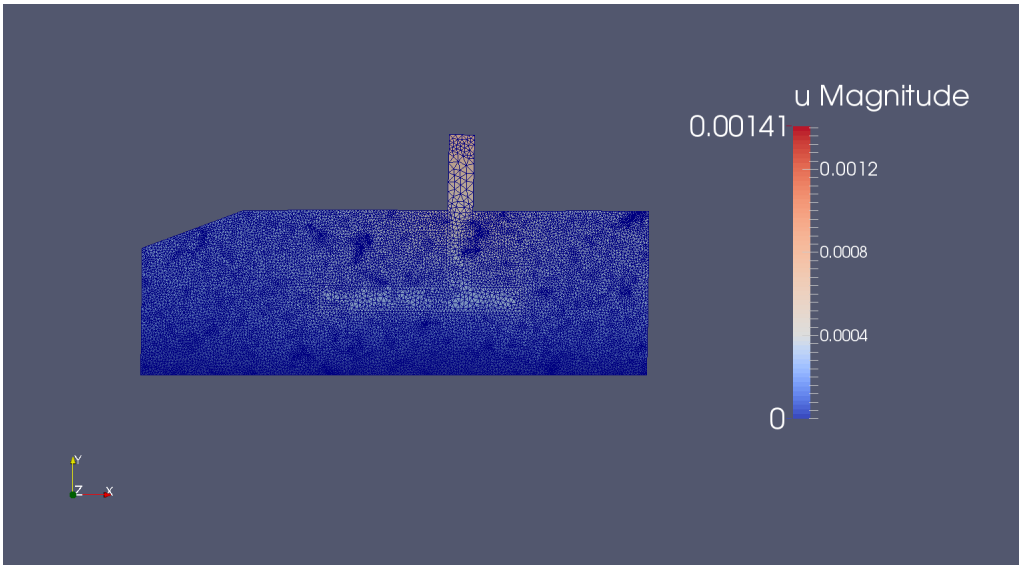

Figure 4.9: Deformation at t=8s: m

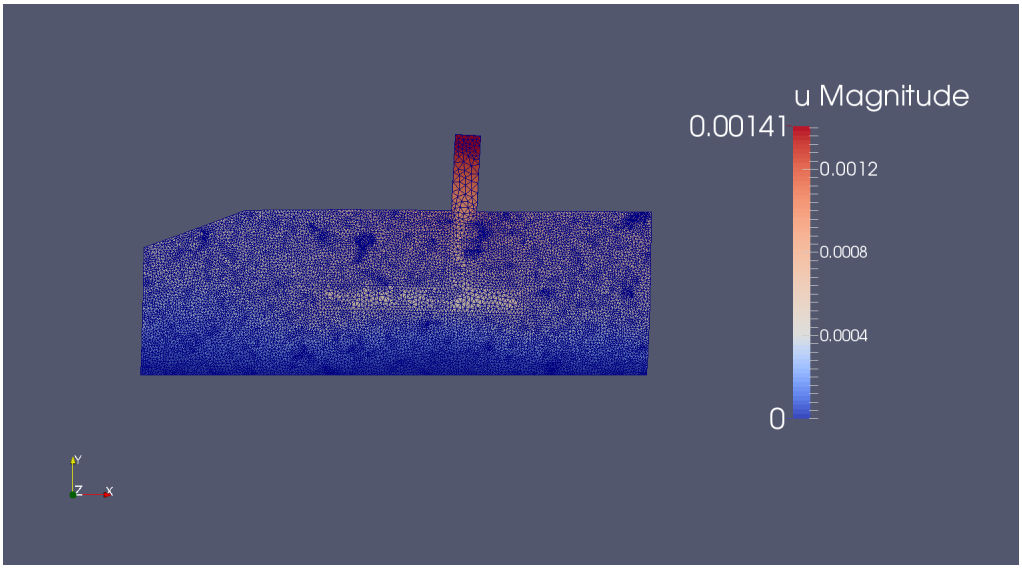

Figure 4.10: Deformation at t=8.5s: m

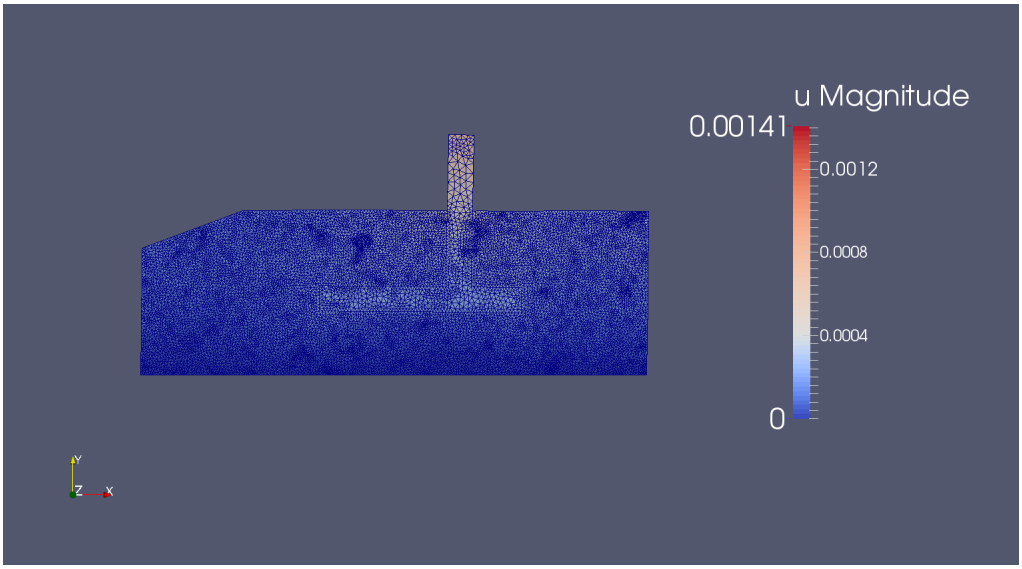

Figure 4.11: Deformation at t=9.5s: m

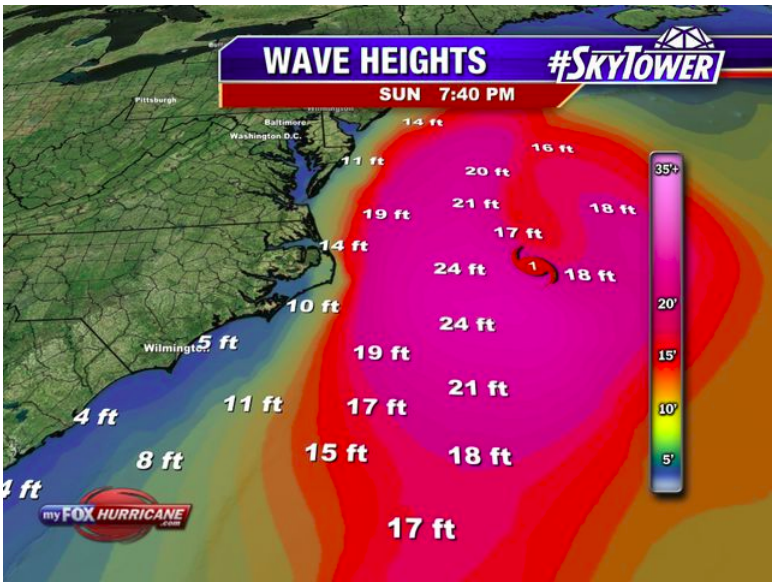

Figure 4.12: Wave Heights During Hurricane Matthew on 10/2/2016 (From myFox-Hurricane, 2016)

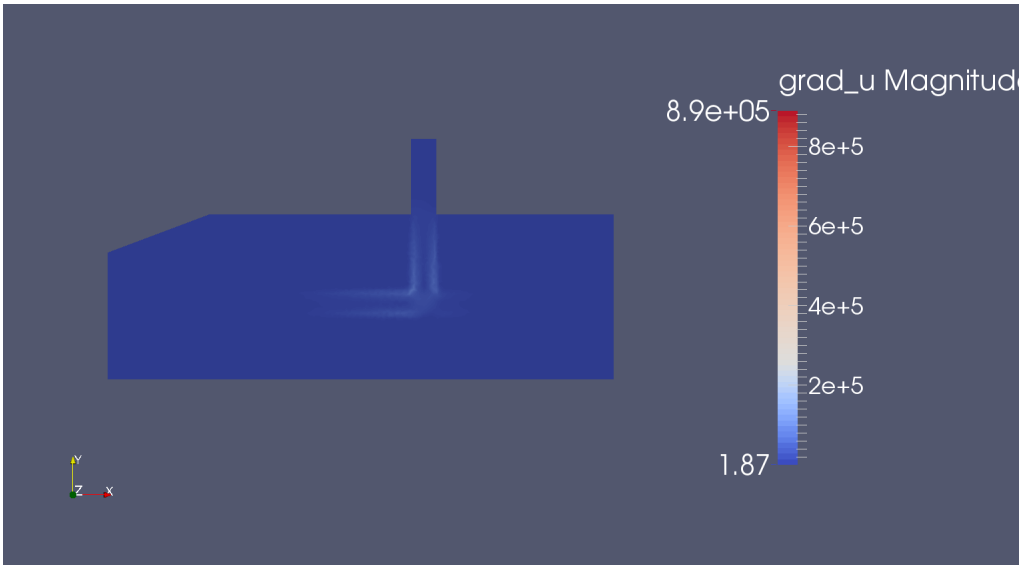

Figure 4.13: Stress at t=0.1s: Pa

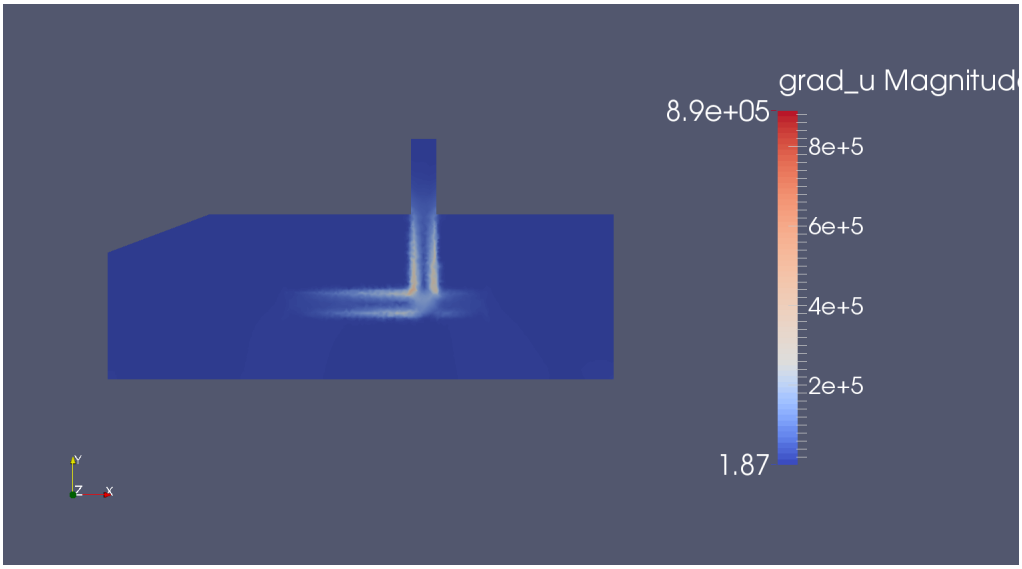

Figure 4.14: Stress at t=4.1s: Pa

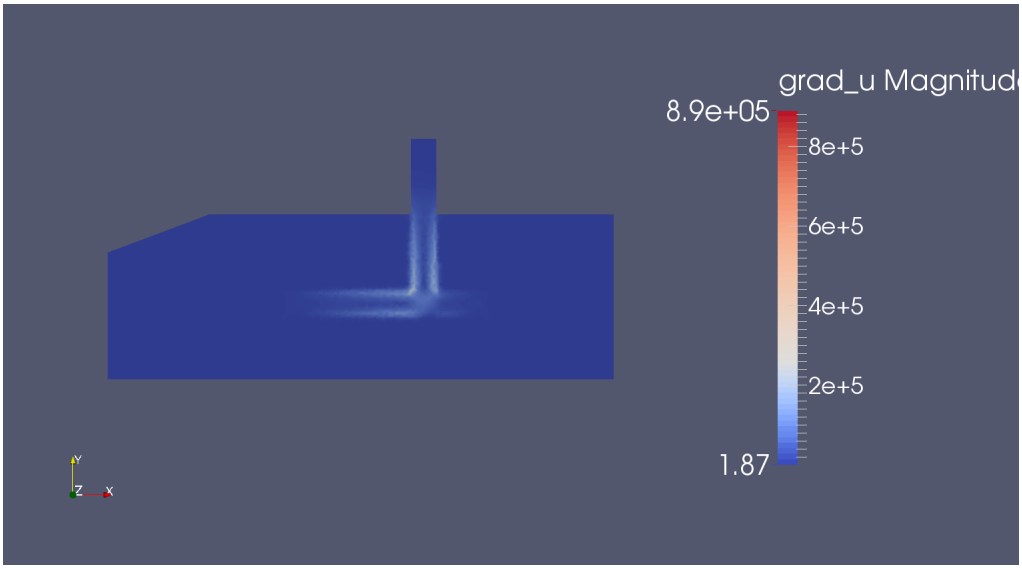

Figure 4.15: Stress at t=6.9s: Pa

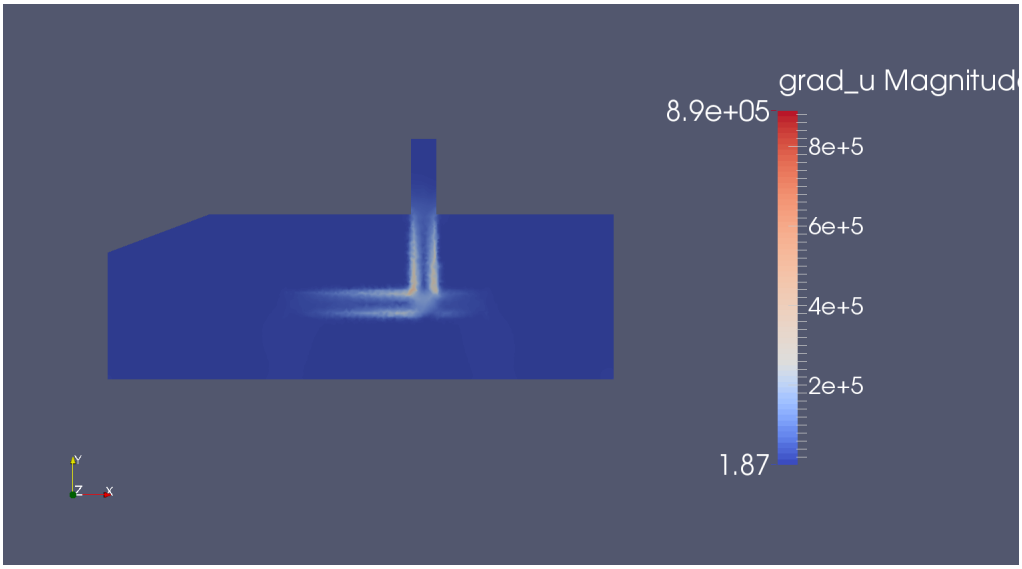

Figure 4.16: Stress at t=9.0s: Pa

ranged from 4ft to 14ft (1.2m to 4.3m). When Hurricane Ike approached Texas in 2008, the significant wave observed near Galveston Bay was 23.3ft (7.1m) high.

In our computational domain, the floodwall height above ground is 3m. The extreme case is the original water depth is 0m so that the largest wave can be modeled is the one with 3m in height. Otherwise, overtopping may happen and our model will be not applicable. To explore the relationship between wave height and maximum floodwall displacement, especially under large waves, a slight change is made to the computational domain. We increase the floodwall height above soil to be 5m. We also let the original water depth change to 0.7m. Now the maximum wave height can reach 4.3m technically. We rerun the same algorithm on this domain and take records of the maximum displacement. The relation between wave heights and maximum displacement is shown in Figure 4.17.

Figure 4.17 tells when the wave height is relatively small, say 2ft (0.61m), the maximum displacement is about 1mm. That is less than 0.1% of the floodwall width. The floodwall is absolutely safe, as expected. The trend is almost linear. As wave height increases, the maximum displacement cannot be neglected. When the wave height reaches 14ft (4.3m), the maximum displacement is 4.5cm, which is 4.5% of the floodwall width. It is an observable movement and may cause the floodwall to overturn. When the deformation is relatively significant, the effect from structure deformation to air water flow system cannot be ignored. To make our model valid and accurate for general cases, it is necessary to move forward to the full two-way interaction models.

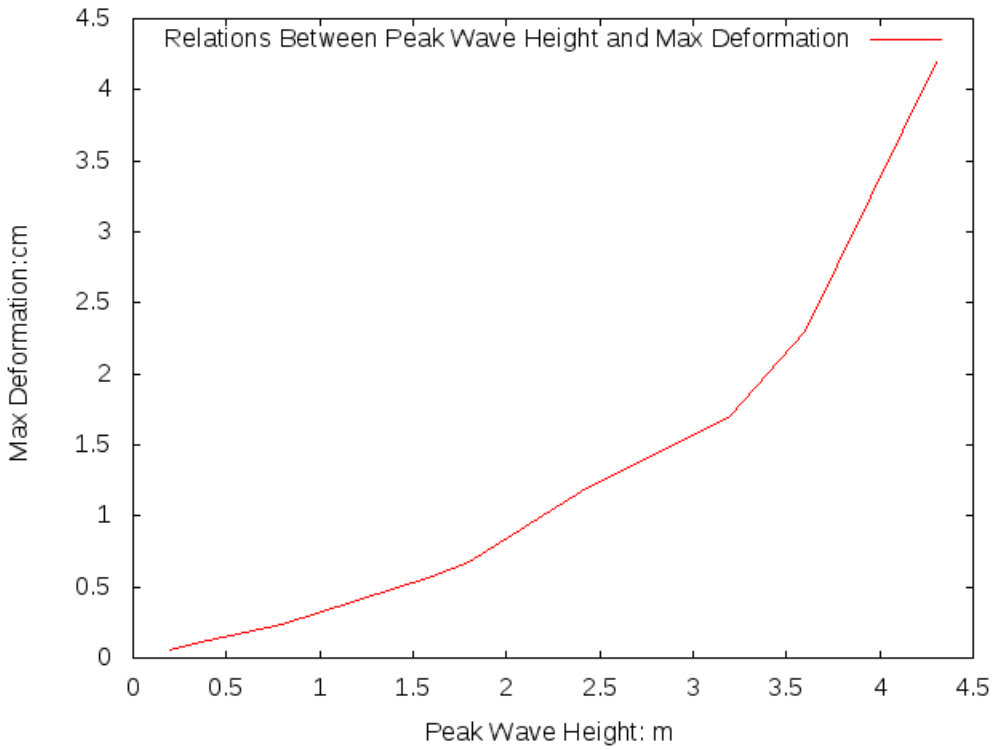

Figure 4.17: Relation between Wave Height and Maximum Floodwall Displacement

Chapter 5

Two-way Interaction Models

5.1 FSI Under ALE Formulation

As stated in Section 3, the Lagrangian framework is mostly used in structural subproblems where the computational mesh moves with the structure. It allows for tracking of common boundaries attached with the structure. But it is difficult to describe the large distortion of the domain. For the fluid subproblem described in Section 2, an Eulerian approach is naturally used where the mesh represents a fixed reference frame. Large distortion can be handled well in the Eulerian framework, while it is expensive to locate the precise interface [18, 19]. To model the interaction process it is necessary to combine the two frameworks into one setting and remain relatively low computational cost.

The arbitrary Lagrangian-Eulerian (ALE) framework is one of the commonly used methods for flows on moving domains [18, 19, 23]. The purpose of this design is to combine the advantages of the traditional kinematic descriptions and overcome their respective disadvantages to a certain extent [19]. Similar to the Lagrangian approach, the ALE description also uses a reference domain. However, the

main difference is that in the ALE methods the reference domain does not follow the motion of the fluid itself. As the name suggests, the nodes of the mesh move arbitrarily with the material.

In the fluid structure two-way interaction models [55], we use upper case letters for the parameters in the reference domain, and the lower case letters stand for the variables in the current domain. Let Ω be the reference domain, and ω be the current fluid domain in $\mathcal{R}^2$. Ω is partitioned into fluid and structural subdomains Ω_F and Ω_S respectively, with $\overline{\Omega}_F \cup \overline{\Omega}_S = \Omega$, $\Omega_F \cap \Omega_S = \emptyset$(empty set). Similarly, $\overline{\omega}_F \cup \overline{\omega}_S = \omega$, $\omega_F(t) \cap \omega_S(t) = \emptyset$ for $t \in [0, T]$. The interface between the fluid and the structure is denoted as Γ_{FS} and $\gamma_{FS}(t)$ respectively.

We first define a map $\Phi(\ ,t) : \Omega \longmapsto \omega(t)$. It maps a reference point $X \in \Omega$ to the corresponding current point $x \in \omega(t)$, i.e. $x = \Phi(X, t)$. The fluid and structure subdomains are deformed independently, so the map is split as [55]:

$$\Phi(X,t) = \begin{cases} \Phi_S(X,t)\,, & \forall X \in \Omega_S, t \in [0,T], \\ \Phi_M(X,t)\,, & \forall X \in \Omega_F, t \in [0,T]. \end{cases} \tag{5.1}$$

where

$$\Phi_S(X,t) = X + U_S(X,t), \tag{5.2}$$

$$\Phi_M(X,t) = X + U_M(X,t), \tag{5.3}$$

(U_S, U_M) are the displacements of the structure and the mesh respectively.

For the governing equations, the structure part remains the same as in the previous Section 3. For the fluid subproblem, we need to make corrections to some of

the governing equation. Under the ALE framework, the convective term in Navier-Stokes Equation is replaced by $\rho_F(\frac{\partial u_F}{\partial t}+grad\, u_F\cdot(u_F-\frac{\partial U_M}{\partial t}))$. The level set equation is corrected by modifying the advective term as $\frac{\partial \phi}{\partial t}+(u_F-\frac{\partial U_M}{\partial t})\cdot\nabla\phi=0$. The mesh is modeled by a linearly elastic description of the fluid domain [55], where the stress tensor is defined by $\Sigma_M(U_M)=\mu_M(Grad\, U_M+Grad\, U_M^T)+\lambda_M tr(Grad\, U_M)I$. μ_M and λ_M are given positive constants.

In summary, the fluid problem (F), the structure problem (S) and the mesh problem (M) are fully coupled as:

$$
\begin{aligned}
(F):\rho_F(\frac{\partial u_F}{\partial t}+grad\, u_F\cdot(u_F-\frac{\partial U_M}{\partial t})) &= div\,\sigma_F(u_F,p_F)+b_F,\ in\ \omega_F && (5.4)\\
div\, u_F &= 0,\ in\ \omega_F(t) && (5.5)\\
(S):\rho_S\frac{\partial^2 U_S}{\partial t^2}-Div\ \Sigma_S(U_S) &= B_S,\ in\ \Omega_S\times[0,T] && (5.6)\\
(M):\frac{\partial U_M}{\partial t}-Div\ \Sigma_M(U_M) &= 0,\ in\ \Omega_F\times[0,T] && (5.7)
\end{aligned}
$$

with the proper initial and boundary conditions. Here b_F and B_S are the body forces per unit mass. Notice that for fluid and structure subproblems (F) and (S), Navier-Stokes Equation and linear elastic equation are listed for demonstration. It does not mean the subproblems are simplified for the whole system. In actual computation, we will still solve for all the governing equations for both subproblems as described in Section 2 and 3.

The stress from the fluid is transferred to the structure, so the normal stress at the common fluid-structure interface should be equal in value and opposite in direction. In addition, the kinematic continuity at the interface is enforced, which ensures there is no gap between the fluid and the structure. So more boundary

conditions are required to prevent the fluid and structure meshes from separating at the interface. Additional boundary conditions for the interaction are [55]:

$$(J_M(\sigma_F \circ \Phi_M) \cdot F_M^{-T}) \cdot N_F = -\Sigma_S \cdot N_S, on\ \Gamma_{FS} \tag{5.8}$$

$$u_F \circ \Phi_M = \frac{\partial^2 U_S}{\partial t^2}, on\ \Gamma_{FS} \tag{5.9}$$

Here, N_S and N_F are the outward normal on the interface of the structure and the fluid subdomains, respectively, and $F_M = Grad\,\Phi_M$, $J_M = det\,F_M$.

5.2 FSI Solver

A partitioned approach is used to solve the fully coupled FSI system [55]. Stability of explicit coupling is discussed in [13, 10]. In each time step t_n, the three subproblems are solved iteratively, and are connected by the boundary conditions at the interface. In detail, the fluid subproblem is solved at first on the current fluid domain $\omega_F(t)$. The stress σ_F is then calculated and transferred to the solid problem by (5.8) in the reference domain Ω_S. The solid subproblem is then solved for the structural displacement with the Neumann boundary conditions from the previously evaluated fluid stress. The displacement field is treated as the boundary condition on the common fluid-structure interface for the mesh problem in the fluid reference domain by (5.9). The mesh problem can be solved and a new current domain will be updated. The above process is repeated until convergence, then move to the next time-step t^{n+1}.

We are following the fluid-structure-mesh sequence in the above process. It is also possible to start with the structure subproblem, followed by the mesh equations and then the fluid part. We may expect fewer iterations in this treatment [55]. Velocity u_F and the pressure p_F are discretized in space with Taylor-Hood elements. There are three steps for the nonlinear variational problem. In the first step, the previously known pressure is used to compute the fluid velocity through the momentum equation. Then the pressure at the current time step is solved from the continuity equation. Lastly the velocity is corrected from the updated pressure.

For the structural subproblem, we still use the plastic-elastic algorithm from Section 3. It allows to solve the elastic structure equations in the Lagrangian framework. For space discretization we use first order Lagrange elements and for the time discretization we use the CG(1) method. In the CG(1) method, a dummy variable is introduced by adding one more equation

$$P_S - \frac{\partial U_S}{\partial t} = 0 \tag{5.10}$$

to the original structural equation. The Neumann conditions evaluated from the fluid subproblems are imposed in the variational form while the Dirichlet conditions are built directly in the Newton solver.

The mesh subproblem is discretized by using the first order spatial Lagrange element and a standard CG(1) formulation in time. Usually piecewise linears are chosen to approximate the mesh problem [55]. The Dirichlet boundary conditions for the mesh subproblem are obtained after the solution from structure subproblem is updated.

5.3 Numerical Results for Two Way Interaction

In the two way interaction simulation, we will use the same computational domain as in Figure 4.2. Again, multiple random single-peaked waves are used. The peak period keeps at 2s and peak wave height stays at 0.8m. The peak wave length is 3.9m. The total simulation time is 10s. The coupled system solutions over time are shown in Figure 5.1. The volume of fractions for air and water over time is plotted. For the structure subproblem the displacements of floodwall and soil subdomains are also shown.

From Figure 5.1, again, we observe the deformation first appears on the top part of the floodwall. When $t = 2.5s$ in Figure 5.1(b), deformation starts to appear on the floodwall heel and toe. When $t = 6.5s$ in Figure 5.1(d), the first wave front is about to reach the floodwall. When $t = 8.5s$ in Figure 5.1(g), larger deformation is reached at the floodwall top. At $t = 9.5s$ in Figure 5.1(h), the deformation decreases again. Figure 5.1 also explains why deformation changes happen less often in the earlier time steps, since it takes time for the first wave front to reach the wall.

The actual displacement of the structure subdomain is displayed in Figure 5.2 to Figure 5.7. To make it easier to see the movement with time, we again rescale by a factor of 100 in Figure 5.2 to Figure 5.7. By comparing Figure 5.1 with Figure 4.5 and Figure 5.2 to Figure 5.7 with Figure 4.6 to Figure 4.11 , we see the maximum displacement for two way interaction is slightly larger than that for one way interaction. They show the displacement at the same time step. But apparently there are differences between the two solutions when $t > 4.5s$. In one way interaction, maximum displacement is reached at $t = 8.5s$. However, this is not true for two way

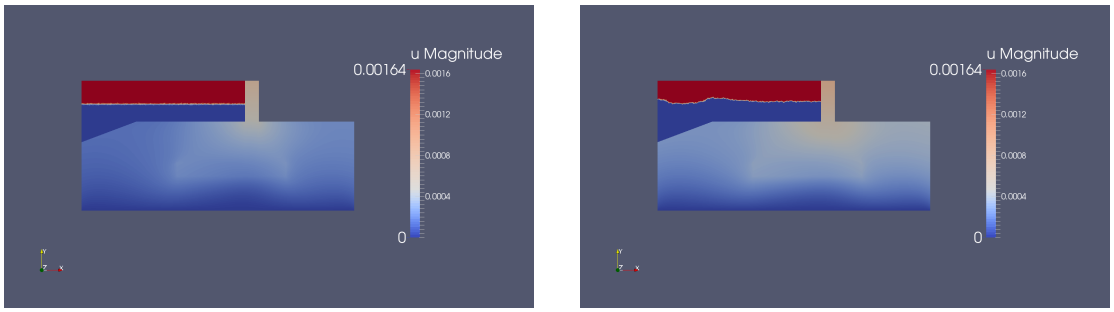

(a) t=0.1s (b) t=2.5s

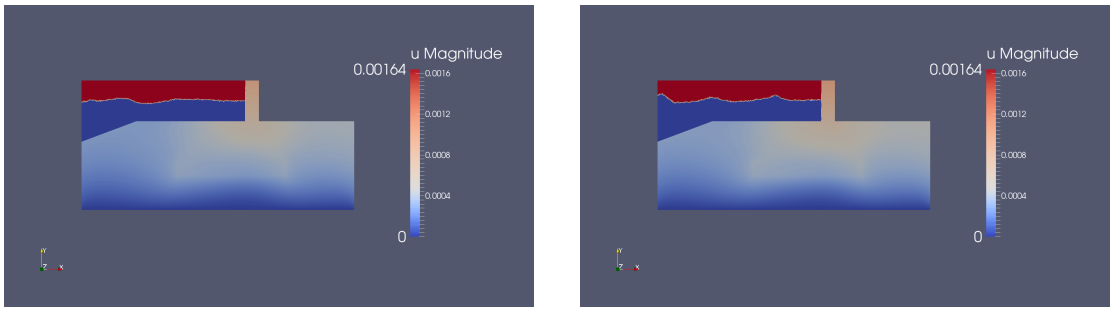

(c) t=4s (d) t=6.5s

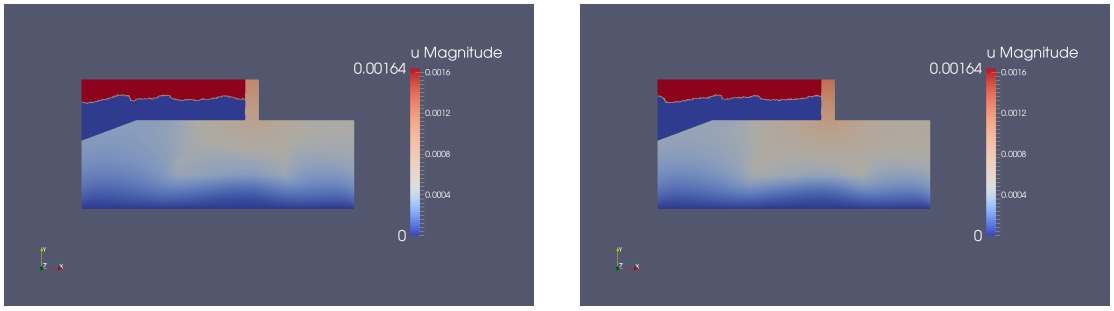

(e) t=7.5s (f) t=8s

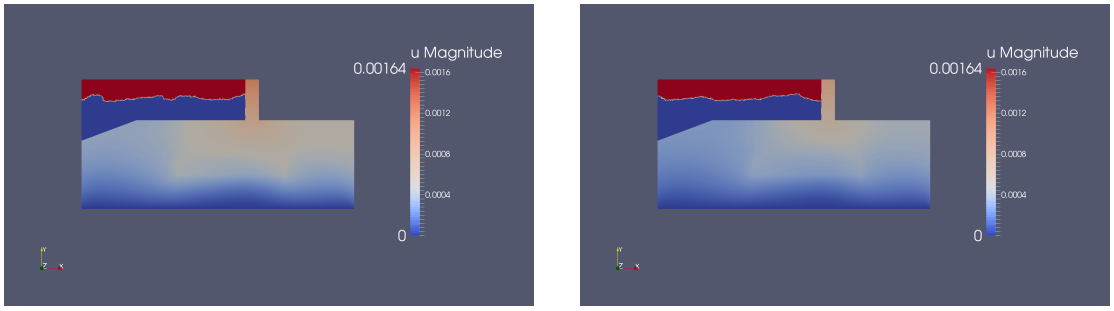

(g) t=8.5s (h) t=9.5s

Figure 5.1: Structure Deformation of Two-way Interaction at t=0.1s, 2.5s, 4s, 6.5s, 7.5s, 8s, 8.5s and 9.5s: m

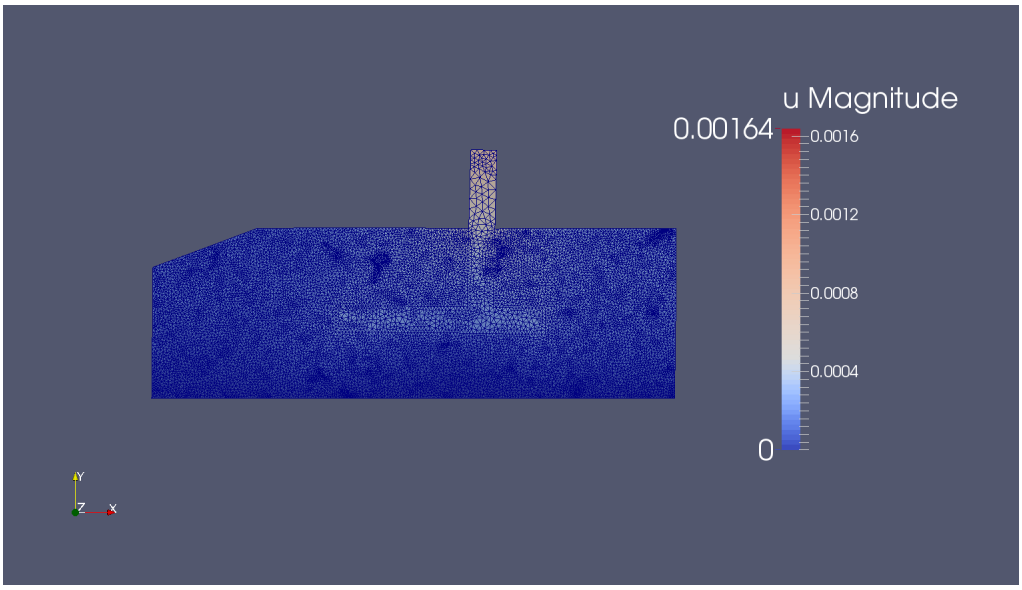

Figure 5.2: Deformation at t=0.1s: m

interaction. If the total simulation extends to 20s, we see the maximum displacement is reached at $t = 10.7s$, as seen in Figure 5.8.

The maximum displacement in the two way interaction is 1.64mm, and that in the one way interaction is 1.41mm. The relative difference between the two solutions is 14%. We should not expect the difference to be rather low, since the two models are inherently different. However, the difference should not be large either since a relatively low wave height is used. Stresses are also plotted as seen in Figure 5.9 to Figure 5.12. The largest magnitude of stress at all times is slightly larger than the one-way interaction simulation, probably due to the larger deformation captured in the full two-way model.

Again, we do the convergence analysis by varying the mesh size, similar

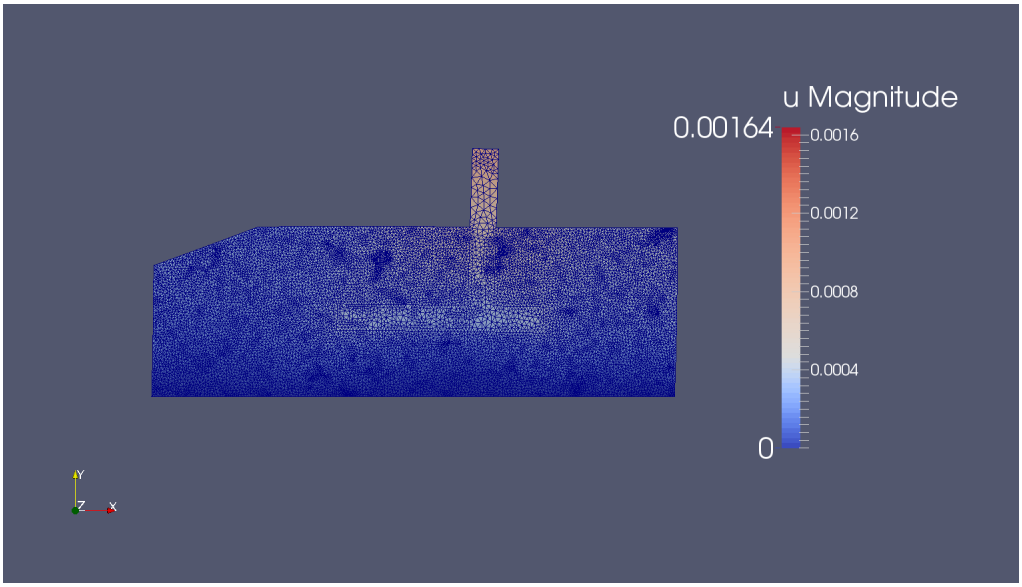

Figure 5.3: Deformation at t=4s: m

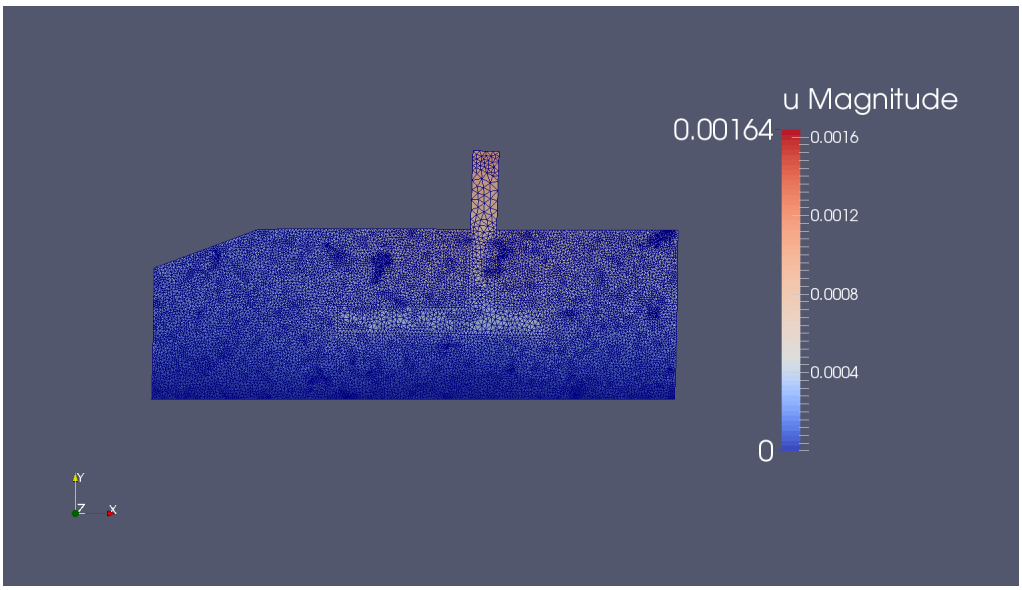

Figure 5.4: Deformation at t=6.5s: m

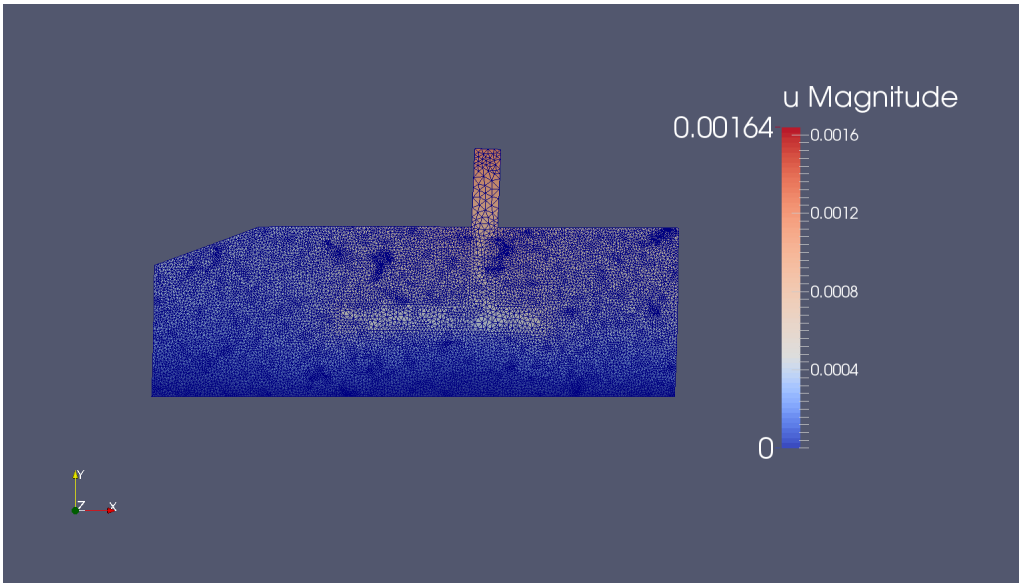

Figure 5.5: Deformation at t=8s: m

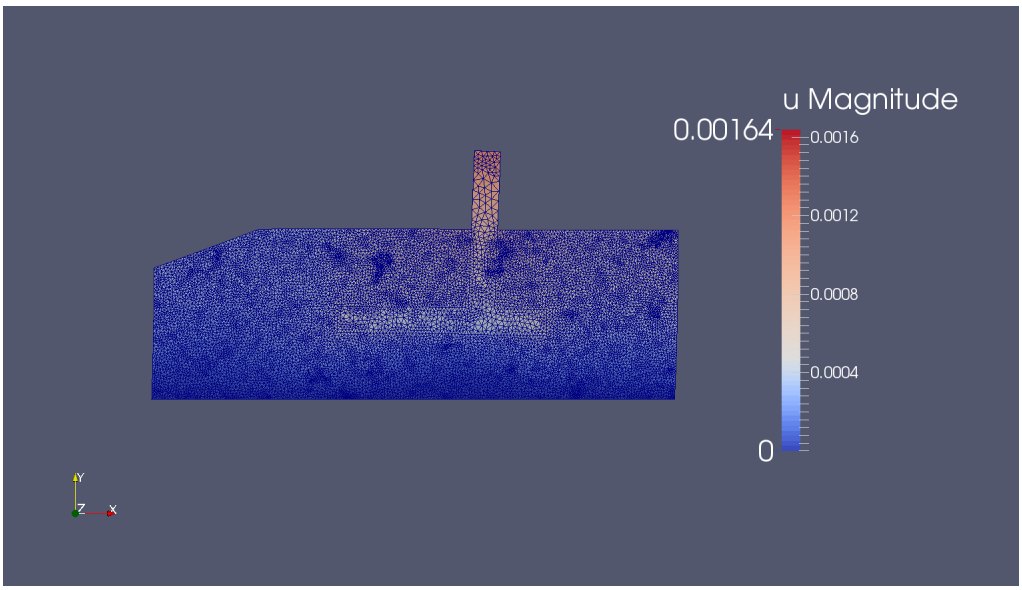

Figure 5.6: Deformation at t=8.5s: m

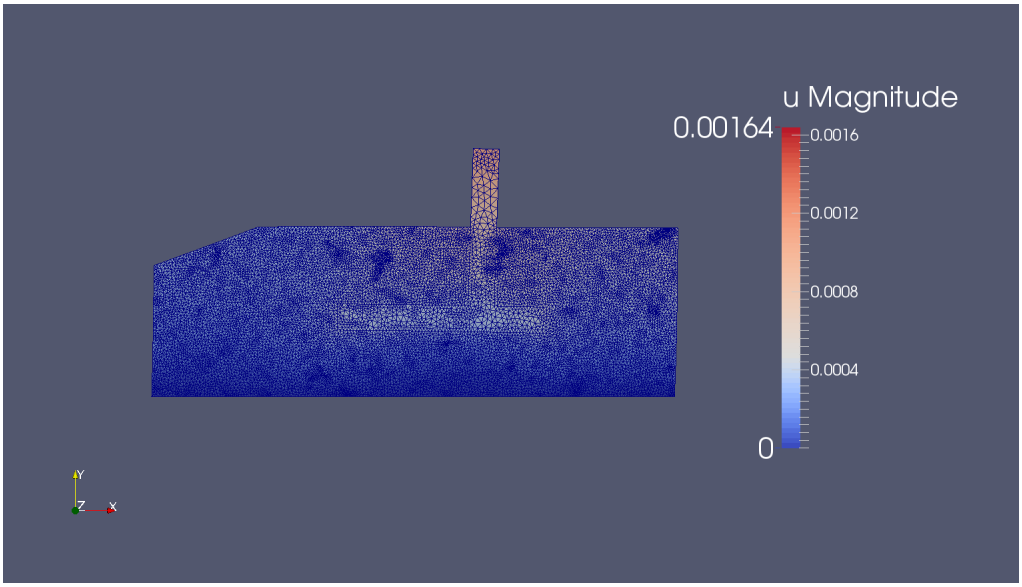

Figure 5.7: Deformation at t=9.5s: m

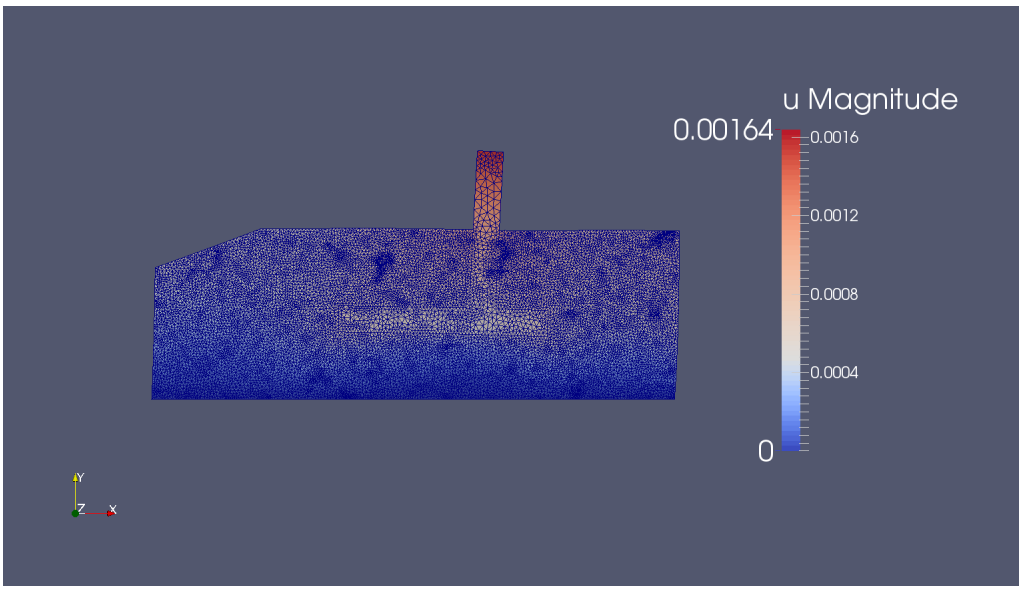

Figure 5.8: Deformation at t=10.7s: m

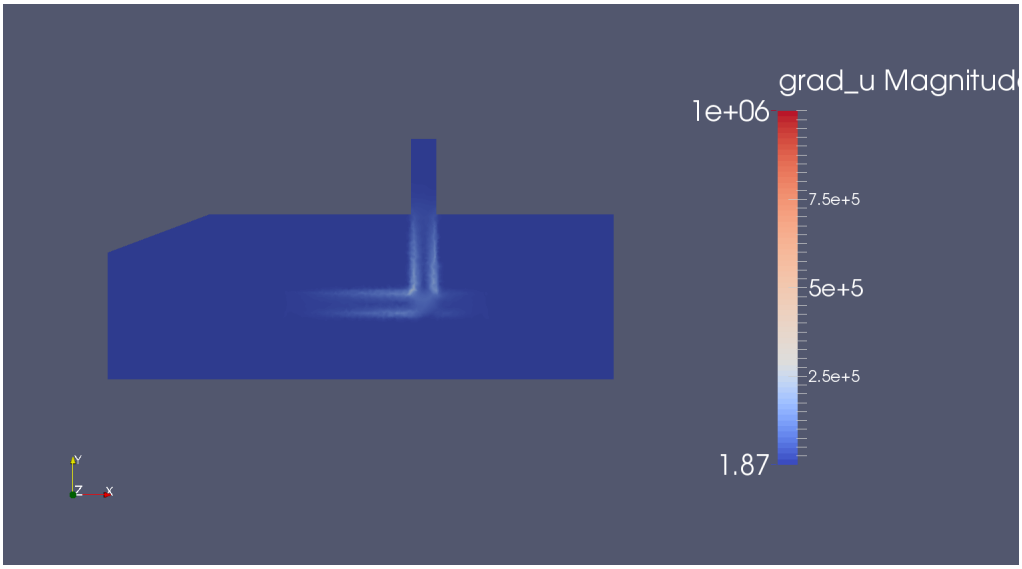

Figure 5.9: Stress at t=0.1s: Pa

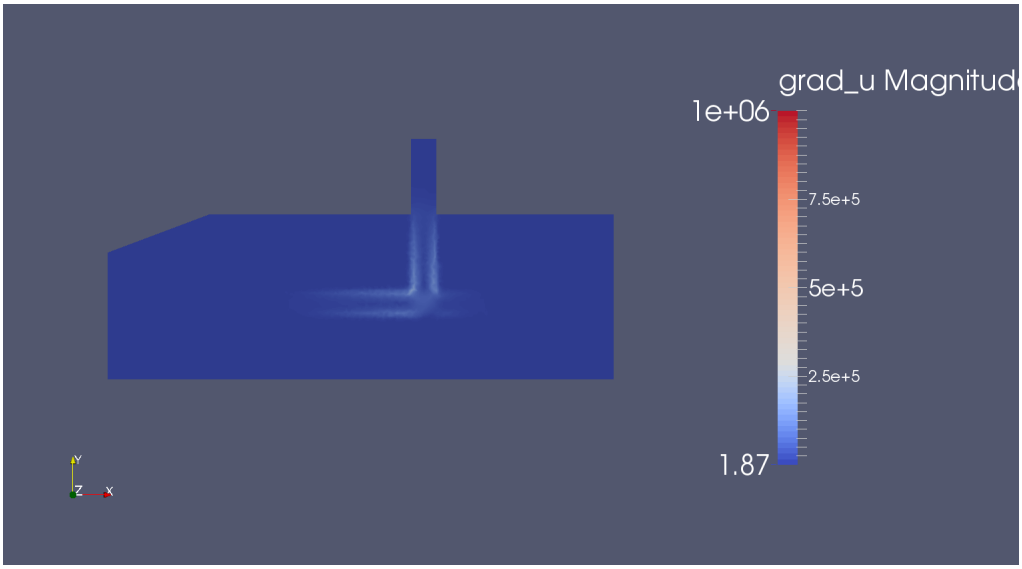

Figure 5.10: Stress at t=4.1s: Pa

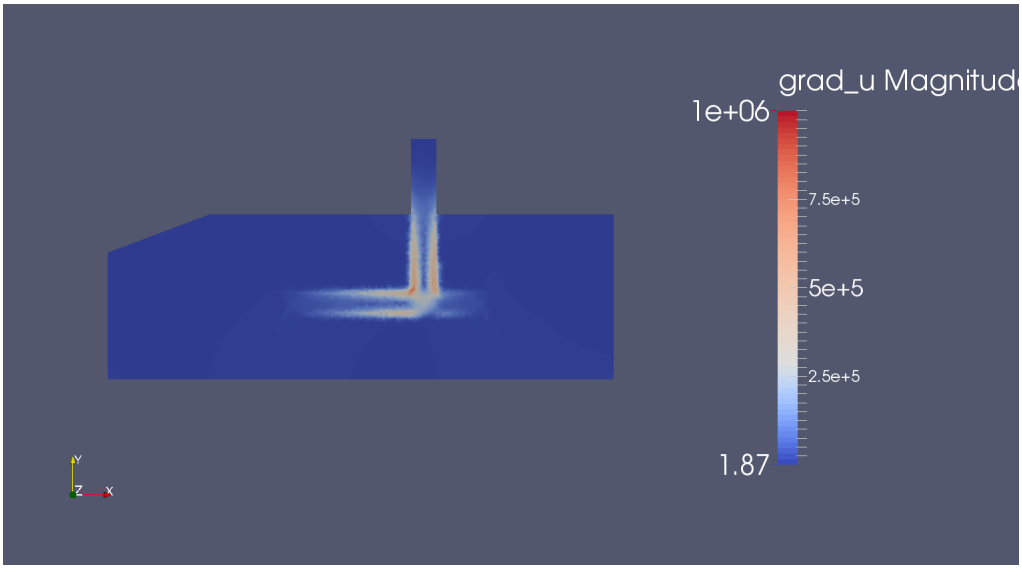

Figure 5.11: Stress at t=6.9s: Pa

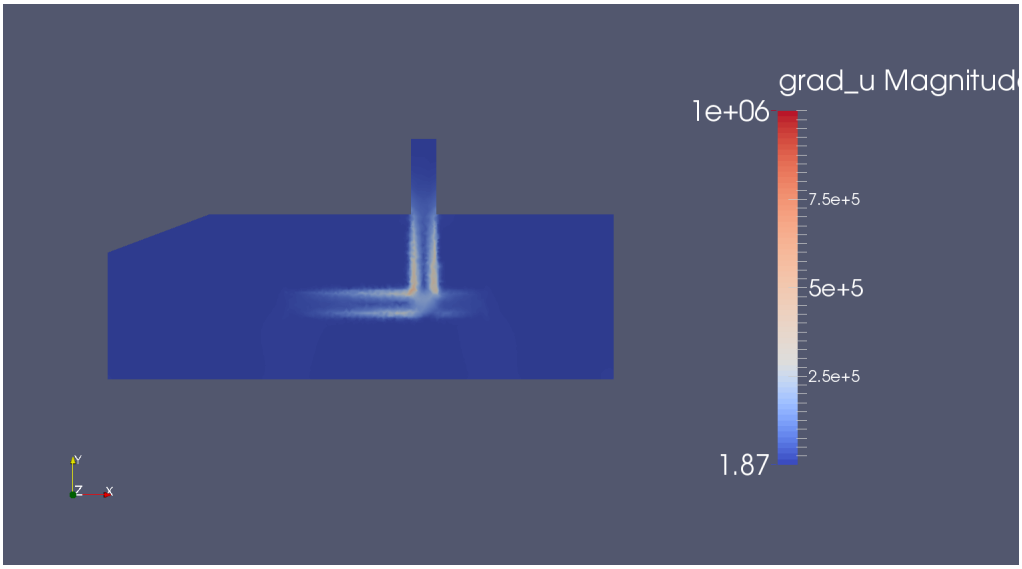

Figure 5.12: Stress at t=9.0s: Pa

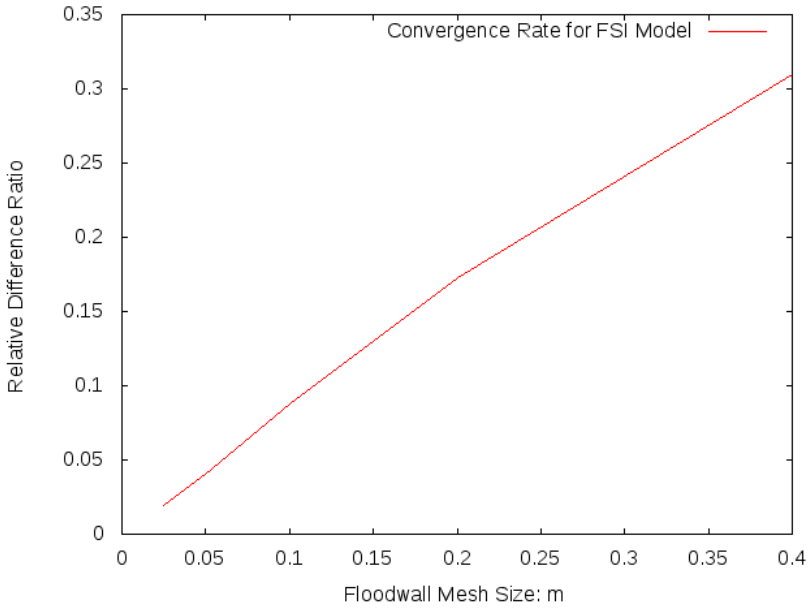

Figure 5.13: Convergence Analysis for Two Way Interaction

to what have been discussed in Section 3.5. Figure 5.13 shows almost first order convergence.

In the two way interaction experiment, it is relatively difficult to simulate for scenarios where wave heights are large. For example, in Figure 5.14, the wave front has reached the top of floodwall. Overtopping cannot be neglected since the two subproblems are solved simultaneously. The wave heights allowed in the model is strictly restricted by the height of the floodwall above ground. To test for more general cases, current model needs modification by adding air model to the structure subproblem. In that way the air subdomain can be higher than that of floodwall thus higher waves may be allowed. Extra effort should also be paid to model the

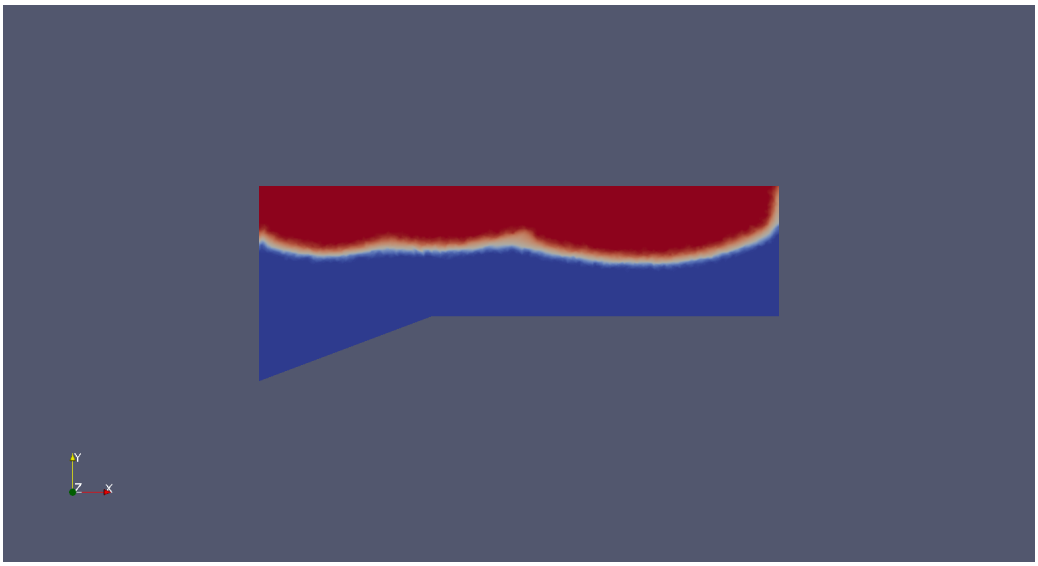

Figure 5.14: Possible Overtopping Scenario

overtopping process. This will be left as the future work.

Chapter 6

Future Work

We have demonstrated the models for the individual flow and structure subproblems and the partitioned approach for the coupled system. We also compare the differences between one way and two way interaction results. For the next step, we plan to develop the goal-oriented adaptive technique to couple the two-phase flow with the structure to further test the partitioned method.

In the partitioned approach, the coupling process is modeled from the boundary conditions on the fluid-structure interface. Theses boundary conditions are imposed weakly to the trial function spaces. To obtain a more general and stronger coupling effect we can further investigate Nitsche's method for handling the Dirichlet boundary conditions by reformulating them with penalty terms and embedding them into the variational forms. Compared to the traditional Galerkin method, Nitsche's method requires less degrees of freedom as the penalty parameter diminishes. In Nitsche's method the condition number remains bounded for fixed element diameter, while the traditional method may not converge for some iterative solvers. Nitsche's method is also applicable for non-matching meshes. Therefore, we will merge Nitsche's method into the ALE framework.

Furthermore, we plan to develop the monolithic approach solver for the two way interaction model, and use the results to examine those from the partitioned approach simulation. The benefits and drawbacks of the two approaches will also be demonstrated and verified. Next the numerical benchmark will also be used to evaluate and compare the different models as well as the various discretization schemes and the robustness of the solver.

Next, collected historical records from the failure of levee systems will be also used to validate the partitioned approach models on both accuracy and efficiency. The current computational models are expensive. It will definitely cost more for the monolithic method. One goal is to to reduce the memory cost and increase the computation speed by using the parallel implementation.

Finally, we will focus more on the quantities of interest. We would also like to examine the dependence of QoI on Young's modulus, Poisson ratio and hydraulic pressure gradient with different geometries. We will further study the application to a specific levee system in the Galveston Bay area. We will use the Advanced Circulation Model(ADCIRC) to obtain the external boundary forcing for the fluid model, look at various hurricane/levee scenarios and compare the numerical results with the existing levee/dam data and historical hurricane records.

Bibliography

[1] C.E. Kees, I. Akkerman, M.W. Farthing, Y. Bazilevs, *A conservative level set method suitable for variable-order approximations and unstructured meshes.* Journal of Computational Physics Volume 230, Issue 12, 1 June 2011, Pages 4536–4558.

[2] M.W. Farthing, C.E. Kees, *Evaluating finite element methods for the level set equation.* Technical Report TR-09-11, US Army Engineer Research and Development Center, Coastal and Hydraulics Laboratory, 2009.

[3] C. E. Kees, M. W. Farthing, M. T. Fong , *Locally conservative, stabilized finite element methods for a class of variable coefficient Navier-Stokes Equations.* ERDC/CHL TR-09-12, 2009.

[4] C. Kees, M. Farthing, C. Dawson, *Locally conservative, stabilized finite element methods for variably saturated flow.* Computer Methods in Applied Mechanics and Engineering 197 (2008) 4610–4625.

[5] M. Hsu, Y. Bazilevs, V. Calo, T. Tezduyar, T. Hughes, *Improving stability of multiscale formulations of fluid flow at small time steps.* Computer Methods in Applied Mechanics and Engineering 199 (2010) 828–840.

[6] Y. Bazilevs, V. M. Calo, T. E. Tezduyar, T. J. R. Hughes, *YZβ discontinuity capturing for advection-dominated processes with application to arterial drug delivery.*

International Journal for Numerical Methods in Fluids 2007; 54:593-608.

[7] I. Akkerman, Y. Bazilevs, V. M. Calo, T. J. R. Hughes, S. Hulshoff, *The role of continuity in residual-based variational multiscale modeling of turbulence.* Computional Mechanics (2008) 41:371-378.

[8] G. Hou, J. Wang, A. Layton, *Numerical Methods for Fluid-Structure Interaction-A Review.* Communications in Computational Physics, 12 (2012), pp. 337-377.

[9] J. Degroote, K. Bathe, J. Vierendeels, *Performance of a new partitioned procedure versus a monolithic procedure in fluid-structure interaction.* Computers and Structures 87 (2009) 793-801.

[10] M. Juntunen, R. Stenberg, *Nitsche's method for general boundary conditions* Mathematics of Computation, Volume 78, Number 267, July 2009, Pages 1353-1374.

[11] T. Wick, *Fluid-structure intertactions using different mesh motion techniques.* Computers and Structures (2011), doi:10.1016/j.compstruc.2011.02.019

[12] B. Helenbrook, *Mesh deformation using the biharmonic operator.* International Journal for Numerical Methods in Engineering 2001; 00:1-30

[13] E. Burman, M. A. Fernández, *Stabilization of explicit coupling in fluid-structure interaction involving fluid incompressibility.* Computer Methods in Applied Mechanics and Engineering, Elsevier, 2009, 198 (5-8), pp.766-784. <10.1016/j.cma.2008.10.012>. <inria- 00247409v4>

[14] S. Gilson, K. M. Jacoby, M. R. Stankiewicz, L. F. Harder, S. A. Medlock, S. W. Verigin, *Flood Protection Structure Accreditation Task Force: Final Report.* Flood Protection Structure Accreditation Task Force, The United States Army Corps of Engineers and the Federal Emergency Management Agency, November 2013.

[15] T. Richter. *A Fully Eulerian formulation for fluid-structure-interaction problems.* Journal of Computational Physics 233(2013) 227-240

[16] Th.Richter, Th. Wick. *Finite elements for fluid-structure-interaction in ALE and fully Eulerian coordinates*, Comput.Methods Appl.Mech.Engrg. 199(2010) 2633-2642

[17] T. Wick. *Fully Eulerian fluid-structure interaction for time-dependent problems*, Comput.Methods Appl.Mech.Engrg. 255(2013) 14-26

[18] Stoia-Djeska Marius and Safta CArmen-Anca. *Fluid-Structure-Interaction*, Fluid Dynamics, Computational Modelling and Applications, 195-216.

[19] L. Do, J. Day. *Overview of ALE method in LS-DYNA*, Livermore Software Technology Corporation, 2005

[20] A. Marzaban, M. Lakshmiraju, N. Richardson, M. Henneke, G. Wu, P. Vargas, O. Oakley *Offishore Platform Fluid Structure Interaction(FSI) Simulation*, OMAE 2012 -83472

[21] A. Hansbo, P. Hansbo and M. G.Larson. *A FINITE ELEMENT METHOD ON COMPOSITE GRIDS BASED ON NITSCHE'S METHOD* , Mathematical Modelling and Numerical Analysis, 37(3), 2003, 495-514

[22] K. Selim, A. Logg. *Simulating Heart Valve Dynamics in FEniCS* , 2009

[23] T. E. Tezduyar, S. Sathe, *Modelling of fluid-structure interactions with the space-time finite elements: Solutions techniques.* Int. J. Numer. Meth. Fluids 2007;54:855-900.

[24] J. Padgett, R. DesRoches, B. Nielson, M. Yashinsky, O. Kwon, N. Burdette and E. Tavera, *Bridge Damage and Repair Costs from Hurricane Katrina.* JOURNAL OF BRIDGE ENGINEERING, ASCE / JANUARY/FEBRUARY 2008.

[25] J. E. Padgett, A Spiller, C. Arnold, *Statistical analysis of coastal bridge vulnerability based on empirical evidence from Hurricane Katrina.*Structure and Infrastructure Engineering, 18 April 2009

[26] M. Stearns, J. E. Padgett, *IMPACT OF 2008 HURRICANE IKE ON BRIDGE INFRASTRUCTURE IN THE HOUSTON/GALVESTON REGION.* Journal of Performance of Constructed Facilities, February 9, 2011. doi:10.1061/(ASCE)CF.1943-5509.0000213

[27] J. Martin, D. M. Sheppard, *Storm Surge and Wave Loading on Bridge Superstructures.* Structures 2009: Don't Mess with Structural Engineers.

[28] *A Failure of Initiative: Final Report of the Select Bipartisan Committee to Investigate the Preparation for and Response to Hurricane Katrina.* U.S. House of Representatives.

[29] R. G. Bea, R. Iversen, T. Xu, *Wave-in-Deck Forces on Offshore Platforms.* Journal of Offshore Mechanics and Arctic Engineering, February 2001, Vol. 123/11

[30] W. Huang, H. Xiao *Numerical Modeling of Dynamic Wave Force Acting on Escambia Bay Bridge Deck during Hurricane Ivan.* J. Waterway, Port, Coastal, Ocean Eng. 2009.135:164-175.

[31] J. Briaud, H. Chen *Wave Forces on Bridge Decks during Hurricanes and Impact on the Foundation.* From Research to Practice in Geotechnical Engineering Congress 2008

[32] D. H. Peregrine, H. Bredmose, G. Bullock, C. Obhrai, G. Müller, and G. Wolters, *Violent water wave impact on a wall.* Annual review of fluid mechanics 35, no. 1 (2003): 23-43.

[33] P. Hansbo, J. Hermansson, T. Svedberg, *Nitsche's method combined with space-time finite elements for ALE fluid-structure interaction problems.* Compu. Methods Appl.Mech. Engrg, 193(2004) 4195-4206.

[34] *2013 Report Card for America's Infrastructure Findings.* American Society of Civil Engineers.

[35] S. Tirpak, S. Willey, J. Stokes, *Coastal Texas Protection and Restoration Project*, Project Management/ Planning/ Environmental USACE, Galveston District, August 2014.

[36] D. Conrad, O. Kapur, A. Mahadevia, D. Maldonado, J. Moline, G. Overcash, S. Passman, M. Perotin, A. Reeder, L. Seitz, A. Sheldon, J. Squerciati, *Engineering Principles and Practices for Retrofitting Flood-Prone Residential Structures*, Third Edition, FEMA P-259, January 2012.

[37] E. Blake, C. Landsea, E. Gibney, and N. Asheville, *The deadliest, costliest, and most intense United States tropical cyclones from 1851 to 2006 (and other frequently requested hurricane facts).* NOAA/National Weather Service, National Centers for Environmental Prediction, National Hurricane Center, 2007. www.nhc.noaa.gov/pdf/NW TPC- 5.pdf.

[38] Plyler, Allison, *Facts for Features: Katrina Impact.* The Data Center, Retreved 2016-02-22.

[39] *The New Orleans Hurricane Protection System: What Went Wrong and Why.* ASCE Hurricane Katrina External Review Panel report. Hosted at web.archive.org. Retreved 29, August 2015.

[40] J. McQuaid, B. Marshall, *Officials Knew About Weak Soil Under Levee.* Times Picayune, October 22, 2005

[41] J. McQuaid, *Swamp Peat Was Poor Anchor, Engineer Says.* Times Picayune, October 15, 2005

[42] S. Yang, *Investigators Release Preliminary Findings of Levee Failures at Senate Hearing.* University of California, Berkeley, November 2005.

[43] R. B. Seed, *Preliminary Report on the Perfomance of the New Orleans Levee Systems in Hurricane Katrina on August 29, 2005.* University of Clifornia, Berkeley, November 2, 2005.

[44] *Investigation of the Performance of the New Orleans Flood Protection Systems in Hurricane Katrina on August 29, 2005.* Independent Levee Investigation Team Final Report, July 31, 2006.

[45] M. Duncan, C. Y. Chang, *Nonlinear Analysis of Stress and Strain in Soils.* Journal of Soil Mechanics and Foundations, ASCE, 96(5): 1629-1653.

[46] D.C. Drucker, W. Prager, *Soil Mechanics and Plastic Analysis for Limit Design.* Quarterly of Applied Mathematics, 10(2), pp 157-165

[47] J.T.R. Hughes, *Unconditionally Stable Algorithms for Quasi-static Elasto/Viscoplastic Finite Element Analysis.* Computers and Structures, 8:169-173, 1978.

[48] Y. Tang, J. Zhou, X. Ren, Q. Yang, *Dynamic Response and Deformation Characteristic of Saturated Soft Clay under Subway Vehicle Loading.* DOI 10.1007/978-3-642-41987-4, Springer, 2014

[49] R. Liu, *Discontinuous Galerkin Finite Element Solution for Poromechanics.* Doctor of Philosophy Dissertation, The University of Texas at Austin, 2004.

[50] J. Lubliner, *Plasticity Theory.* Dover, ISBN 0-486-46290-0, ISBN 978-0-486-46290-5, 2008

[51] P. Helnwein, *Some Remarks on the Compressed Matrix Representation of Symmetric Second-Order and Fourth-Order Tensor.* Computer Methods in Applied Mechanics and Engineering, 190(22-23):2753-2770.

[52] Moondoggy, *Generic Stress-strain Graph for a Ductile Material.* [GFDL (http://www.gnu.org/copy or CC-BY-SA-3.0 (http://creativecommons.org/licenses/by-sa/3.0/)] https://commons.wikimedia.c strain1.svg

[53] P.J.Cook, C. Carleton, *Continental Shelf Limits: The Scientific and Legal Interface.* ISBN 0-19-511782-4, 2000

[54] Continental Margin, https://upload.wikimedia.org/wikipedia/commons/3/32/Continental_shelf.pn

[55] A. Logg, K. Mardal, G.N.Wells, *Automated Solution of Differential Equations by the Finite Element Method.* The FEniCS Book, fenicsproject.org.

[56] O. Ghattas, X. Li, *A Variational Finite Element Method for Stationary Nonlinear Fluid-Solid Interaction.* Journal of Computational Physics 121, 347-356, 1995

[57] M. W. Farthing and C. E. Kees, *Implementation of Discontinuous Galerkin Methods for the Level Set Equation on Unstructured Meshes.* ERDC/CHL CHETN-XIII-2, 2008

[58] C. E. Kees, M. W. Farthing, T. C. Lackey, and R. C. Berger, *A Review of Methods for Moving Boundary Problems.* ERDC/CHL TR-09-10, 2009

[59] J.C. Simo and J.T.R. Hughes. *General return mapping algorithms for rate independent plasticity in Constitutive Laws for Engineering Materials, ed., C.S. Desai.* Elsevier, N.Y., 1987.

[60] J.C. Simo and J.T.R. Hughes. *Computational Inelasticity.* Springer Verlag, New York, Inc., 1998.

[61] J.C. Simo and R.L. Taylor. *Consistent tangent operators for rate independent elasto-plasticity.* Computer Methods Appl. Mech. Engrg., 48:101–118, 1985.

[62] J.T.R. Hughes. *Numerical implementation of constitutive models: Rateindependent deviatoric plasticity, in Theoretical Foundations for Large Scale Computations of Nonlinear Material Behaviors, eds., S. NematNasser, R. Asaro, and G. Hegemier.* Martinus Nijhoff Publishers, Dor- drecht, The Netherlands, 1984.

[63] Jeager and Cook.*Fundamentals of Rock Mechanics.* Chapman and Hall, London, 1979

[64] R. Hill. *The mathematical theory of plasticity.* Oxford University Press, Oxford, U.K., 1950

[65] R. Hill, *A general theory of uniqueness and stability in elasto-plastic solids.* Journal of Mechanics and Physics of Solids, 6:236–249, 1958.

[66] G. W. Crenwdlge, E. L. Griffin, J. K. Baker, *Soil Survey of Galveston County, Texas.* United States Department of Agriculture, Soil Conservation Service, Texas Agricultural Experiment Station and the Texas State Soil and Water Conservation Board, February 1988.

Vita

Wei Du was born in the beautiful ancient city Xiangyang in Hubei Province, China. In 2007, she entered the University of Science and Technology of China with the Silver Award of Outstanding Incoming Students Scholarship. During the summer of 2010, she interned in the Key Laboratory of Intelligent Information Processing in Beijing. While in the University of Science and Technology of China, she worked at the Nature Inspired Computation and Applications Laboratory as an undergraduate research assistant. She received the degree of Bachelor of Science in Applied Mathematics from the University of Science and Technology of China in June 2011. She began graduate studies at the Institute for Computational Engineering and Sciences at the University of Texas at Austin in August 2011. She was awarded the Graduate School Fellowship of the University of Texas at Austin in 2011. She received her Master of Science degree in Computational Science, Engineering, and Mathematics in May 2014.

Permanent address: weidu@ices.utexas.edu

This dissertation was typeset with LaTeX[†] by the author.

[†]LaTeX is a document preparation system developed by Leslie Lamport as a special version of Donald Knuth's TeX Program.